5-2008

A Collection of New Studies Using Existing and Proposed Techniques and Instrumentation for Nondestructive Testing and Analysis of Concrete Materials and Structures

Shane D. Boone
Utah State University

Utah State University
MERRILL-CAZIER LIBRARY

A COLLECTION OF NEW STUDIES USING EXISTING AND PROPOSED

TECHNIQUES AND INSTRUMENTATION FOR NONDESTRUCTIVE

TESTING AND ANALYSIS OF CONCRETE

MATERIALS AND STRUCTURES

by

Shane D. Boone

A dissertation submitted in partial fulfillment
of the requirements for the degree

of

DOCTOR OF PHILOSOPHY

in

Civil and Environmental Engineering

Approved:

_____ _____
Paul J. Barr   Marvin W. Halling
Major Professor   Committee Member

_____ _____
James A. Bay   Kevin C. Womack
Committee Member   Committee Member

_____ _____
Thomas H. Fronk   Byron R. Burnham
Committee Member   Dean of Graduate Studies

UTAH STATE UNIVERSITY
Logan, Utah

2008

ABSTRACT

A Collection of New Studies Using Existing and Proposed Techniques and

Instrumentation for Nondestructive Testing and Analysis of Concrete

Materials and Structures

by

Shane D. Boone, Doctor of Philosophy

Utah State University, 2008

Major Professor: Dr. Paul J. Barr
Department: Civil and Environmental Engineering

A variety of studies were performed using existing and newly proposed

techniques and instrumentation to further the understanding of nondestructive testing of

concrete. A new combined stress wave propagation method was developed that

combined the existing methods of the spectral analysis of surface waves, impact echo,

and free-free resonant column experimental and analysis techniques. The method was

used to determine the stiffness profile and location of embedded voids in a concrete

tunnel lining modeled as a three layer concrete slab.   A new equation was proposed that

predicted the level of damage of concrete samples based on the functions of the change in

first mode longitudinal frequency and the absorption of energy during cyclic loading to

failure. During this study, new instrumentation was developed that aided in the dynamic

stiffness measurements during the cyclic loading. A comparison of the static and

dynamic Young's modulus was performed. It was found that the ratio of these two

moduli depend on a concrete's strength and damping properties as well as the age of the specimen. A new equation was proposed using these three properties to determine the ratio of static to dynamic Young's modulus. An experimental program was performed on samples of high performance self-consolidating concrete (HPSCC). The HPSCC exceeded expected values of strength and stiffness over that of regular high performance concrete. Finally, a comparison of prestress losses in prestressed bridge girders fabricated using the HPSCC was conducted. Prestress losses were measured and calculated using the American Association of State Highway and Transportation Officials (AASHTO) LRFD 2004 and 2007 Specifications. It was determined that the AASHTO LRFD 2007 Specifications most accurately predict the measured prestress losses.

(225 pages)

DEDICATION

This dissertation is dedicated to my wife, my family, my friends, and all others that supported me during these past three years. The appreciation I have for the motivation and confidence that has been bestowed upon me by these people is unimaginable.

<div style="text-align: right">Shane D. Boone</div>

ACKNOWLEDGMENTS

CONTENTS

LIST OF TABLES

LIST OF FIGURES

CHAPTER 1

INTRODUCTION, OBJECTIVES, AND ORGANIZATION

Introduction

Concrete is one of the most commonly used construction materials in the world. All types of structures, including residential, commercial, and even nuclear facilities, are constructed using concrete. In addition, the majority of the infrastructure in the United States is comprised of concrete structures. Most of these structures have been subjected to years of loading, fatigue, and deterioration. Because of this in-service condition, many concrete structures have exceeded their design life and are thought to be in need of replacement. However, many structures that might be considered for replacement are in acceptable condition with respect to their original design requirements or even the design requirements set forth by newer codes. Thus, it is of great importance that structural engineers have the capability to measure the properties of the in-place concrete to determine its acceptability with regards to current specifications. In instances in which damage is measured, there is a need to evaluate and quantify the extent of the damage. These capabilities should come from proven nondestructive techniques that can be used in combination or in solitary along with a complete understanding of the behavior of the material under a variety of loading conditions to provide meaningful and accurate quantitative experimental data. Finally, it is of great importance to understand the behavior of new structures and how existing design specifications predict their behavior.

For structural engineers, nondestructive evaluation techniques are available in a large variety. The original method, which is still frequently used, is visual inspection.

Visual inspection is a good tool for any engineer, but is highly subjective and does not provide any quantitative data. Thus, procedures that can provide data with regards to a structure's material properties are desirable. Some of the most widely used quantitative nondestructive testing techniques for concrete involve the basic theories of elasticity to measure and quantify in-place material properties through stress wave propagation and in-place strain measurements.

Although the experimental and analytical techniques utilized by these methods are well developed, the dynamic material properties and subsequent behavior of concrete must be understood for these methods to continue to play a progressive role in the evaluation of concrete. Also, the methods and applications of many of the existing techniques can be expanded upon for situations that have previously not been considered. Finally, some existing methods can be combined to develop more efficient techniques of experimental and analytical evaluations.

Objectives of the Research

The objective of this research was to provide a more complete understanding of the dynamic material properties of concrete and to develop new testing equipment, new experimental and analytical techniques, and an expanded knowledge to the extent that the methods of nondestructive testing can be used. Because of the complex nature of the stress wave propagation methods, a large portion of the research was performed to gain a complete understanding of the testing apparatus and techniques along with the individual analysis required for each method. Once this knowledge was acquired, progressive research was performed. Three studies were executed.

The first study involved the combined use of the spectral analysis of surface waves (SASW), impact echo (IE), and free-free resonant column (FFRC) methods to develop a newly proposed method named the Combined Stress Wave Propagation (CSWP) method. The newly proposed method was used to determine the behavior of stress waves passing through a concrete tunnel lining modeled as a multilayered concrete slab. The slab was composed of three layers of varying stiffness and contained embedded voids. The combination of IE and SASW experimental and analytical techniques, along with FFRC testing performed on laboratory specimens provided all of the essential dynamic properties of the concrete slab. As such, no material assumptions were required during the analysis. The combined method proved to be more efficient while obtaining more data than any of the individual methods could have if performed alone.

The second study involved the development of a new technique to quantify damage in concrete cylinders as a function of the variation in dynamic stiffness, damping, and energy absorption. A new device was created to excite concrete specimens at a wide range of frequencies while under a compressive load. Using this device, dynamic stiffness properties were measured as cylinders were subjected to loading cycles at increasing percentages of their ultimate compressive strength until failure. Simultaneously, data was measured to create hysteretic curves of the loading cycles and calculate energy absorption in the material. This new data was used to develop a better understanding of the behavior of concrete under fatigue loading and to develop a damage model involving dynamic stiffness and energy absorption.

The third study utilized embedded Vibrating Wire Strain Gauges (VWSG) to measure the change in strain in high strength, self-consolidating concrete (SCC), prestressed bridge girders.   The strains measured using the VWSGs were used to determine prestress loss and were compared to calculated values obtained using the American Association of State Highway and Transportation Officials (AASHTO) design Specifications. Because of the high strength of the SCC, the prestress losses calculated using the AASHTO design practices were overestimated in this case. This study shows that current AASHTO design specifications are improving with regards to the prediction of prestress loss in high performance concrete bridge girders, and that prestress losses for high strength SCC can be predicted with them.

During each of these three studies, the constant measurement of static and dynamic Young's modulus of a multitude of concrete mixes was being performed. Several concrete mixes that included low, normal, and high strength concretes composed of varying aggregate sizes were tested. FFRC tests were used to measure the longitudinal first mode of vibration frequencies of the specimens. Specimens were then subjected to both low and high strain static tests. Comparing the two data sets shows a correlation between the static and dynamic values of Young's modulus as a function of concrete strength. Also, a new method to calculate dynamic Young's modulus from statically measured stress-strain curves is proposed.

Report Organization

In Chapter 2, the basic principles of wave theory in elastic, isotropic materials are presented. A history of the use of stress wave propagation techniques on concrete

materials is described. Also, the evolution of these techniques into the SASW, IE, and FFRC methods along with previous research successes and the experimental and analysis procedures for each is outlined. The limited literature regarding the combination of the SASW and IE methods is discussed. Previous research on the quantitative assessment of damage in concrete structures is summarized. Finally, existing research concerning the measurement of strain in high performance prestressed concrete bridge girders is discussed.

Chapter 3 describes the experimental and analytical methods that were performed on a concrete tunnel lining modeled as a three layer slab. The purpose of this study was to demonstrate the effectiveness of the newly proposed CSWP method. Measured and calculated results obtained by using the newly proposed method are presented.

The investigation of several concrete specimens made using two high performance SCC (HPSCC) mixes to fabricate a series of prestressed concrete bridge girders is presented in Chapter 4. The investigation measured compressive strength, static Young's modulus, and drying shrinkage as a function of time. Results indicate that these concretes exhibit strength and stiffness far beyond that of even high performance concrete. Drying shrinkage results indicate that the HPSCC measured exhibits shrinkage characteristics within the range of other SCCs reviewed in existing literature.

Chapter 5 describes the development of a new instrument used to measure longitudinal modes of vibration on concrete specimen. The device was used to determine the changes in dynamic stiffness and damping of concrete specimen subjected to cyclic loading to failure. The results of the variation in dynamic stiffness and energy absorption during cyclic loading to failure along with a proposed damage model are discussed.

In Chapter 6, the installation, measurements, analysis, and results of embedded VWSGs in high strength, SCC, prestressed bridge girders are described. The use of these measurements and results provides data to show that the current AASHTO design parameters are improving and can be used to predict prestress losses in high strength SCC girders.

The behavior of a multitude of concrete specimens under a variety of strain conditions is discussed in Chapter 7. The results allow a comparison of the behavior between the static and dynamic Young's modulus of concrete at different values of stress and a proposed method to determine the dynamic Young's modulus using static measurements is proposed.

Finally, summary, conclusions, and recommendations are presented in Chapter 8.

CHAPTER 2

LITERATURE REVIEW

Basic Wave Principles of Isotropic Elastic Media

Multiple types of stress waves radiate through an elastic medium resulting from a loaded region with finite velocities and propagation. As discussed in the methods of stress wave propagation measurements, a load is typically of finite duration and results in a multitude of transient waves that cause a disturbance throughout the material. When the material is homogenous, the relationship between the wave velocity and physical properties of the material can be explained based on the theory of propagation of waves in elastic isotropic media. In the case of a heterogeneous material like concrete, the assumption that it is homogenous must be assumed so that the following equations are valid (Timoshenko and Goodier 1970):

$$E_d = \frac{(1+\upsilon)(1-2\upsilon)}{1-\upsilon} M_d \qquad (2.1)$$

$$E_d = 2(1+\upsilon)G_d \qquad (2.2)$$

$$V_p = \sqrt{\frac{E_d(1-\nu)}{\rho(1+\nu)(1-2\nu)}} \qquad (2.3)$$

$$V_s = \sqrt{\frac{G_d}{\rho}} \qquad (2.4)$$

where: E_d = dynamic Young's modulus of the concrete

M_d = dynamic unconstrained modulus of elasticity

G_d = dynamic shear modulus of the concrete

υ = poisson's ratio of the material

V_p = compression wave velocity of the material

ρ = mass density of the material

V_s = shear wave velocity of the material;

It should be noted that although Eqs. (2.1) and (2.2) are described in terms of dynamic moduli, the same relationships also are valid for the static moduli. The dynamic conditions refer to a deformation condition in which strains are of the order of 0.001 percent or less (Stokoe et al. 1994).

When transient waves move between two layers of material that have different properties, reflection and refraction occur. Eqs. (2.3) and (2.4) provide the relationship between compression and shear wave velocities and the material properties. The reflected and refracted wave amplitudes depend entirely upon the ratio of these properties, known as the impedance ratio, α, of one material to the other (Eqs. (2.5) and (2.6)). Also, if the wave is not normal to the incident surface, the angle at which it reflects or refracts is also dependent on both the impedances of the materials and the angle of incidence which follows Snell's law (Fig. 2.1). These relationships are described as follows (Kramer 1996):

$$\alpha = \frac{\rho_2 V_2}{\rho_1 V_1} \qquad (2.5)$$

$$\sin \beta = \frac{V_2}{V_1} \sin \theta \qquad (2.6)$$

where: ρ_2 = mass density of the material upon which the wave is incident

V_2 = the wave velocity of the material upon which the wave is incident

ρ_1 = mass density of the material through which the incident wave travels

V_1 = the wave velocity of the material through which the incident wave travels

β = the angle at which the wave is refracted

θ = the angle of incidence.

When the impedance ratio at the interface of a surface is zero, as in the case of a concrete to air interface, stress waves cannot be transmitted into the second medium and there is a complete reflection at the surface and no refraction. There is also a nearly complete reflection of the incident wave when the impedance ratio at the interface is very high, as in the case of a soft soil to bedrock interface. In the latter case, however, the wave's amplitude is nearly doubled and there is little to no energy transferred into the higher modulus material in the form of a refracted wave. For this reason, energy is "trapped" in layers of lower modulus that are between layers of higher modulus (Kramer 1996).

$$\sin \beta = \frac{V_2}{V_1} \sin \theta$$
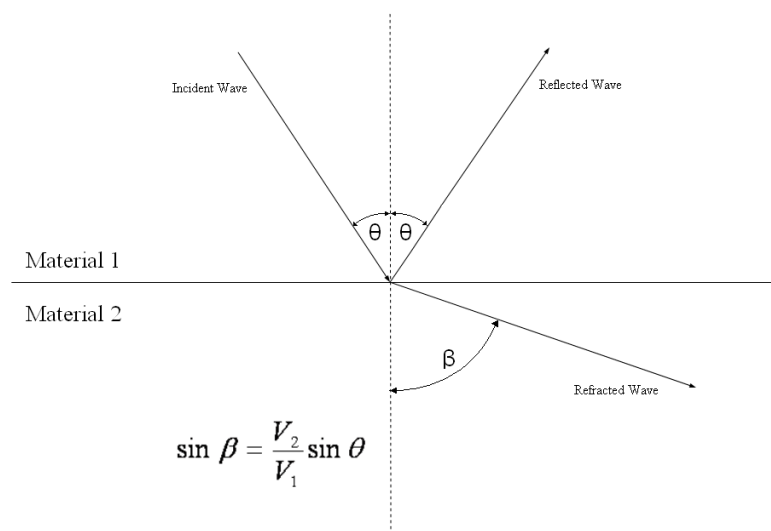
Fig. 2.1. Reflected and refracted waves caused by an incident wave

It is important to note that the angles of incidence and refraction of both shear and compressive waves act in the manners described in Eqs. (2.5) and (2.6). However, because shear waves propagate at a lower velocity than compression waves, when a compression wave acts upon an interface of dissimilar media, shear waves are reflected and refracted at different angles than the reflected and refracted compression waves. The interaction of these waves causes multiple reflections from wave interactions along with reflections from surfaces. This interaction also causes the combination of waves and multiple modal disturbances (Joh 1996).

**History of the Use of Stress Wave
Propagation Techniques in Concrete**

Work with stress wave propagation in arbitrary materials began as early as 1877 when Lord Rayleigh reported "the mathematical relationships existing between the velocity of sound through a [material] specimen and its resonant frequency and the relationship of these two to the modulus of elasticity of the material" (Rayleigh 1976). These relationships, which are acoustical in nature, essentially laid the groundwork for dynamic testing of concrete using stress wave propagation. The relationship that Rayleigh described is:

$$V = f\lambda \tag{2.7}$$

where: V = velocity at which a wave travels through a material

f = Associated wave frequency

λ = associated wavelength.

In 1938, T.C. Powers, was able to determine the resonant frequency of concrete samples by supporting them at their nodal points, striking them with a hammer, and

matching the musical tone produced with a calibrated tone source. This progressed in the late 1930's and 1940's when a number of researchers improved the technique using electronic equipment to match the tones and determine the resonant frequency (Powers 1938; Hornibrook 1939; Obert and Duvall 1941; Stanton 1944). These processes have all evolved and given rise to both the impact echo (IE) and free-free resonant column (FFRC) methods.

Jones (1953, 1962) reported on the use of a method that used Rayleigh surface waves to determine the stiffness profile of pavements and underlying layers. This method, called the steady-state Rayleigh-wave method, used vertically oriented vibrators to produce a source vibration of a known frequency. A sensor was then moved gradually away from the source until the vertical surface motion of the source and the sensor were in perfect phase (Fig. 2.2).

Fig. 2.2 depicts different scenarios within a single steady-state Rayleigh-wave experiment. The waveform shown would be the motion of the vibrator induced surface wave due to Rayleigh like displacements in a 2D model. For this particular waveform, receivers 1 and 4 are in phase, and receivers 2 and 3 are not. Because the frequency of the vibrator and the distance between the two receivers that in phase are known, the Rayleigh wave velocity, V_R, can be calculated as follows (Richart et al. 1970):

$$V_R = \lambda \, f \qquad\qquad (2.8)$$

where: V_R = Rayleigh wave velocity

f = known frequency of vertical vibrator

λ = wavelength (spacing between the source and receiver).
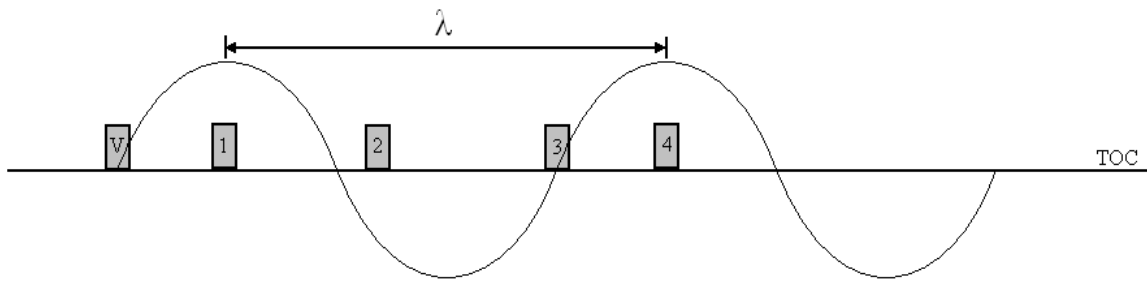
Fig. 2.2. Steady state Rayleigh wave method

where: V = Vibration source

1, 2, 3, 4 = various positions of receivers

TOC = top of concrete.

After these findings, there was little research done in this stress wave propagation

area until the early 1980's when researchers at the University of Texas at Austin began

using impulse and swept-sinusoidal vibrators to produce excitations to soil surfaces. By

incorporating two vertically oriented receivers, the researchers could record the

displacement-time record induced by the excitations caused over a range of frequencies.

Using a Fast Fourier Transform Algorithm, the digital time record from each receiver was

transferred into a frequency domain record whereby the phase difference between the two

signals was calculated.   This method was called the spectral analysis of surface waves

(SASW) (Stokoe et al. 1994).

Impact Techniques

Stress wave propagation testing techniques, when applied to concrete, typically

utilize an impact created by a hammer or small steel ball to create a short duration

impulse. This impact, depending on its contact time, creates an impulse that sends

various body and surface waves of different frequencies and wavelengths throughout the system. Typically, when a hammer is used, the hammer can be instrumented such that an amplitude time record of the impact can be recorded. From this impulse record, the range of frequencies created in the concrete can be determined. However, when a steel ball is used, the contact time of the impact produced is determined as (Goldsmith 1965):

$$T_c = 5.97 \left[\rho_s \left(\delta_s + \delta_p \right) \right]^{2/5} \frac{R}{(h)^{0.1}} \tag{2.9}$$

$$\delta_p = \frac{1 - v_p^2}{\pi E_p} \tag{2.10}$$

$$\delta_s = \frac{1 - v_s^2}{\pi E_s} \tag{2.11}$$

where: T_c = contact time

ρ_s = density of the sphere

R = Radius of the sphere

h = drop height

v_p = Poisson's ratio of the plate

v_s = Poisson's ratio of the sphere

E_p = Young's modulus of elasticity of the plate

E_s = Young's modulus of elasticity of the sphere

The actual contact time may vary due to the lack of uniformity of most concrete surfaces (Carino et al. 1986). However, it is only necessary to calculate the contact time of an impact source if a measurement of a specific frequency yields small amounts of energy. In most cases, multiple impact sources are used to create a wide range of frequency excitations, and the need to calculate contact time is negated.

For impact techniques, the receiver is typically a velocity transducer or an accelerometer. In the case of concrete, the receiver is almost always an accelerometer. Accelerometers are typically piezoelectric devices. Piezoelectric devices are generally manufactured ceramic materials that, when subjected to an electric charge will deform. Also, when subjected to deformation of any kind, the device will create an electric charge whose magnitude is proportional to the deformation. Thus, a piezoelectric accelerometer, when subjected to the response of a transient stress wave, generates an electrical output that is proportional to the acceleration associated with the response. This quality makes piezoelectric accelerometers an ideal device for measuring the response of concrete elements exposed to transient stress waves caused by impact induced excitations.

The Impact Echo Method

This section discusses the history of the IE method along with previous research successes. The experimental and analysis procedure for the method is also provided.

Background

The IE method is a stress wave propagation testing technique used to determine the depth and compression wave velocity of concrete elements. The method uses the detection of transient resonance conditions caused by the multiple reflections of compression waves to determine the soundness of a concrete element. It has been used to detect flaws in concrete including honeycombing, voids, cracks, and shallow delaminations in plate, circular, square, rectangular bars, and hollow cylinder structural geometries (Sansalone 1997).

The method's development began in the early 1980's by Dr. Nicholas Carino, Dr. Nelson N. Hsu, and Mary Sansalone at the Structures Division of the National Bureau of Standards. The team, led by Dr. Carino, developed the method over the period of several years into a complete technique for flaw detection in concrete elements.

The IE method evolved from the pulse-echo method. In the early 1960s, research using the pulse-echo method for flaw detection in concrete was performed. The pulse-echo method uses a transmitter set on the surface of a concrete element to create stress waves at a constant frequency that moved through the concrete. The surface response to these stress waves was then measured by either the same transmitter acting as a receiver or another transmitter, located near the source, acting solely as a receiver. The method, dependent on the source-receiver setup was known as either the true pulse-echo or the pitch catch method, respectively (Fig. 2.3). The setup used an oscilloscope to view and then measure the travel time of the pulse created by the source transmitter. From this measured time domain, the compression wave velocity could be found from (Malhotra and Carino 2000):

$$T = \frac{1}{2}(\Delta t)V_p \qquad (2.12)$$

where: T = thickness of the material

Δt = travel time between the initiation of the source pulse and the reception of that pulse.

Although this method was capable of detecting the thickness and compression wave velocities of sound concrete elements, it was determined that the equipment required to both produce and receive an impulse wave was not realistic. The
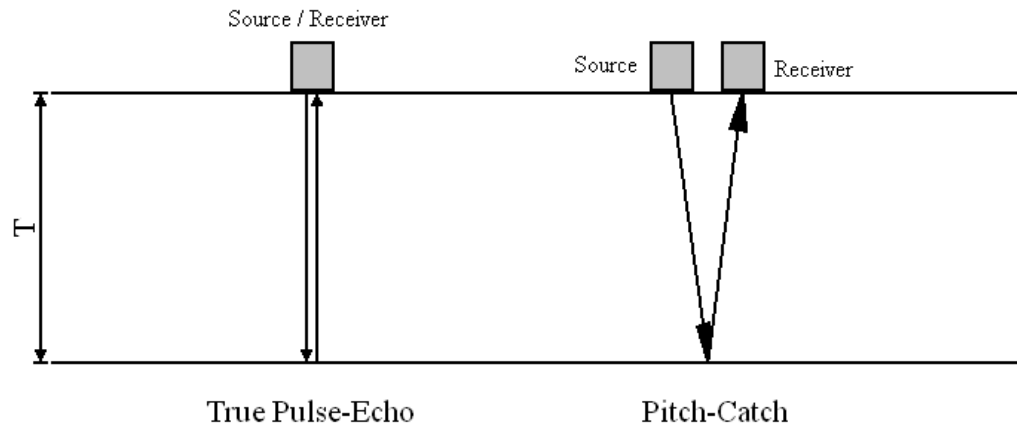
Fig. 2.3. Source-receiver setups and nomenclature for the pulse-echo method

transmitters and receivers used in the pulse-echo method are piezoelectric transducers

that can generate and receive responses created by the propagation of transient stress

waves. However, when a piezoelectric transducer is excited by an electric charge it does

not instantaneously change shape and return to its original state. Nor does it produce a

singular electric impulse upon being deformed. Instead, the device oscillates from its

deformed state back to its original state according to the damping factor of its specific

material. In order to accurately measure the displacement time record of a concrete

element excited by transient stress waves it is ideal to have a finite impulse duration.

Thus, a high excitation frequency is required to ensure that the element has finished

oscillating before the first reception of the stress waves is recorded. If the element has

not returned to its original state, but is still oscillating, it becomes very difficult to

distinguish the reflected stress waves from the impulse waves. If, instead, a transmitter

and receiver pair is used instead of a sole transmitter-receiver, problems arise from the

attenuation of the body waves and the radiation pattern of the stress pulses determined by

the ratio of the transducer diameter to the wavelength of the transmitted waves.

Because little success was achieved using the pulse-echo method, Carino and his team began experimentation with an impact source. A finite-element model was created that simulated the impact-echo response of structures. Early results showed good reliability when compared to known solutions for impacts on infinite plates and experiments carried out on design specimens (Sansalone and Carino 1987). These initial experiments led to continued computer simulations that created a wealth of understanding with regards to how multitudes of structural geometries are affected by impact related stress waves. Further research showed how internal flaws affected the solution of these problems and it was quickly realized that this method was ideal not only for the determination of thickness and wave velocity but also the detection of internal flaws in concrete elements (Sansalone and Carino 1986).

Using steel spheres as impact sources and what has now developed into the digital signal analyzer, IE researchers initially studied the displacement time record to recognize the arrival of different body waves (Sansalone 1986). However, the method realized its final breakthrough when the researchers discovered that problems inherent in interpreting time domain records could be easily resolved by transferring the data into the frequency domain using a Fast Fourier Transform (FFT).

The inherent success of the IE method is due to the reflective nature of transient stress waves. As mentioned above, a compression wave reflects from an interface of dissimilar media. In the case of a compression wave incident at an interface of concrete and air, the amplitude of the reflected wave is almost exactly equal to the amplitude of the incident wave. Thus, when a compression wave is normal to such an interface, the reflection of that wave between the impact source and the opposite boundary causes a

peak in the frequency domain plot (Fig. 2.4). This peak can be analyzed and is

determined to be the detection of transient resonances caused by body waves reflecting

off either boundary surfaces or internal flaws (Sansalone 1997):

$$F = \frac{\beta V_p}{2(T)} \tag{2.13}$$

where: F = Frequency of the first transient mode, Hz

β = Cross section geometry correction factor

$\beta \approx 0.96$ for plates

$\beta \approx 0.92$ for circular columns

$\beta \approx 0.87$ for square columns or beams

$\beta \approx 0.96$ for hollow cylinders

Using this fundamental equation and varying experimental setups, procedures for

determining minimum crack widths in concrete elements (Cheng and Sansalone 1995),

determining interfacial bond quality (Lin and Sansalone 1996), determining depth of

surface-opening cracks (Sansalone et al. 1998), and evaluating early-age concrete

strength (Pessiki and Johnson 1996), among many others, have been developed.

Relationships between velocity and strength as a function of time for normal and high

strength concrete have been developed (Lee et al. 2003). The effect of Poisson's ratio on

the analysis has been studied (Popovics 1997). Commercial model field instrumentation

has also been developed and a U.S. patent is in place for a "Nondestructive Materials

Testing Apparatus and Technique for Use in the Field" that is essentially the IE method

(Sansalone 1997).

Studies have also been performed that incorporate the use of horizontally polarized shear, SH, waves into the IE method. In this method, a shear wave is produced at the surface of a concrete plate and horizontally polarized receivers measure the predominant frequency. The IE method using SH waves does not require a geometric correction factor as described in Eq. (2.13) (Cho 2005).

In summary, the IE method is one of the most utilized and proven stress wave propagation methods used for nondestructive testing of concrete structures. Consequently, the method, as it applies to concrete plate like structures was designated as the "Standard Test Method for Measuring the P-Wave Speed and the Thickness of Concrete Plates Using the Impact Echo Method" by the American Standard for Testing and Materials (ASTM 1998) C 1383.
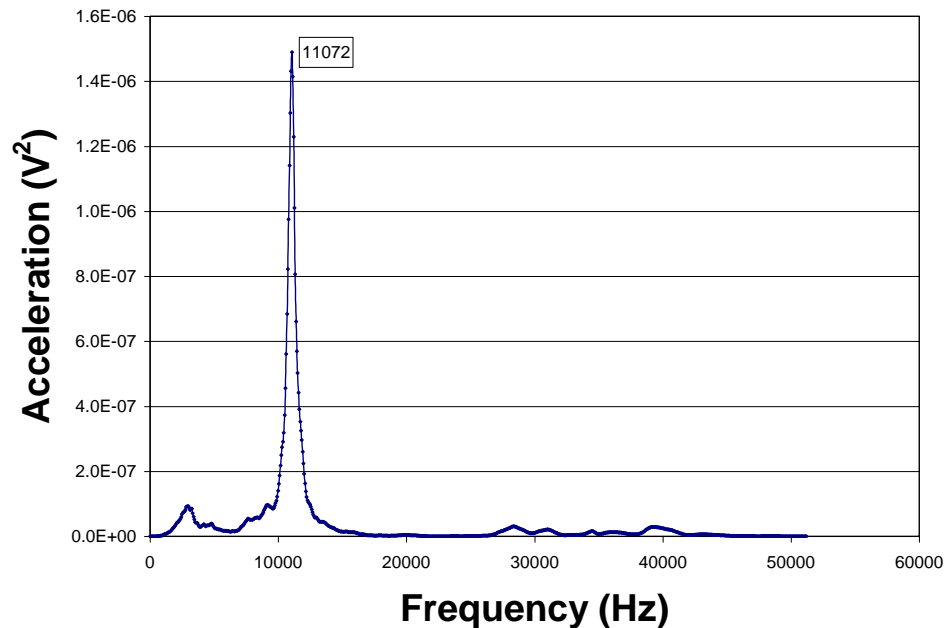
Fig. 2.4. Peak in frequency domain during impact echo testing

Experimental Procedure and Analysis

The experimental procedure for the IE method on concrete involves the use of an impact source (typically an instrumented hammer or small steel spheres), a receiver (typically a piezoelectric accelerometer), and a digital signal analyzer (Fig. 2.5).

Like any experiment, it is important to plan the specific technique that will be used during any IE test. For instance, if a thick slab is to be tested, it is important that the impact source be capable of producing low enough frequencies (long wavelengths) to travel the entire thickness of the slab.

(a) Large instrumented hammer

(b) Small instrumented hammer

Fig. 2.5. Equipment used for stress wave propagation testing

(b) Accelerometer
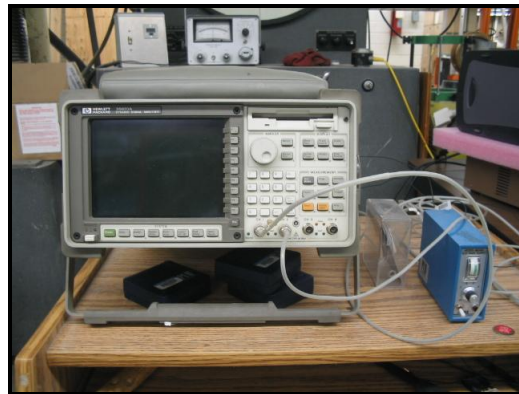
(d) Digital signal analyzer
Fig. 2.5. (continued)

Also, if the slab is thought to have flaws, several different impact sources may be required to ensure that a large range of frequencies are produced that can travel to different depths of the slab more precisely. A transducer that can measure a large range of frequencies is also beneficial as it will be capable of measuring responses from a multitude of impact sources and associated excitation frequencies.

If small steel spheres are used as an impact source, the frequencies can be calculated using Eq. (2.9). In the event that an instrumented hammer is being used, the response time history of the impact can be recorded and the approximate frequencies imparted due to the impulse can be calculated as the inverse of the contact time.

Although the frequencies imparted into the structure do not affect the analysis, it is often helpful, as mentioned above, to know what frequencies are abundant, and which are not.

In the case of a concrete slab, an array of test points should be designed to encompass the entire surface of the slab (Fig. 2.6). The receivers are then connected to the slab using a coupling (gels, adhesives, etc.) at each test point. A spacing of approximately 2 in., but no more than 0.4 times the thickness of the element being measured, is recommended between the impact source and the receiver (Sansalone 1997). Impacts are made adjacent to each receiver and the digital signal analyzer records the response time history. The time record is then transformed into the frequency domain using a FFT and analysis can begin using Eq. (2.8).

For each test point, an amplitude spectrum is assigned from frequency domain measurements. From these amplitude spectra, analyses are performed using Eq. (2.13) and cross sections of the slab can be constructed. These cross sections identify the depth of, and any internal flaws included in, the slab.

• => Impact Point
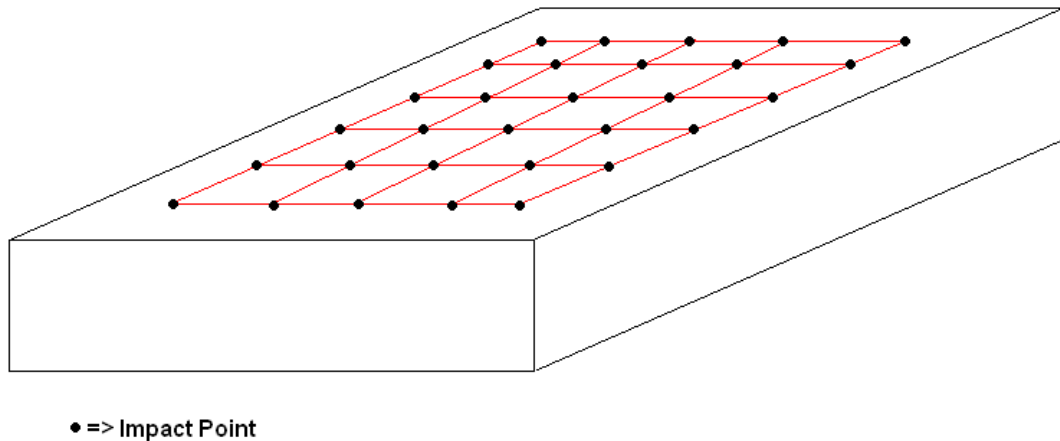
Fig. 2.6. Testing array for IE on a slab

The Spectral Analysis of Surface Wave Method

In this section, the development of the SASW method along with previous research successes is discussed. The experimental and analysis procedures for the method are also outlined.

<u>Background</u>

The SASW method is a technique that has been typically used to determine the stiffness and depth profiles of layered soil and pavement systems. The propagation of velocity of a surface wave varies with wavelength and frequency. This characteristic is called dispersion. It is the dispersive characteristic of surface waves of the Rayleigh type that is measured with the SASW methodology (Kalinski et al. 1994). The technique uses spectral analysis to evaluate the velocity of these surface waves at different frequencies and theoretical modeling of layered systems to determine velocity profiles (Stokoe et al. 1994). The technique was developed in the 1980's by researchers at the University of Texas at Austin and was first used as a nondestructive technique to evaluate profiles of pavement systems (Nazarian 1984) and soil profiles (Nazarian 1984; et al. Stokoe 1994). Because of its success in pavement systems, the use of the method has grown to also include concrete structures.

The most relevant research to date on concrete structures includes research on portland cement concrete (PCC) slabs (Bay and Stokoe 1990; 1992), high performance concrete (Cho 2003), concrete tunnel linings (Kang et al. 2006), damaged concrete beams (Kalinski et al. 1994), and a mass concrete placement (Boone 2005), among others.

Experimental Procedure and Analysis

The experimental setup for the SASW testing incorporates an impact source, multiple receivers (typically vertically oriented velocity transducers or accelerometers), and a digital signal analyzer (Fig. 2.7). Typically receivers are set up in either a common receiver midpoint (CRM) geometry or common source (CS) geometry (Fig. 2.8). For the common receiver midpoint geometry, an impact is produced so that waves will travel from receiver 1 to receiver 2, and then also so that waves will travel from receiver 2 to receiver 1. The receivers spacing is then expanded and the process is repeated. For the common source geometry, only one impact is produced and waves travel from receiver 1 to receiver 2. Initial spacing of the receivers is based on assumed knowledge of the profile being tested. In the case of concrete the spacing primarily depends on aggregate size for a minimum spacing and the thickness of the material for a maximum spacing. As mentioned above, the minimum size wavelength that can accurately be measured depends essentially on the aggregate size and spacing of the receivers.
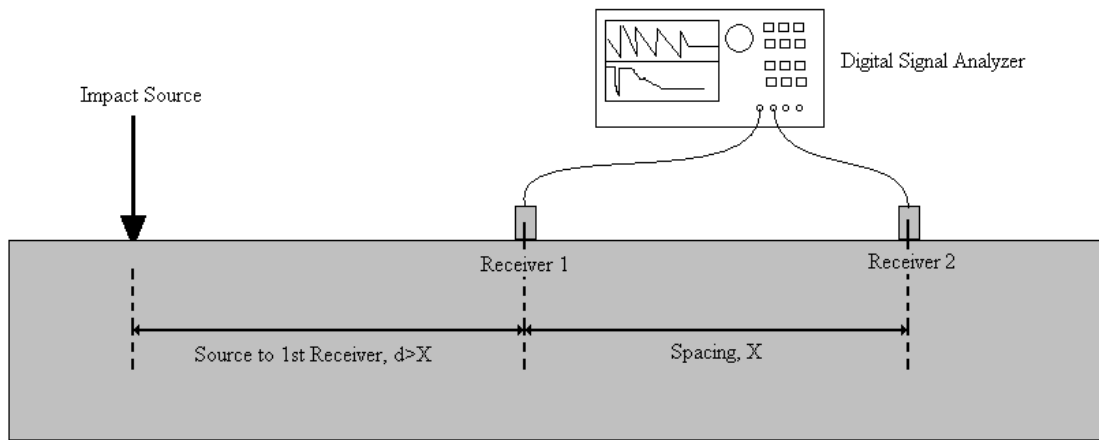
Fig. 2.7. Experimental setup for SASW

(a) CSM geometry

(b) CS geometry
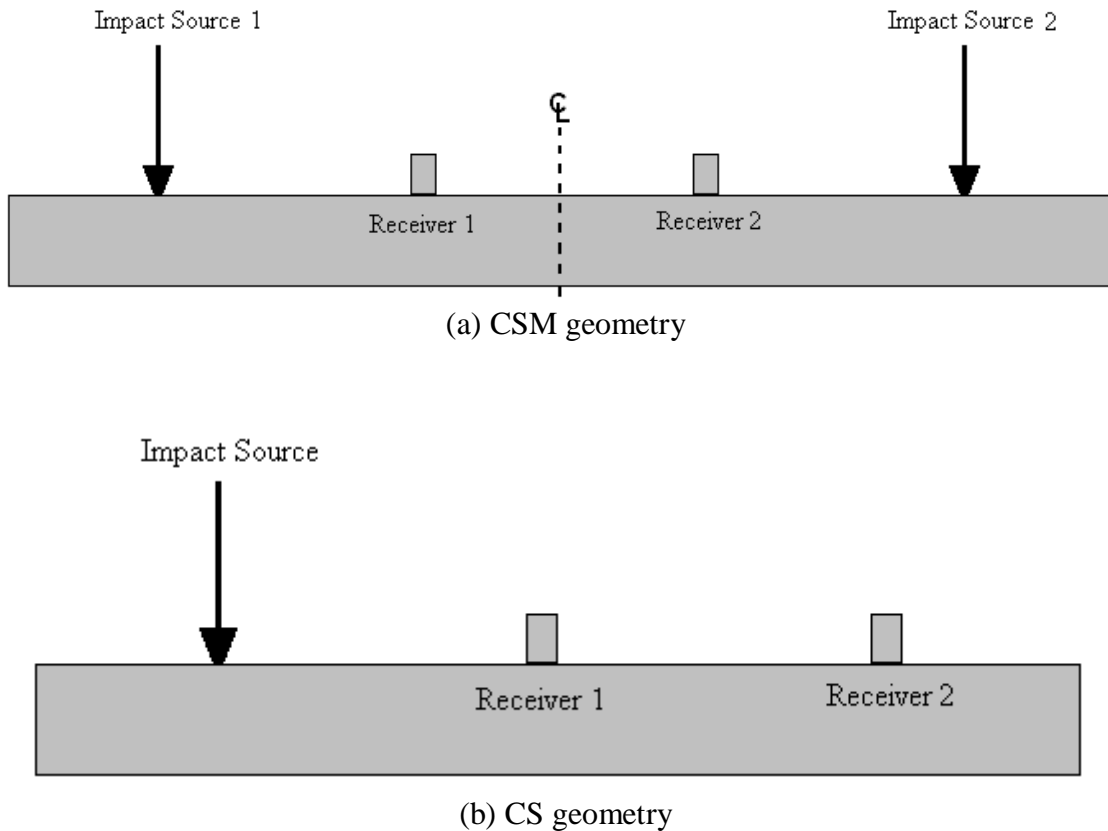
Fig. 2.8. Variations of SASW receiver and impact setup

Thus, the minimum spacing of the receivers should be at a distance equal to three times the maximum aggregate size. Also, velocities of waves having wavelengths greater than two times the receiver spacing should not be considered due to near field effects. Near field effects refers to an underlying principle in the theory of the SASW method that assumes that at least one full Rayleigh waveform is developed between receivers. Subsequent spacing should be set by doubling the initial increment (i.e. 3 in., 6 in., 12 in., etc.). Multiple spacings of the receivers are required to provide enough data to completely determine the profile of the structure being tested. In the case in which there is no initial information with regards to aggregate size, a good starting spacing is of the

order of 2 – 3 in. This spacing is based on an assumed aggregate size of ¾ in. or smaller

and an impact source capable of creating an excitation of 20 kHz.

An impact is produced using a device capable of exerting a short duration

impulse. Typical impact sources are small steel spheres, ball peen hammers, and steel

hammers of various sizes. As mentioned in Section 2.3, the size and duration of the

impact affects the excitation frequency imparted to the material. In accordance with Eq.

(2.7), the depth of material tested depends on the receiver spacing, which determines the

wavelength, λ, and the impact, which determines the frequency, f. Thus, based on a

constant material velocity, receiver spacing and impact frequency determine the depth of

the material being measured.

The digital signal analyzer is used to record vertical motion at each of the two

receiver locations in the time domain as transducer voltage. Assuming there are two

receivers, these records shall be denoted as x(t) and y(t) for receivers 1 and 2,

respectively. The two time domain records are then transformed into the frequency

domain, X(f) and Y(f), using a Fast Fourier Transform.

These two signals are then multiplied together to create the power spectra and

cross power spectrum as follows:

$$G_{xx} = X(f)X^*(f) \qquad (2.14)$$

$$G_{yy} = Y(f)Y^*(f) \qquad (2.15)$$

$$G_{xy} = X(f)Y^*(f) \qquad (2.16)$$

where: G_{xy} = cross power spectrum

* denotes the complex conjugate of the quantity.

Using these values the phase and coherence functions of the cross power spectrum

can be calculated as (Stokoe et al. 1994):

$$\phi = \phi(x) - \phi(y) = \tan^{-1}\left(\frac{Im(G_{xy})}{Re(G_{xy})}\right) \tag{2.17}$$

$$\gamma^2 = \frac{|G_{xy}|^2}{G_{xx}G_{yy}} \tag{2.18}$$

where: ϕ = phase difference between the two receivers

Im denotes the imaginary part of the cross power spectrum

Re denotes the real part of the cross power spectrum

γ^2 = coherence function

The phase difference between the two receivers represents the number of cycles

that a waveform of a given frequency completes as it passes from one receiver to another.

On a periodic waveform, such as that shown in Fig. 2.9, the phase difference between

two points can be calculated as:

$$\phi = \frac{\Delta t}{T}(360°) \tag{2.19}$$

By calculating each value of phase using Eq. (2.17), a wrapped phase spectrum is

created (Fig. 2.10). Wrapped phase differences vary between -180° and 180°, and the

phase values repeat themselves every 360°.

The coherence function is a measure of the power in the output signal caused by

the input. Thus, if the coherence is 1, then all the output power is coming from the input

and there is a high signal-to-noise ratio.
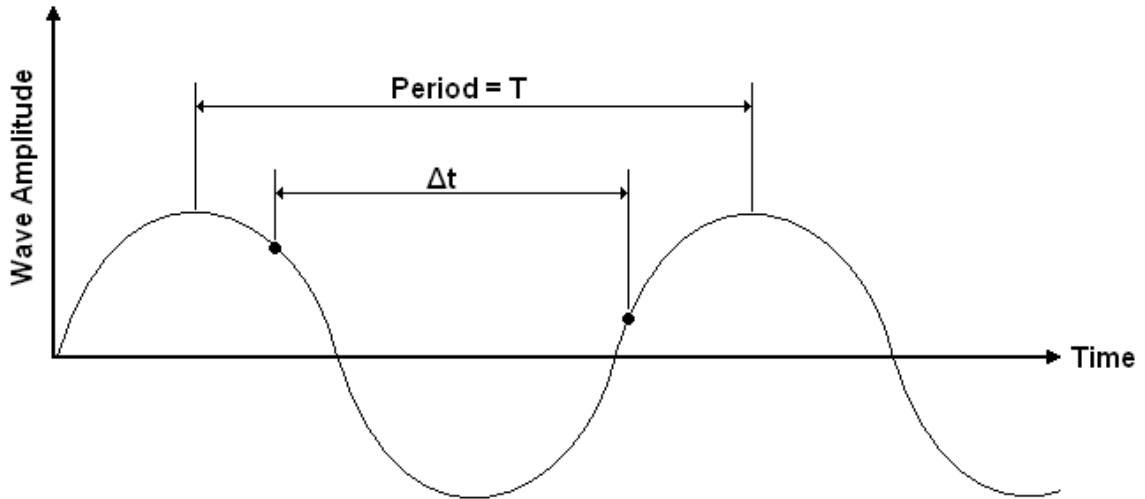
Fig. 2.9. Phase difference between two points on a waveform

If the value is 0 then there is no output energy caused by the input and there is a very low

signal to noise ratio. Thus, by calculating the coherence during the testing period, a

determination of the quality of the measurement over a variety of frequencies can be

quantified (Stokoe et al. 1994).

The first step in the analysis of the data measured using the SASW method is a

creation of an experimental dispersion curve.   A dispersion curve is a plot of phase

velocity versus wavelength and is created using the unwrapped phase spectrum. The

unwrapped phase spectrum is created by cumulatively adding the phase angles from the

wrapped phase spectrum every 360° (Fig. 2.11). The number of cycles a waveform

completes between each receiver is determined using the unwrapped phase spectrum.

Thus, for each frequency, the travel time between the receivers, the velocity of the

surface waves, and the wavelength corresponding to a specific frequency can be

calculated from this unwrapped phase spectrum as follows:

$$\Delta t_f = \frac{\phi}{360f} \qquad\qquad (2.20)$$

$$V_{R(f)} = \frac{X}{\Delta t_f} \tag{2.21}$$

$$\lambda(f) = \frac{V_{R(f)}}{f} \tag{2.22}$$

where: Δt_f = travel time between receivers

ϕ = phase difference between the two receivers

$V_{R(f)}$ = phase velocity

X = spacing between the two receivers

$\lambda(f)$ = wavelength corresponding to a specific frequency.
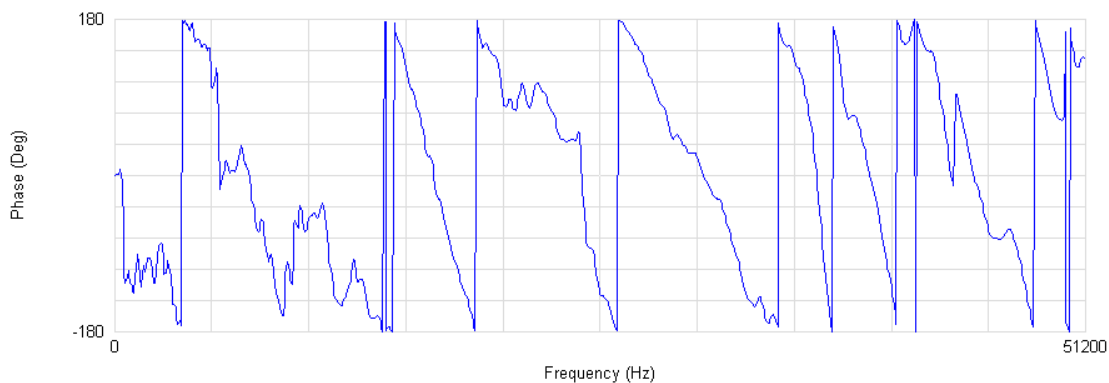
Fig. 2.10. Typical wrapped phase spectrum
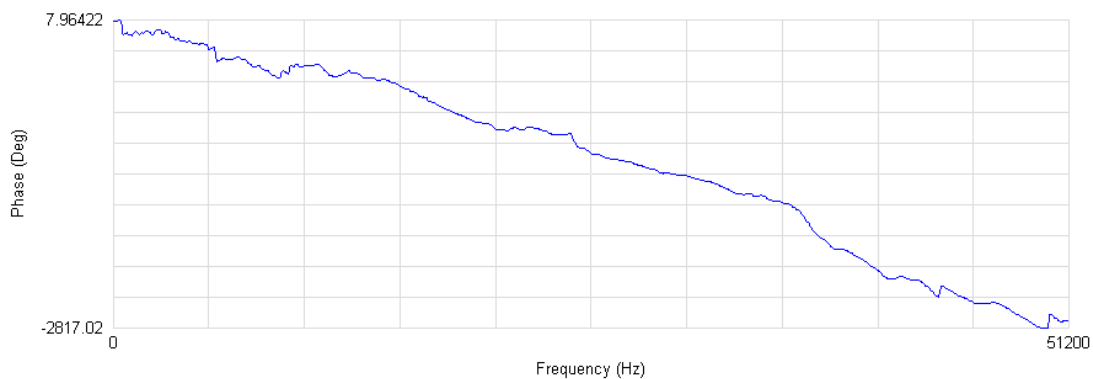
Fig. 2.11. Typical unwrapped phase spectrum

The experimental dispersion curve is then created by repeating these calculations for each frequency and associated phase value.

However, not every phase angle and associated frequency can be assumed to represent good data and an accurate interpretation of the phase spectrum is needed. The interpretation procedure applied to the phase spectrum is called interactive masking. Interactive masking is used to remove the low quality phase data from the phase spectrum. Regions that have undulating phase angles, phase angles with backwards saw tooth patterns, and/or messy phase angles are removed from the phase spectrum. Also, data in the region of the near field and regions that violate the criterion of receiver geometry should be removed (Joh 1996). Fig. 2.12 shows a masked and unmasked phase spectrum and the resulting dispersion curves. It can be seen that when the data is completely unmasked, it is difficult to determine the unwrapped phase spectrum and the dispersion curve gives erroneous data.

The next step in the SASW analysis is the creation of a theoretical dispersion curve. A theoretical dispersion curve is a calculated phase velocity plot created based on an assumed stiffness profile.

(a) Unmasked phase spectrum

Fig. 2.12. Masking data for the creation of experimental dispersion curves

(b) Dispersion curve using unmasked data
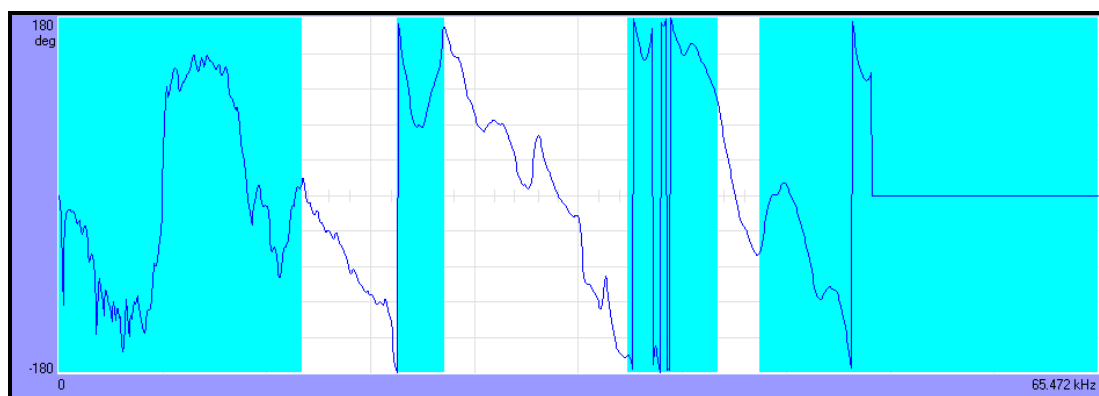
(c) Masked phase spectrum

(d) Dispersion curve using masked data

Fig. 2.12. (continued)

In this method, a dynamic stiffness matrix quantifies the relationship between the stresses and displacements at the interface between media in a layered system as a result of an arbitrary dynamic load imparted upon that system. Two solutions are possible. The first assumes plane surface waves and only includes the first mode of propagation of those waves. This solution is called the 2-D solution. The 2-D solution provides good results for stiffness profiles of increasing gradual stiffness. The 3-D solution, which represents the superposition of body and surface waves moving in all directions, is considered optimum. Due to the reflection and refraction of multiple waves at the interface of these media in a layered system, the propagation of more than one wave group through the entire body is observed. In the 3-D solution, the superposition of several modes of different types of waves is realized, and systems of various layering and stiffness gradations can be solved (Joh 1996).

The special case of layered systems with large stiffness contrasts and particularly those in which stiffness decreases with depth is of particular interest in the 3-D solution. In such a system, the roots of the stiffness matrix are complex to the point at which the wavelengths being determined significantly exceed the thickness of the upper, stiffer, layers. At this point, shear wave velocities determined by the solution are those of the lower, less stiff, layer. The complex roots are exceedingly difficult to extract and interpret, and therefore, alternate methods which solve only for the real part of separate waveforms are performed (Stokoe et al. 1994). Interactive masking of such a system using the impulse response filtration technique is one method that can solve for the correct stiffness profile of the system. In this approach, it becomes imperative to distinguish between the multiple wave groups propagating to accurately unwrap the

phase spectrum. The detection of these wave groups can be performed using the Gabor

spectrogram (Dziewonski et al. 1969), which presents the response of a system as a linear

combination of time-and-frequency-shifted Gaussian functions (Fig. 2.13) (Joh 1996).

In order to determine the depth and stiffness profile of a layered system, the

matching of the theoretical dispersion curve and experimental dispersion curve must be

completed. An assumption of the stiffness profile is made and a theoretical dispersion

curve is plotted using the dynamic stiffness method. The process of manually changing

the assumed profile until the theoretical and experimental dispersion curves match is

called forward modeling.

Another method used to calculate the stiffness profile is called inversion.

Inversion analysis is an automated forward modeling procedure that uses a goodness of

fit measurement to determine whether an assumed stiffness profile creates a theoretical

dispersion curve close enough to the experimental dispersion curve. The inversion

analysis engine used for this study is one using a maximum likelihood approach proposed

by Tarantola (1987) and implemented in the WinSASW application written by Dr. Sung-

Ho Joh. This inversion analysis uses a root mean square error goodness of fit to

determine whether an assumed stiffness profile corresponds to the actual profile.
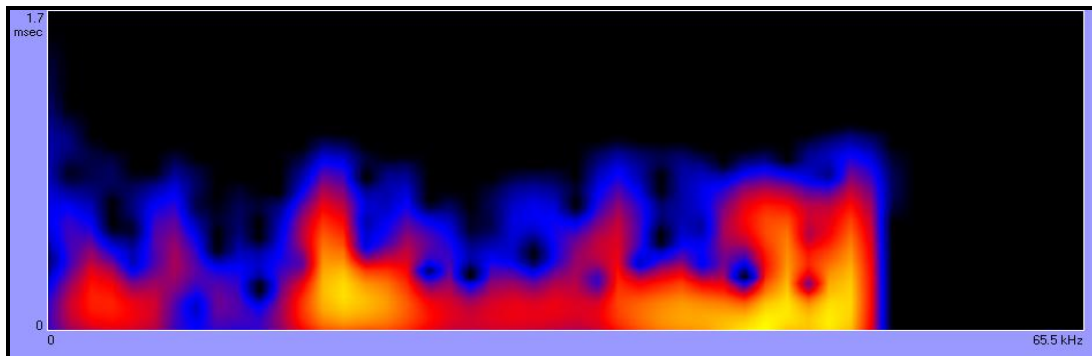
Fig. 2.13. Gabor spectrogram

At the point where the theoretical dispersion curve created using either a forward modeling or inversion analysis and the experimental dispersion curve match, the assumed profile is deemed to be correct and the analysis is concluded.

The Free-Free Resonant Column Method

This section discusses the history of the FFRC method along with previous research findings. The experimental and analysis procedure for the method is also outlined.

<u>Background</u>

The FFRC method is one of the oldest and most frequently used of the stress wave propagation methods. Originally standardized by ASTM in 1947, the method is now designated as ASTM C215, Standard Test Method for Fundamental Transverse, Longitudinal, and Torsional Resonant Frequencies of Concrete Specimens (ASTM 2002)

The majority of its uses apply directly to the determination of dynamic Young's and shear moduli of concrete specimens. It has been used to quantify, through units of dynamic moduli or damping ratio, damage due to freeze thaw (Seely 2005), monotomic and cyclic damage (Gheorghiu et al. 2005) incurred upon concrete specimens. Its uses typically coincide with the correlation of static to dynamic modulus in concrete specimens, however, and to this extent, it has been used in a variety of studies (Jones 1962; Whitehurst 1966; Neville 1996; Nagy 1997; Boone 2005; Seely 2005).

Experimental Procedure and Analysis

The testing protocol for the FFRC method is explained in detail in ASTM C215 (2002) and involves an impact source, receiver (accelerometer), and digital signal analyzer. The receiver positioning and impact point depends on the desired mode of vibration. Longitudinal and torsional vibrations coincide with Young's modulus and shear modulus of elasticity, respectively. After the receivers are positioned to measure the desired mode of vibration, an impact is made at the corresponding impact point and the response time history is recorded with the digital signal analyzer. The time history is then transformed into the frequency domain using an FFT and the first mode fundamental frequency is determined similarly to that of the IE method.

The unconstrained longitudinal frequency measured during the FFRC testing is associated with the propagation of normal stress which is related to the unconstrained longitudinal wave, or rod wave, velocity, V_c. The rod wave is related to the dynamic Young's modulus of elasticity. The torsional frequency measured is associated with the propagation of shear stress which is related to the shear wave, V_s. Equations exist to relate the rod wave and shear wave to the Young's modulus and shear modulus of elasticity:

$$V_c = 2 f_l L C_l \qquad \text{2.23)}$$

$$E_d = \rho V_c^2 \qquad \text{(2.24)}$$

$$V_s = 2 f_t L C_t \qquad \text{(2.25)}$$

$$G_d = \rho V_S^2 \qquad \text{(2.26)}$$

where: V_c = rod wave velocity

f_l = 1st mode unconstrained longitudinal frequency of the specimen

L = length of the specimen

C_l = correction factor that depends on the ratio of the length of the

specimen to the diameter of the specimen

E_d = dynamic Young's modulus

ρ = mass density of material

f_t = 1st mode unconstrained torsional frequency of the specimen

C_t = correction factor that depends on the ratio of the length and shape

factor of the specimen (1 for a circular cylinder) to the cross sectional area

of the specimen

Stress Wave Propagation Combination Methods

Although SASW, IE, and FFRC testing appear to be the most commonly used stress wave propagation methods for nondestructive testing of concrete, research focusing their combined use has rarely been performed. Kim et al. (2006) performed a feasibility study and associated experimental investigation on combining these methods. Although measurements from the SASW and IE methods were combined during the analysis, the testing methods were performed independently. A simplified SASW analysis was performed that did not include any forward modeling or inversion procedures. Rayleigh wave velocities were calculated during this simplified SASW analysis. The FFRC method was not used and Poisson's ratios were assumed. An average P-wave velocity was then calculated from the Rayleigh wave velocities and the assumed Poisson's ratio using Eq. (2.27). This average P-wave velocity was used in the IE analysis.

$$V_p = \frac{1+v}{0.87+1.12v} \sqrt{\frac{2(1-v)}{(1-2v)}} V_R \qquad (2.27)$$

where: V_p = average compression wave velocity

V_R = average Rayleigh wave velocity

v = assumed Poisson's ratio

It should be noted that Eq. (2.27) only holds true for Poisson's ratios of approximately 0.15 to 0.30. Although this is adequate for concrete, a more precise formula should be used. The calculated error as a result of using an assumed Poisson's ratio is at most 5%. Using the IE method and this average compression wave velocity, the depth of a single layered slab can be found along with any internal flaws. For a single layer system, this approach seems to work well. Kim was able to verify the depth to known flaws in a concrete slab as well as the total depth of the slab.

The researchers reasoning for using the SASW method to determine the average compression wave velocity instead of direct methods of measuring the wave velocity (Sansalone 1997) was that the P-wave velocity found using the direct measurement method was only representative of the concrete. Also noted was that not all slab systems have two boundaries from which a true P-wave measurement could be made, and in these cases, the depth of the slab was unknown. These are all valid arguments. However, the use of the SASW method to take an average measurement over the entire cross section is only valid if the system is composed of a single modulus concrete that is sound throughout the cross section. In the event that there is poor concrete, or a multilayered system, the averaging of P-wave velocities over the entire cross section causes erroneous data during the IE method analysis.

The SASW method should be used to determine the depth and layering of the profile. This should include some type of forward modeling or inversion analysis that can differentiate between layers of material with varying stiffness. With a complete layering system formulated, the true P-wave and shear wave velocities of each layer can be calculated. From this data, the IE method can be used to verify the depths of each layer and to detect any flaws.

Also, because the two methods are so similar in experimental setup, the two tests can be run in parallel simply by using another channel of the digital signal analyzer. In this case, three receivers would be setup, one for the IE measurement and two for the SASW measurement. In theory, the IE data could be taken from the waveforms created using the impact from the SASW method, or vice versa, but due to the specific waveforms measured for each test, individual receivers for the two methods would provide better-quality data. The same impact source can be used for both tests and data can be collected simultaneously.

A newly proposed method called the combined stress wave propagation (CSWP) method takes into account these principles and is further described in Chapter 3 of this report.

Damage Quantification

Several methods have been developed to model the damage in concrete structures. The majority of these models use energy-related damage indicators to quantitatively assess the damage in such structures (Rao et al. 1998; Garstka et al. 1993; Sadeghi et al. 1993; Park and Ang 1985). Also, Hsu (1981) has developed relationships for the

calculation of fatigue of plain concrete to incorporate indicators such as stress versus number of cycles, ratio of minimum stress to maximum stress, and rate of loading. Other models have used other various indicators such as splitting tensile strength (Gettu et al. 1996), stress-strain relationships (Gao and Hsu 1998; Bahn and Hsu 1998), and strain-cycle relationships (Alliche and Francois 1989).

As cycling and fatigue occurs in concrete, the primary reason for a decrease in structural related properties is the continuous microcrack growth. Thus, research interest to investigate procedures to measure the growth of these cracks has been conducted (Suaris and Fernando 1987; Suaris et al. 1990; Nogueria and Willam 2001). All of these tests have incorporated nondestructive testing (NDT) techniques to quantify crack growth as a function of loading cycles. Measurements of pulse velocity, acoustic emission, and ultrasonic wave attenuation are methods that have been used to determine the growth of microcracks. All of these methods use similar techniques to excite the specimens and measure the elastic wave characteristics of the material during and after cyclic loadings. The free-free resonant column (FFRC) method has been used to quantify damage in terms of the fundamental longitudinal, transverse, and torsional frequencies as well as damping (Gheorghiu et al. 2005). The results from all of the NDT research indicate that the measurement of elastic wave properties is a good indicator of damage in concrete. A more recent study (Shokouhi 2008) indicates that not only are the elastic properties of the material dependent on the growth of microcracks, but also on the closing of microcracks. Shokouhi has shown in a feasibility study that surface wave velocities propagating parallel to the direction of loading demonstrate a distinct stress sensitive behavior. During this study, surface wave velocities were measured while concrete

specimens were uniaxially loaded to 35% and 80% of the ultimate compressive strength. Her results indicate that as load and inherent stresses increase, microcracks in the specimens close and the surface wave velocities increase.

There is also an anisotropic behavior of elastic waves in loaded concrete specimens that depends on the direction of loading relative to the direction of wave propagation (Shokouhi 2008). Thus, the presence of microcracks forming in the same direction of loading can be measured by determining the changes in stress wave propagation in that direction.

Studies that have used the FFRC method to determine the decrease in fundamental longitudinal, transverse, and torsional frequencies have shown that for a specific concrete mix, these natural frequencies decrease (Gheorghiu et al. 2005). However, a trend to show their amount of decrease has not been determined. It is the goal of this study to show that for a variety of concrete specimens varying in strength a general trend exists for all concrete specimens and a specific trend exists for defined concrete strengths with regards to the decrease in first mode longitudinal frequency and increase in damping ratio. This information will provide engineers a new tool to continue the development of the understanding of concrete behavior in fatigue.

A Comparison of Prestress Losses for
Prestressed High Performance
Concrete Bridge Girders

High performance concrete (HPC) is a type of concrete that provides superior physical properties such as increased strength for specific applications like prestressed concrete bridge girders. A specific type of HPC studied during this research is self-

consolidating concrete (SCC). SCC is discussed in detail in Chapter 4 of this document.

SCC utilizes highly refined mix proportions and mixing sequences to produce a concrete

that consolidates completely without the need for vibrating, greatly reducing labor costs.

This allows the concrete to flow under its own weight into sections of highly reinforced

formwork, making it perfect for prestressed bridge girders. This type of concrete has also

been shown to increase in strength very quickly within its first few days of curing.

Because compressive strengths increase so quickly, girders can be removed from the

formwork and prestressing strands can be released in as little as one day. Finally, bridges

that incorporate the use of these girders can be fabricated with longer spans, fewer

girders, and more clearance. Thus, using high performance SCC (HPSCC), prestressed

concrete bridges can be produced for a smaller cost than those using conventional normal

strength concrete. These advantages of HPSCC have been utilized by engineers in Utah

for the use of prestressed concrete bridge girders.

 Although the benefits of using HPC SCC are somewhat apparent, few bridge

girders are in place that utilize the material. Also, there are no long-term measurements

to validate the calculation of prestress losses for this specific type of concrete.

 The comparison of measured and predicted prestress losses in HPC prestressed

bridge girders is highly documented in literature. Kukay et al. (2007) investigated a

comparison of time dependent prestress losses in a two-span, prestressed concrete bridge.

The four bridge girders studied in this investigation were made of HPSCC and were

instrumented with vibrating wire strain gauges with integral thermistors. The study

compared values of prestress loss calculated from measured strain to predictive values

found using the NCHRP method (NCHRP 18-07). The study found that there was a

relatively low percentage (11.5% of the jacking stress) of total prestress loss due to the actual concrete strength that was significantly higher than was required by design. Using the NCHRP predicted values, the study also found that when actual concrete strengths were used the predicted values of prestress losses corresponded closely with the measured values up through deck casting. After deck casting, the predicted values of total loss were found to be un-conservative when the actual compressive strengths were used in the calculations.

Barr et al. (2007) instrumented and monitored five precast, prestress girders made with HPC. These girders were monitored for prestress losses for three years after the time of casting. The observed values of prestress losses were compared with values calculated using the 2004 AASHTO LRFD Specifications and the methods based on the results of NCHRP 18-07 (Tadros et al. 2003). The study found that by using a calibrated modulus of elasticity, total losses calculated using the NCHRP method were within 10% of the measured total losses. However, this calibrated modulus resulted in the AASHTO calculated values being 30% higher than the total measured losses. The study found that, on average, the observed elastic shortening losses were found to be 21% higher than those calculated using AASHTO and 11% lower than those calculated using the NCHRP method. The difference between the measured and predicted losses was reduced to within 3% difference when the calibrated modulus was used.

Kowalsky et al. (2001) instrumented and measured prestress losses in HPC bridge girders in North Carolina. Kowalsky et al. found shrinkage losses were a small component to overall prestress losses and that the elastic shortening and creep losses were the major contributors. These larger than expected losses from elastic shortening

and creep were attributed to an actual modulus of elasticity that was lower than predicted. The total prestress losses ranged from 12.9% to 19.1% of the initial jacking stress.

Yang and Myers (2005) instrumented four HPC prestressed bridge girders in Missouri with a total of 16 internal thermocouples, 64 VWSGs, and 14 internal bonded electrical resistance gauges (ERSG). Yang and Myers incorporated eight commonly used loss estimate models for total prestress losses, including the AASHTO, Prestressed Concrete Institute (PCI), and NCHRP methods. They measured total average losses of 20.7% of the initial jacking stress with elastic shortening accounting for the largest portion of the total loss. Also, they found that for prestress precast HPC girders, the PCI handbook method, the method recommended by Gross (1999), and the NCHRP method to be optimal for prestress losses estimation in the design stage.

Ahlborn et al. (1995) tested two full-size composite I-girders fabricated with HPC. Two different mix designs were used for these girders, which spanned 133 feet. Prestress losses predicted by incorporating measured material properties into the PCI general time step approach were 5 to 10 percent larger than measured in the instrumented girders.

Roller et al. (1995) fabricated and tested several prestressed high strength concrete bulb-tee girders. They found that the AASHTO LRFD 1989 Specifications provisions for calculating creep and shrinkage prestress losses may be overly conservative for high-strength concrete. In their study, measured prestress losses were significantly less than the total long-term prestress losses predicted using the provisions in the AASHTO LRFD 1989 Specifications. They also found that measured creep and shrinkage deformations of cylinders representing the concrete in the instrumented girders

were consistent with the finding regarding the measured prestress loss. Their study

concluded that high strength bridge girders could be expected to perform adequately over

the long-term when designed and fabricated in accordance with AASHTO LRFD 1989

Specifications. However, the measured prestress losses in one of the girders

instrumented was 50% less than the expected value indicating that the AASHTO LRFD

1989 Specifications used were grossly conservative.

Further literature regarding prestress losses in prestressed HPC bridge girders can

be found in Cole (2000), Tadros et al. (2003), Stallings et al. (2003), and Gilbertson and

Ahlborn (2004).

Comparison Between Static and
Dynamic Young's Modulus

In solid mechanics, Young's modulus, E, is a measure of stiffness, and is defined

as the ratio of the rate of change in stress with strain. Young's modulus can be

experimentally determined, either in tension or compression, from the slope of a stress-

strain curve measured during uniaxial loading. Young's modulus is named for the 18th

Century British Scientist Thomas Young. However, Leonhard Euler developed the

concept in 1727 and Giordano Riccati predated Young's work by 25 years with the first

experiments that used the concept of Young's modulus in its current form in 1782

(Wikipedia 2008). When applying these concepts to the testing of concrete, the modulus

described above is known as the static Young's modulus, E_s, and methods to determine

its value are specified in ASTM C 469 (2002), the Standard Test Method for Static

Modulus of Elasticity and Poisson's Ratio of Concrete in Compression.

In addition to research regarding the static Young's modulus in which a

significant stress is required, research has been performed to determine the value at small stress and strains. In 1877, Lord Rayleigh reported a "mathematical relationship existing between the velocity of sound through a specimen and its resonant frequency and the relationship of these two to the modulus of elasticity of the material." The relationship between the resonant frequency and what is termed the dynamic modulus of elasticity was thus found (Rayleigh 1976). In this case, the resonant frequency referred to is the longitudinal resonant frequency.

In 1938, T.C. Powers laid the groundwork for the dynamic testing of concrete samples. He was able to determine the resonant frequency of concrete samples, usually 2 in. x 2 in. x 9 ½ in., by supporting the sample at its nodal points (1/3 and 2/3 times the length of the specimen), striking it with a hammer, and matching the musical tone that was produced with a calibrated tone source. Powers used a set of Deagan orchestra bells and a homemade sonometer for the tone source. He found that the error likely to occur using the bells was on the order of approximately 3% while the error using the sonometer was much less (Whitehurst 1966). In 1939, Hornibrook refined the method by using electronic equipment to measure the resonance. Other early investigations on the development of this method included those by Obert and Duvall (1941), and by Stanton (1944). In these tests, a sonometer was used to measure the resonant frequencies of the tested specimens. These processes have evolved into the method that is designated as standard ASTM C 215, the Standard Test Method for Fundamental Transverse, Longitudinal, and Torsional Resonant Frequencies of Concrete Specimens.

In the case of the dynamic Young's modulus, the measured modulus is almost purely elastic. This is due to the absence of a significant applied stress and as a result, the

lack of micro cracking induced creep. In this case, a specimen could be loaded and unloaded without significantly affecting the linear elastic properties of the material. Because the dynamic modulus refers to almost purely elastic response, it has typically been considered equal to the initial tangent modulus determined in the static test (Neville 1996; Mehta and Monteiro 2006).

The difference between static and dynamic Young's modulus is of great importance to engineers for several factors. The static Young's modulus is typically assumed to quantify the stiffness of a material during the design phase of a concrete structure. The American Concrete Institute (ACI), Prestress Concrete Institute (PCI), and American Associate of State Highway and Transportation Officials (AASHTO) all suggest methods to calculate the static Young's modulus. Using the equations suggested by each, an engineer could determine an appropriate value of Young's modulus to use in equations to determine deflection, ductility, and other important properties of a designed structure. The dynamic Young's modulus, however, is a measured value. There are currently no accepted design equations from which the dynamic Young's modulus can be calculated. Also, because it can be measured using nondestructive techniques, it is much easier to determine its value on an in-place structure. Due to these differences, there is a growing need for the capability to calculate one moduli from the other.

There has long been a debate concerning the magnitude of the ratio between the static and the dynamic Young's modulus of elasticity and the difference in material behavior required to cause this ratio. Most literature defines the static Young's modulus of elasticity of concrete as a chord modulus calculated based on an initial strain (typically 0.0005) and a higher strain typically determined as the ultimate compressive stress

(typically 40% of f'$_c$). These researchers also agree that the dynamic modulus should be considered the initial tangent modulus of a concrete stress-strain curve (Neville 1996; Mesbah et al. 2002; Mehta and Monteiro 2006). Because of the nonlinearity of the stress-strain curve typically measured on concrete specimens, the ratio of static to dynamic Young's modulus is always less than one. Studies have also shown that as the strength of the concrete increases, the stress strain curve becomes more nearly linear. As this happens, the value of the static modulus increases, and the ratio between the dynamic modulus and the static modulus approaches unity (Neville 1996). Although this ratio depends entirely on the specific concrete being measured, studies have been performed in an attempt to quantify the relationship. Several equations have been suggested.

Nagy (1997) obtained moduli measurements on two different concrete mixes and used the results to develop a relationship between the static and dynamic Young's moduli. The relationship is based on the damping ratio of the concrete specimen and is listed as Eq. (7.1).

$$E_s = \frac{E_d}{1 + \eta^\alpha} \tag{7.1}$$

where: E_d = dynamic Young's modulus

η = damping ratio

α = an empirical factor

In his study, Nagy found α to be approximately equal to 0.35. He also found that the ratio between static and dynamic moduli to be approximately 0.80 after a few days of curing. This value is widely accepted as the approximate ratio between static and dynamic Young's moduli and has been reported as 0.83 by Lydon and Balendran (1986).

Nagy found his results to be independent of the w/c ratio or cement type. Seely (2005) also studied three concrete mixes and found α to be approximately equal to 0.359, thus validating Nagy's research.

Mesbah et al. (2002) conducted a study on three different high performance concrete mixes. The researchers also concluded that the dynamic modulus is considered to be approximately equal to the initial tangent modulus obtained during a static test. Because the literature reviewed in their research consisted of measurements performed on normal weight concrete, they proposed a formula to convert dynamic to static Young's moduli for high performance concrete:

$$E_s = 9 \times 10^{-11} \left(65E_d + 1600\right)^{3.2} \tag{7.2}$$

where moduli are in units of GPa. They found that with this formula they were able to accurately predict either the static Young's modulus from the dynamic Young's modulus or vice versa for the three tested mixes. However, they found this formula to be significantly dependent on age of the concrete and it was only held true for the mixes tested.

Han and Kim (2004) performed a study on four concrete mixes cured at various temperatures. The four concrete mixes were composed of two types of cements with two w/c ratios. The four mix designs had a range in compressive strengths based on the curing temperature from 3800 psi to 6500 psi at 28 days. They found that the slope of the initial chord elastic modulus from values of 10×10^{-6} to 50×10^{-6} was more closely related to the dynamic Young's modulus than the initial tangent modulus. They proposed a formula based on several assumptions (Eq. (7.3)). The assumption that as the strength of the concrete increases, the dynamic elastic modulus increases, and the stress-strain

curve below 40% of the ultimate compressive strength becomes more linear was made. This led to the assumption that as the linearity of the stress-strain curve increases, the difference between the static and dynamic moduli decreases. Finally, they assumed that when the static modulus is zero, the dynamic modulus is zero.

$$E_s = E_d\left(1 - ae^{-bE_d}\right) \tag{7.3}$$

where a and b are constants used to fit the calculated data to the measured data and moduli are in units of GPa. They found a to range from 0.492 to 1.021 and b to range from 0.0170 to 0.0431. They concluded that since the experimental data had dissimilar ranges at different ages, the comparison between dynamic and static moduli could not be accurately quantified as a function of age. They also concluded that the relationship between dynamic Young's modulus and compressive strength was not significantly affected by cement type or age. In addition, the curing temperature did not have a large influence on the relationship between the initial chord modulus and the dynamic Young's modulus, and cement types did not significantly affect the relationship between static and dynamic Young's moduli.

Although the research comparing the static and dynamic moduli appears to be various, most literature agrees that the ratio between the static and dynamic Young's modulus is approximately 0.83, and that this difference is mostly dependent on strength and age (Lydon and Balendran 1986; Neville 1996; Mesbah et al. 2002; Seely 2005; Mehta and Monteiro 2006). Results from other studies also showed that the static Young's modulus could be directly calculated using dynamic Young's modulus and damping ratio measurements (Nagy 1997; Seely 2005). Finally, a majority of the reviewed literature agrees that the dynamic Young's modulus is approximately equal to

the initial tangent modulus measured using static tests (Neville 1996; Mesbah et al. 2002;

Mehta and Monteiro 2006).

CHAPTER 3

NONDESTRUCTIVE ANALYSIS OF A CONCRETE TUNNEL MODEL USING A

PROPOSED COMBINED STRESS WAVE PROPAGATION METHOD

Abstract

This paper summarizes the measured dynamic properties of a concrete tunnel

model using a newly proposed combined stress wave propagation (CSWP) method. The

spectral analysis of surface waves (SASW) and impact echo (IE) methods were used in

combination to determine the in-place dynamic properties of the tunnel lining and to

locate embedded voids. Simultaneously, the free-free resonant column (FFRC) method

was used independently to determine the dynamic properties of the materials used to

make the concrete tunnel model. Finally, a direct P-wave (DPW) measurement was used

to compare and verify measurements recorded using the CSWP method. Results indicate

that the combination of the SASW and IE methods, along with FFRC measurements,

provides a more efficient procedure that results in the determination of the P-wave and

shear wave velocities, depths of layers, and locations of embedded voids without the need

to make assumptions of any material properties. Thus, more physical properties can be

found using this proposed procedure than by using the techniques independently, and the

procedure is more efficient than performing each task separately.

Introduction

The spectral analysis of surface waves (SASW), impact echo (IE), and free-free

resonant column (FFRC) methods are the most commonly used stress wave propagation

methods for nondestructive testing of concrete. The techniques, analysis procedures, and

applications for SASW, IE, and FFRC can be found in many published papers. Each of their test results provides a variety of quantifiable data that can help describe the in-place properties of a concrete structure. However, by using a procedure for combining the SASW and IE methods, along with the FFRC test on laboratory specimens, all of the structural properties can be found in a more efficient manner without the need to make any material assumptions.

While SASW testing has predominantly been used in the field of geotechnical site investigation, the method has also been applied to concrete. The SASW method has been used to determine velocity profiles of portland cement concrete (PCC) slabs (Bay and Stokoe 1990; 1992), multi-layer slabs with finite thickness using finite element modeling (Cho 2005), high-performance concrete (Cho 2003), concrete tunnel linings (Kang et al. 2006), damaged concrete beams (Kalinski et al. 1994), and a mass concrete placement (Boone 2005) among others.

The IE method has been used to detect flaws in concrete such as honeycombing, voids, cracks, and shallow delaminations in plate, circular, square, rectangular bar, and hollow cylinder structural geometries (Sansalone 1997). The procedure has also been used to determine crack widths in concrete elements (Cheng and Sansalone 1995), determine interfacial bond quality (Lin and Sansalone 1996), quantify depth of surface-opening cracks (Sansalone et al. 1998), determine velocity-strength relationships (Lee et al. 2003), and evaluate early-age concrete strength (Pessiki and Johnson 1996) among many other studies.

The IE method relies on *a priori* knowledge of either the depth of a cross section or P-wave velocity of the in-place concrete in order to obtain the P-wave velocity or

depth, respectively. Thus, the direct P-wave (DPW) method was developed to make the IE method effective on concrete elements of which only one surface was accessible. The DPW method is typically used to determine the P-wave velocity of concrete elements or pavements. Once the P-wave velocity is known, the IE method can be used to determine depths of layers and / or identify internal flaws (Sansalone et al. 1997).

The final nondestructive method used in this study was the FFRC method. It is one of the oldest and most frequently utilized of the stress wave propagation methods. Originally standardized by ASTM in 1947, the method is now designated as ASTM C215, Standard Test Method for Fundamental Transverse, Longitudinal, and Torsional Resonant Frequencies of Concrete Specimens. The majority of its uses apply directly to the determination of dynamic Young's and shear moduli of concrete specimens. It has been used to quantify, through units of dynamic moduli or damping ratios, damage due to freeze thaw (Seely 2005), monotonic and cyclic damage (Gheorghiu 2005) incurred upon concrete specimens.

Although SASW, IE, and FFRC testing appear to be the most commonly used stress wave propagation methods for nondestructive testing of concrete, research regarding their combined use has rarely been performed. Kim et al. (2006) performed a feasibility study and associated experimental investigation on combining these methods. Although measurements from the SASW and IE methods were combined during the analysis, the testing methods were performed independently. A simplified SASW analysis was performed that did not include any forward modeling or inversion procedures. Rayleigh wave velocities were calculated during this simplified SASW analysis. The FFRC method was not used and Poisson's ratios were assumed. An

average P-wave velocity was then calculated from the Rayleigh wave velocities and the assumed Poisson's ratio. This average P-wave velocity was used in the IE analysis.

This study proposes a new combined stress wave propagation (CSWP) method that is a much more efficient technique that combines not only the analysis portion of the procedure, but also the SASW and IE measurements. A complete SASW analysis is performed that incorporates an inversion process that can determine the velocity profile of multi-layered systems. Also, by incorporating dynamic properties measured using the FFRC method, no assumptions are required for the final analysis.

Concrete Tunnel Model

A three layer concrete slab was constructed in Logan, Utah as a model of a concrete tunnel lining. The purpose of the slab was to replicate the stiffness profile that might be expected in a typical concrete tunnel structure. The top layer was intended to model the concrete in a tunnel structure and was made with a standard 4,000 psi mix. The intermediate layer was intended to model a grout or soil layer and thus was only designed to be approximately 300 psi. The bottom and final layer was intended to model a bedrock type material and was the strongest of the three layers having a 28 day compressive strength of approximately 10,000 psi. The bedrock was idealized as there were no joints or other known flaws present in the cast concrete. Proportions for all three mix designs are presented in Table 3.1. Also, a three layer cylinder was made in order to replicate the waveform that was created in the three layer slab (Fig. 3.2).

The slab was approximately 16 ft. x 6.5 ft. x 2 ft and is shown in Fig. 3.1(a). It contained embedded voids placed between the top and middle layers (Fig. 3.1(b)). The

voids were approximately 1 in. thick, and were made of bubble rap material that provided

low specific acoustical impedance in relation to the surrounding materials. This

condition is similar to the behavior of a true void in a tunnel lining.

Table 3.1. Mix Designs for Three Layer Slab

	Top Layer	Middle Layer	Bottom Layer
Sand (lb.)	1541	3400	1351
Cement (lb.)	452	301	545
Aggregate (lb.)	1750	0	1582
Water (lb.)	245	220	250
Fly Ash (lb.)	120	75	136
Air (%)	5	5	5
w/c	0.54	0.73	0.46
Total Weight (lb.)	4108	3996	3864

(a) Three layer concrete slab
Fig. 3.1. Concrete tunnel lining model
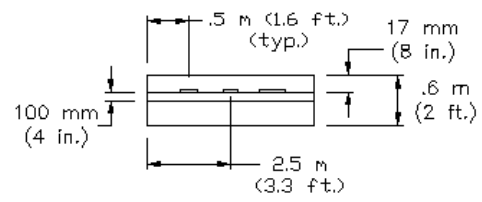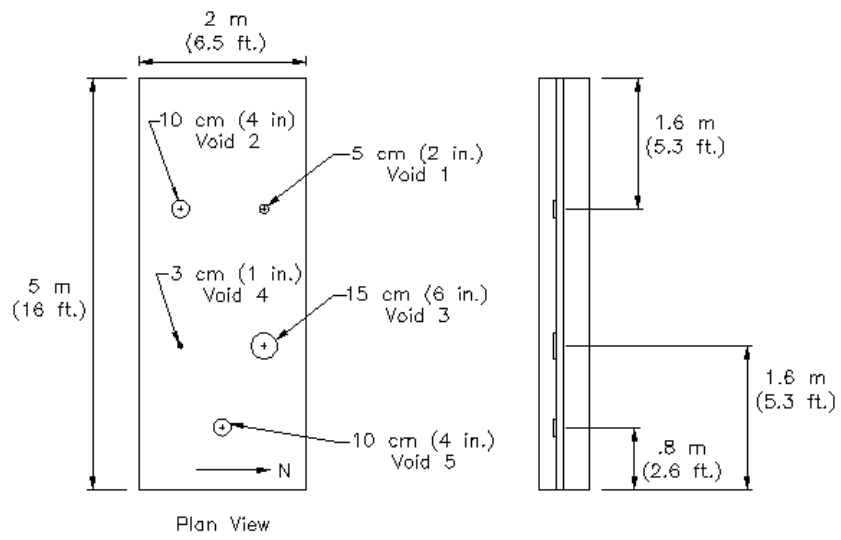
(b) Embedded void plan view
Fig. 3.1. (continued)

Fig. 3.2. Three layer cylinder

**Combined Stress Wave Propagation
Method**

A new procedure is proposed in this study that combines the SASW and IE

methods. It was used on the concrete tunnel model to determine the stiffness and

layering of the system and identify the locations of embedded voids. Thus, the

methodology of combining each nondestructive test into one procedure to determine the

structural properties of the lining and locate any flaws is proposed.

The SASW and IE methods were used jointly to measure the compression wave

velocity (P-wave), shear wave velocity, and depth of each concrete layer for the three

layer system. The DPW measurement procedure (Sansalone et al. 1997) was also used to

compare and validate the P-wave velocities found using the SASW and IE methods. The

FFRC method was used to determine the dynamic properties of the materials in the lab in

order to avoid assumptions during the analysis portion of the procedure. These values

collectively provided all of the dynamic moduli properties of the in-place concrete.

Also, once the P-wave velocities and depths were determined, embedded voids, located

between the top and middle layers of the slab, were identified and the depth to each void

was measured.

Free-Free Resonant Column Results

Material specimens were made from the concrete mix proportions (Table 3.1)

used to place the three layers of the concrete tunnel model. The individual material

specimens were placed in 4 in. diameter x 8 in. long cylinders. FFRC tests were

performed in parallel with static Young's modulus and compression strength tests on

each specimen. Also, dynamic values calculated from the FFRC analysis were used

during the SASW analysis to avoid making material property assumptions.

FFRC measurements yielded data for the longitudinal and torsional first modal

frequencies. From these values, the unconstrained compression wave (rod wave) and

shear wave velocities were calculated, respectively, using Eq. (3.1). The dynamic

Young's moduli, E_d, and dynamic shear moduli, G_d, were then calculated using these

respective wave velocities. Poisson's ratios were then calculated from these moduli.

Finally, the P-wave velocities were calculated using Eq. (3.2) (Timoshenko and Goodier

1970). The half power bandwidth was also measured from each first mode longitudinal

frequency peak and the damping ratio of each material was calculated. The 28 day values

of wave velocity, dynamic Young's Modulus, and damping for each material tested are

listed in Table 3.2.

$$V = f\lambda \tag{3.1}$$

$$V_p = \sqrt{\frac{M_d}{\rho}} = \sqrt{\frac{E_d(1-v)}{\rho(1+v)(1-2v)}} = \sqrt{\frac{2G_d(1-v)}{\rho(1-2v)}} \tag{3.2}$$

where: V = velocity at which a wave travels through a material

f = associated wave frequency

λ = associated wavelength

V_p = constrained compression wave velocity of the material

M_d = dynamic unconstrained modulus of elasticity

ρ = mass density of the material

E_d = dynamic Young's modulus of the material

v = poisson's ratio of the material.

Field Testing

SASW arrays were placed on the top and side surfaces of the slab. In this case, an array refers to a single impact point with multiple receiver spacings. There were 5 arrays placed on the top surface of the slab with 7 impact points and 3 arrays placed on the side surface of the slab with 3 impact points (Fig. 3.3). The purpose of the side surface arrays was to make both direct shear wave and DPW velocity measurements of each individual material. Piezoelectric accelerometers were used as receivers and were attached to the plates using small magnets. The excitation sources used for the CSWP method were small steel spheres ranging in size from 5/16 in. to 7/16 in., an instrumented hammer capable of producing frequencies ranging from 10 to 25 kHz, and a 2 lb. ball peen hammer.

During the SASW testing, receivers were also positioned close to the source to make IE measurements. Thus, at each source location for the SASW tests, an IE measurement was also performed. IE measurements were also performed directly above the location of the embedded voids. IE receivers were set up 2 in. from the sources. DPW measurements were made on the side surface arrays of each material. For this method, an impact was produced using a 5/16 in. steel sphere. Accelerometers were set at 6 in. and 12 in. from the impact source and were used as receivers for all testing.

Table 3.2. Dynamic Properties Calculated from Measured Data Using the FFRC Method

Layer	V_{rod} (ft/sec)	V_s (ft/sec)	V_p (ft/sec)	ν	Damping Ratio, ζ
Top	11800	7680	12300	0.18	0.017
Middle	7700	5020	8020	0.18	0.020
Bottom	13500	9030	14700	0.20	0.010
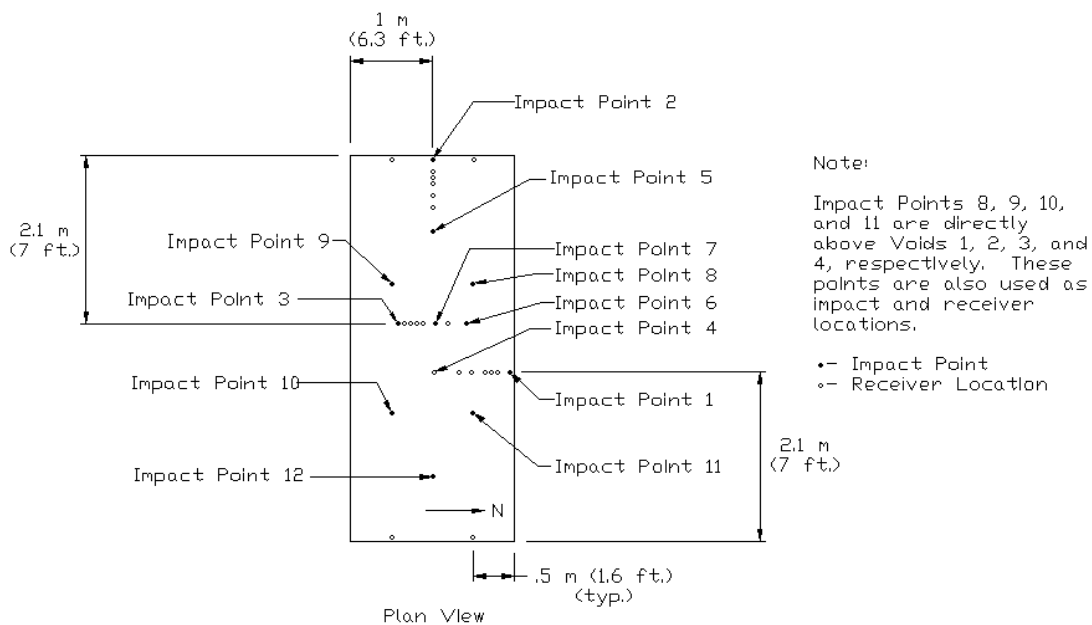
(a) CSWP array and impact locations
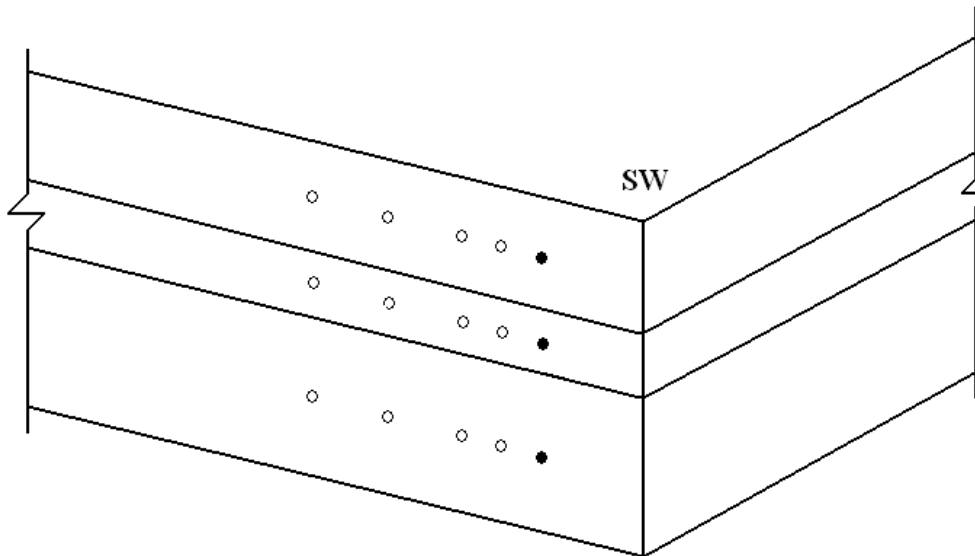
(b) Side surface SASW and DPW arrays

Fig. 3.3. Array and impact points on the three layer slab

Spectral Analysis of Surface Waves
(SASW) Results

SASW tests were performed on the top and side surfaces of the slab. The measurements on the side surface were used to determine the shear wave velocity of each material individually. The measurements recorded on the top surface testing determined the stiffness and depth profile of the system.

Once the initial data was recorded, impulse response filtration (IRF) was used to create enhanced Gabor spectrograms and mask the phase velocity plots (Joh 1996). Experimental dispersion curves were then created using the unwrapped phase spectrum from the masked phase velocities. The dispersion curves created from the different impact sources and spacings were combined to create a representative global dispersion curve. From this global representative dispersion curve, a starting model was created and an inversion process was used to determine the shear wave velocity profiles of the individual layers. Using this process, shear wave velocity data for the top, middle, and bottom layers were found to be 8560 ft/sec, 4190 ft/sec, and 8720 ft/sec, respectively. Although the top and bottom layers were originally designed to be 4000 psi and 10,000 psi, respectively, standard 28 day compressive strength tests indicated that their actual strengths were 4780 psi and 7170 psi, respectively. This helps explain the similar measured values of shear wave velocity for the top and bottom layers.

In addition to the variety of impact sources mentioned above, receiver spacings ranged from 3 in. to 72 in. The measurements recorded using these impact sources and receiver spacings, in each array, were used to determine the stiffness profile of the entire system. Synonymous with the analysis procedure for the individual layers, the phase

spectra from each spacing and impact source was masked and used to create an

experimental dispersion curve. Using IRF and Gabor spectrograms, mode transition

frequencies were identified. The frequency which represents the boundary between later

arriving, lower frequency waves and earlier arriving, higher frequency waves is known as

a mode transition frequency. Because of the multi-stiffness profile of the slab, both lower

and higher modes were identified in nearly every phase spectrum. A global

representative dispersion curve was then created based on the experimental dispersion

curves and starting velocity model parameters were set forth using guidelines presented

by Joh (1996). A forward analysis was performed to modify the starting velocity model.

An inversion process was then used to determine the shear wave velocity profile of the

system.

FFRC measurements were used to determine the Poisson's and damping ratios

used in the starting velocity model (Table 3.3). The final shear wave velocity profile is

presented in Table 3.4. Fig. 3.4 displays the global representative dispersion curve,

theoretical dispersion curve, and final shear wave velocity profile for the middle layer.

Closed circles represent the global representative dispersion curve and open circles

represent the theoretical dispersion curve. Similar curves and final velocity profiles were

determined for the top and bottom layers to compare to the values calculated for the

entire profile. The global representative dispersion curve, theoretical dispersion curve,

and final shear wave velocity profile of the entire system is presented in Fig. 3.5. The

experimental dispersion curve is a representation of the phase velocities calculated from

the SASW data measured from all arrays. The experimental data was separated into

fundamental and higher modal frequencies during the IRF analysis. Only the

fundamental mode was used resulting in a discontinuous experimental dispersion

curve. A global representative curve was then created using data from all experimental

data. The theoretical dispersion curve represents the combined velocity of all modes.

Thus, the theoretical dispersion curve does not exactly match the experimental dispersion

curve in this case, but does match the global representative dispersion curve. Once again,

the global representative curve is represented by closed circles and the theoretical

curve is represented by open circles. The final shear wave velocity profile displays

the shear wave velocity versus depth calculated during the final inversion analysis. The

depth resolution analysis showed that the data was accurate well into the soil layer

beneath the slab.

Table 3.3. Starting Model Parameters for Concrete Tunnel Model

Layer	Depth (ft)	Thickness (ft)	Vp (ft/sec)	Vs (ft/sec)	ρ (pcf)	ν	ζ
1	0.000	0.625	N/A	8400	145	0.18	0.017
2	0.625	0.375	N/A	4400	110	0.18	0.020
3	1.00	1.25	N/A	8800	155	0.20	0.010
4	2.25	2	N/A	600	125	0.3	0.02
5	4.25	Half Space	N/A	500	125	0.3	0.02

Table 3.4. Final Velocity Profile for the Concrete Tunnel Model

Layer	Depth, (ft)	Thickness, (ft)	V_p, (ft/sec)	V_s, (ft/sec)	ρ, (pcf)	ν	ζ
1	0.000	0.62	14280	8457	145	0.18	0.017
2	0.617	0.38	7393	4378	110	0.18	0.020
3	1.00	1.28	15055	8915	155	0.20	0.010
4	2.27	3.00	1309	700	125	0.3	0.02
5	5.265	Half Space	1200	650	125	0.3	0.02
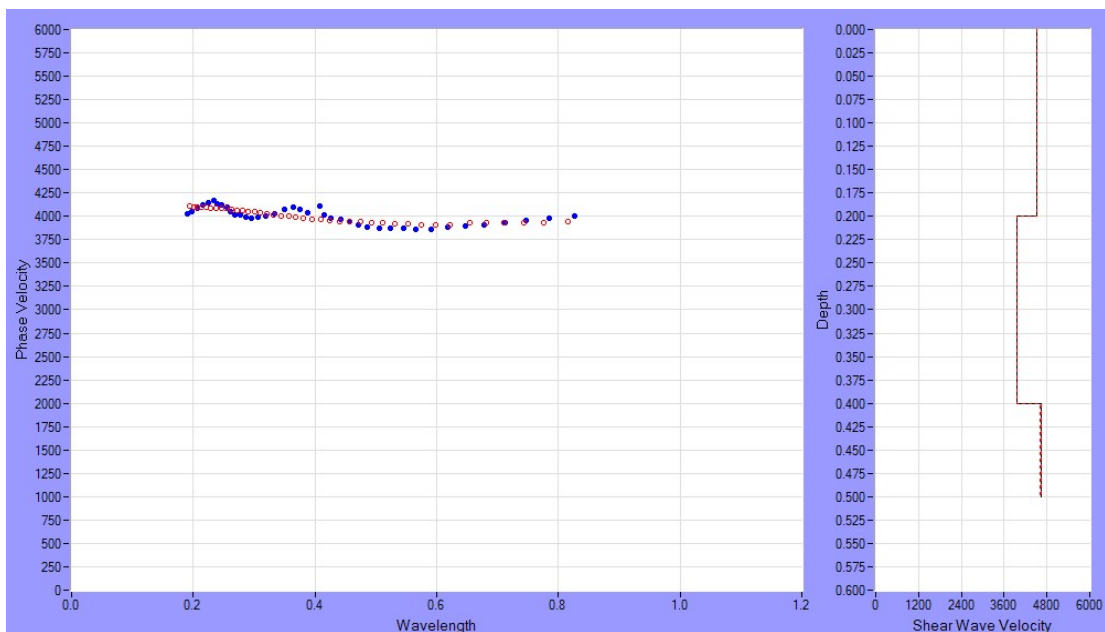
Fig. 3.4. Comparison between global representative and theoretical dispersion curves and the final velocity profile for the middle layer
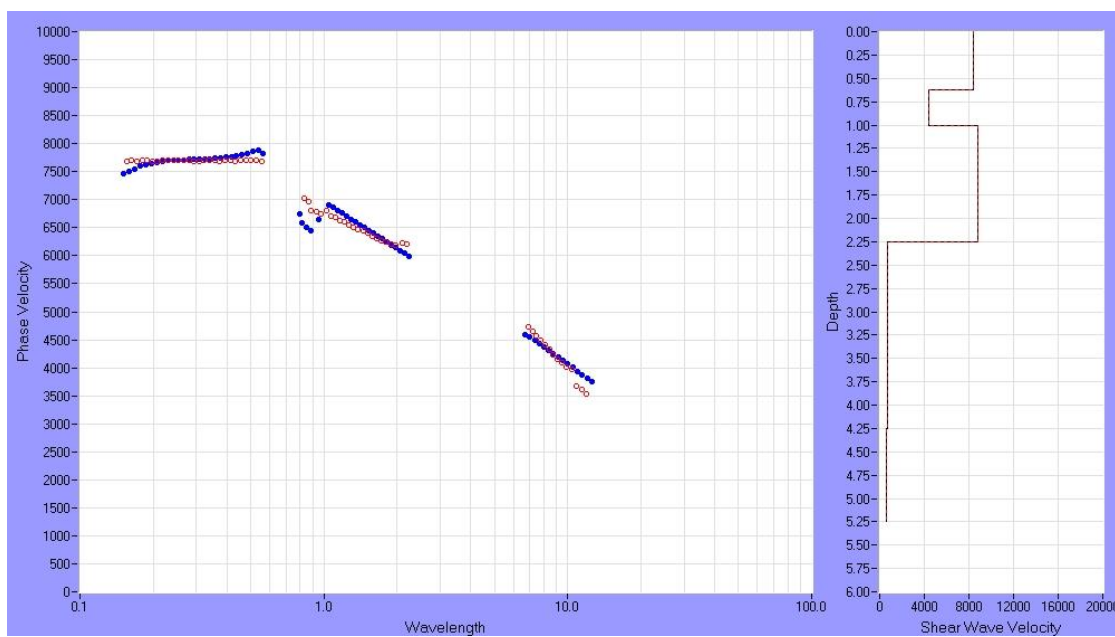
Fig. 3.5. Comparison between global representative and theoretical dispersion curves and the final velocity profile for the concrete tunnel model

Impact Echo Results

IE tests were performed simultaneously with the SASW testing using the array set up on the top surface of the slab. The peak frequencies measured using the IE method are listed in Tables 3.5 and 3.6. For these tables, void locations and impact points are shown in Figs 3.1 and 3.3, respectively. In some cases, peaks in both low and high frequency ranges were measured using one impact device. These peaks were a result of the impact source creating enough energy over a wide frequency range to produce reflections from the bottom surface of the slab and the interface between the top and middle layers, respectively. A typical frequency plot for IE measurements made with the steel sphere impact source is shown in Fig. 3.6.

Table 3.5. Frequencies (Hz) Measured Using the IE Method at Designated Impact Points

| | Impact Source | | | | | |
| | Sphere | | Hammer | | Big Hammer | |
Impact Point	Low	High	Low	High	Low	High
1	N/A	10980	2880	11070	2560	10500
2	N/A	10500	3140	11900	N/A	12400
3	N/A	11000	3070	N/A	2460	N/A
4	N/A	11400	3140	13300	2430	10500
5	N/A	10900	2750	11900	2340	12100
6	N/A	10100	2690	10900	2560	N/A
7	N/A	10400	N/A	11100	N/A	11100

Table 3.6. Frequencies (Hz) Measured Using the IE Method Above Voids

| | Impact Source | | | | | |
| | Sphere | | Hammer | | Big Hammer | |
Above Void	Low	High	Low	High	Low	High
1	N/A	13600	N/A	13700	N/A	N/A
2	N/A	12400	2840	13000	N/A	N/A
3	N/A	12700	2820	N/A	2690	N/A
4	N/A	11800	3140	11900	2370	12100
5	N/A	11500	2940	11800	2820	12500
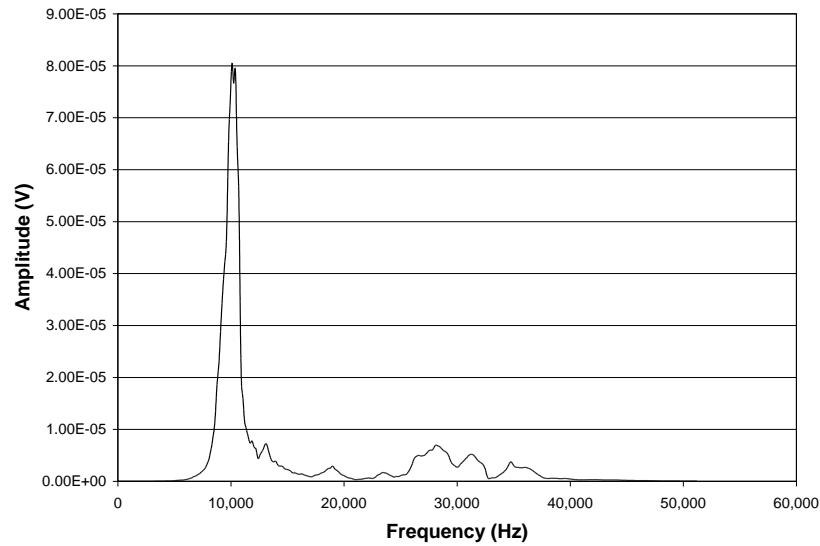
Fig. 3.6. Typical frequency plot

When using the CSWP method it is important to perform the FFRC analysis first. By calculating Poisson's and damping ratios using FFRC measurements, no assumptions are required for the SASW analysis. The depths of the individual layers are determined during the SASW analysis. Because of this, SASW testing analysis should be performed second. Finally, because either the depth of the slab or the P-wave velocity needs to be known *a priori* for the analysis of the IE data, the IE analysis is performed last. In this case, the depths of the layer(s) determined during the SASW analysis can be used directly in the analysis of the IE data to determine the P-wave velocity.

When the depth of a layer is known and a frequency is measured using the IE method, the average wave velocity for the cross section being measured can be calculated using Eq. (3.1) (Timoshenko and Goodier 1970). In this case, multiple frequencies represent the variation in wavelength and velocity across the varying cross sections. By measuring multiple wavelengths and frequencies, the changes in velocity as a function of depth can be found. In this case, two distinct frequencies from known wavelengths are

measured: a low frequency representing a reflection from the bottom surface of the slab and a high frequency representing a reflection from the bottom surface of the top layer. For instance, using the depth of 0.62 ft for the top layer found using SASW analysis (Table 3.3) and the average of all high frequency measurements listed in Tables 3.5 and 3.6, an average P-wave velocity of 14,000 ft/sec is calculated using Eq. (3.1). A similar procedure can be performed to provide an estimate of the average P-wave velocity of all three layers of concrete using the low frequency values listed in Tables 3.5 and 3.6. This average P-wave velocity was calculated as 12,600 ft/sec using the average of these values with a total depth of 2.27 ft found using the SASW method.

Another method to calculate the average P-wave velocity, V_{pavg}, across the three concrete layers can be made in a similar way that the average shear wave velocity in the top 100 ft of soil, V_{S30}, is calculated for earthquake engineering purposes. Using Equation 3.3, and the depths of the layers measured using the SASW method, an average P-wave velocity of 12,700 ft/sec was calculated (International Building Code 2006).

$$V_{pavg} = \frac{\sum_{i=1}^{n} d_i}{\sum_{i=1}^{n} \frac{d_i}{V_{pi}}} \tag{3.3}$$

where: t_i = calculated travel time of P-wave through layer i

d_i = thickness of layer i

V_{pi} = P-wave velocity of layer i

V_{pavg} = average P-wave velocity

Based on the results, it was found that there was an acceptable variation in the frequency measurements. The standard deviation calculated for the high frequencies is

820 Hz. This represents a variation in the measured P-wave velocity of +/- 1,000 ft/sec when compared to the average. This variation in velocity corresponds to a difference of 0.54 in. for the top layer. This variation is likely consistent with the variation in the actual depth of the top layer. Also, because one of the purposes of the IE method is to identify flaws in a concrete layer, a variation of this magnitude is acceptable. This is because a contractor can easily identify and repair a void in a concrete layer when the depth of the void is known within such a range.

Thus, using the combination methodology, a P-wave velocity can be calculated for the top layer and, using the averaging procedure described above, an average P-wave velocity can be calculated for the entire cross section. The importance of accurately obtaining the P-wave velocity is that, once it is known, voids can then be accurately detected.

Using Equation 3.1 with these calculated P-wave velocities and the frequency values given in Tables 3.5 and 3.6, the depths of the voids and depths of the cross sections were calculated and are listed in Tables 3.7 and 3.8. P-wave velocities of 14,120 ft/sec and 13,000 ft/sec are used for all high frequency and low frequency calculations, respectively. For Tables 3.7 and 3.8, void locations and impact points are shown in Figs. 3.1 and 3.2, respectively.

It should be noted that no frequency peaks were measured that would lead to a calculation for the depth of the bottom of the middle layer. This was due to the low impedance ratio between the soft middle layer and the stiff top layer. Essentially, the high frequency waves that enter into the middle layer are "trapped" in the layer and attenuate within it. This further reinforces the need for a combined method. Using the

CSWP method, the depths of the layers are found during the SASW portion of the analysis. If only the IE method were used, the depths of these layers would not be able to be measured.

Although there were not any embedded flaws in the bottom layer of the concrete tunnel model, the process used to average P-wave velocities mentioned above could also be used to detect a flaw in this layer. The low frequencies measured during the IE portion of the method (Tables 3.5 and 3.6) are caused by reflections from the bottom of the slab. Thus, because of the lack of reflections from the top of the bottom layer, any low frequency measured is associated with a reflection from the bottom of the slab. If a frequency is measured that results in a calculated depth that does not correlate with the depth of the bottom layer measured during the SASW portion of the method, that measurement must be assumed to be from a reflection from another boundary. In this case, the other boundary could be an internal flaw such as honeycombing or a crack, or even a section of poor concrete. Using Equation 3.3, the depth to this boundary can be found.

Table 3.7. Depths, (in.), Determined from Calculated P-wave Values at Designated Impact Points

Impact Point	Sphere	Hammer		Big Hammer	
	High	Low	High	Low	High
1	7.61	26.2	7.54	29.5	7.96
2	7.96	24.0	7.02	N/A	6.73
3	7.57	24.6	N/A	30.6	N/A
4	7.31	24.0	6.28	31.0	7.95
5	7.67	27.4	7.00	32.3	6.92
6	8.26	28.1	7.68	29.5	N/A
7	8.01	N/A	7.54	N/A	7.54
Average	7.77	25.71	7.18	30.57	7.42

The average depths for the first layer and entire slab using all impact device measurements were found to be 0.62 ft. and 2.34 ft., respectively. These values correlate within 1% and 4% with those measured using the SASW method. Also, the embedded voids were found to be an average of approximately 6.47 in. from the surface which coincides with the known thickness of the voids of approximately 1 in.

Direct P-wave Results

Measurements made using DPW tests were used to compare and validate those made using the CSWP method (Tables 3.9). P-wave calculations were obtained by dividing the distance between receivers by the travel time (Fig. 3.7). The DPW method provides data that shows an excellent correlation, within 3%, to that measured using the CSWP method.

Table 3.8. Depths, (in.), Determined from Calculated P-wave Values for Voids

	Sphere	Hammer		Big Hammer	
Void	High	Low	High	Low	High
1	5.90	N/A	5.87	N/A	N/A
2	6.49	24.3	6.18	N/A	N/A
3	6.30	25.7	N/A	26.9	N/A
4	6.77	23.1	6.74	30.6	6.63
5	7.00	24.6	6.77	25.7	6.42

Table 3.9. DPW Velocities Measurements

Layer	Impact Method	T_1 (sec)	T_2 (sec)	V_p, (ft/sec)	Avg. V_p, (ft/sec)
Top	Hammer	-3.05E-04	-2.37E-04	4600	14200
Top	Ball	-8.01E-05	-7.63E-06	13800	
Middle	Ball	-1.60E-04	-2.29E-05	7280	7280
Bottom	Hammer	-2.29E-04	-1.60E-04	14600	14600
Bottom	Ball	-7.63E-05	-7.63E-06	14600	
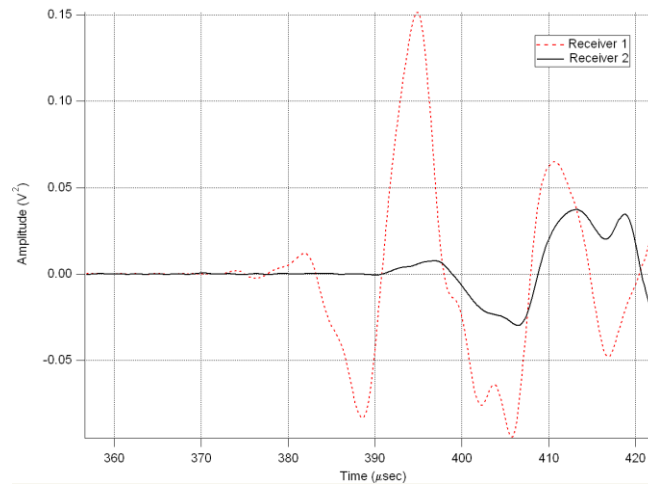
Fig. 3.7. Direct P-wave typical time domain record

Three Layer Cylinder

A 6 in. diameter x 17 in. long three layer specimen was made to study a layered system in the laboratory similar to the concrete tunnel lining model. FFRC tests were performed on the three layer cylinder to determine modal frequency changes due to the impedance ratios between the materials. Also, both ends of the cylinder were subjected to impacts. The frequencies measured are presented in Table 3.10. Because there are multiple reflections being measured due to the circular boundary of the cylinder, it is impossible to determine, without prior knowledge of the wave velocities of the separate materials, what frequency peaks are useful. This is a similar situation to that encountered when measuring the three layer slab. However, the circular boundary reflections present in the three layer cylinder are not measured on the concrete tunnel lining model. Thus, the three layer cylinder was useful in determining whether the averaging of wave velocities used on the slab during the IE analysis was practical.

Using the average rod wave velocities listed in Table 3.2, the depths associated with the first layer's V_{rod} velocity were determined. These values are listed in Table 3.11.

Table 3.10. Dominant Frequencies Measured on Three Layer Cylinder (Hz) using the FFRC Method and Multiple Impact Devices on the (a) Top and (b) Bottom Surfaces

(a)

Big Hammer	Hammer	Small Hammer	5/16 in. Ball	3/16 in. Ball	Average
3420	3420	3420	3420	3460	3428
8930	8960	8990	8990	8990	8972
N/A	11500	N/A	11600	11600	11567
13900	13900	14000	13900	13900	13920
16100	16100	N/A	16100	16200	16125

(b)

Big Hammer	Hammer	Small Hammer	5/16 in. Ball	3/16 in. Ball	Average
3390	3420	3420	3420	3460	3422
8900	8960	8930	8960	8990	8948
11500	11500	11600	11600	11500	11540
14500	14500	14400	14500	14500	14480
N/A	16800	16800	16800	16900	16825
N/A	N/A	N/A	17700	17800	17750

Table 3.11. Depths Associated with Average Frequencies Presented in Table 3.16 for (a) Top and (b) Bottom Impacts

(a)

f (Hz)	Depth (in.)
3428	20.51
8972	7.83
11567	6.08
13920	5.05
16125	4.36

(b)

f (Hz)	Depth (in.)
3422	24.04
8948	9.19
11540	7.13
14480	5.74
16825	4.89
17750	4.63

Using a micrometer, the three layer cylinder was measured to provide an estimate of an approximate depth for each layer. Average depths of 7.5 in. and 6 in. were measured for the top and bottom layers, respectively. Using these estimates, the depths of 7.83 in. and 5.74 in. listed in Table 3.11 were determined to be the depths for the top and bottom layers measured by the FFRC method. Using these depths, a depth of 3.75 in. is calculated from the total length of the cylinder of approximately 17.25 in. This value correlates perfectly with the micrometer measurement of the middle layer of 3.75 in.

Using these depths, the average rod wave velocities listed in Table 3.2, and a procedure to calculate the average rod wave velocity similar to that used to calculate the average P-wave velocity of the slab, the estimated frequencies from known boundaries can be calculated. Using this technique, estimated frequency responses for impacts made on the top and bottom surfaces were calculated and are listed in Table 3.12.

Using the average rod wave velocities calculated, the estimated frequency responses associated with the rod wave traveling the entire length of the cylinder correlate to the measured values listed in Table 3.12 within 9% for both top and bottom impacts. This indicates that the method used to calculate average P-wave velocity of the slab provides a good measurement across a profile of varying stiffness.

It should be noted that no reflection data met that which was calculated for a wave traveling through only the first two layers and then reflecting back to the point of impact. This fact, which was also noticed in the IE analysis, is due to the high impedance ratio between the stiffer layers and the middle layer.

Table 3.12. Estimated Frequency Responses from Known Boundaries for (a) Top and (b) Bottom Impacts

(a)

Reflection Boundary	Est. Frequency (Hz)
Top-Middle	8977
Bottom	3756

(b)

Reflection Boundary	Est. Frequency (Hz)
Bottom-Middle	14481
Top	3756

Conclusions

The purpose of this study was to show that a newly developed combined stress wave propagation (CSWP) method can be used as an effective procedure to determine the physical properties of a concrete tunnel structure. As such, a three layer concrete slab was built to model the in-place properties of a typical concrete tunnel structure. The proposed method involves performing both SASW and IE measurements simultaneously making a more efficient field experiment than by performing the two techniques independently. Simultaneously, the free-free resonant column (FFRC) method was used to calculate Poisson's and damping ratios and to validate a multilayer P-wave averaging procedure. As such, no material property assumptions were made in the final analysis of the data. Finally, the direct P-wave (DPW) method was used to compare and verify measurements made by the CSWP method. The results indicate that:

1.   The newly proposed CWSP method has shown to yield accurate results with

regards to P-wave velocity, void detection, and measured depth. Final analysis

shows that SASW, IE, and DPW measurements correlate within 3% for both P-wave velocities and depth. The location and depth of the five voids were identified.

2. Combining the SASW and IE procedures into one test provides the same data as performing the tests separately and is a much more efficient field experiment. Results from IE measurements correlate within 1% and 4% with those measured using the SASW method for the top and bottom layer, respectively.

3. A P-wave averaging procedure was used that was found to determine frequency response to within 9% of measured values. These results indicated that a method used to calculate average P-wave velocity on the concrete tunnel lining model provided a good measurement across a profile of varying stiffness.

4. Analyzing FFRC data first allows the analysis of the SASW to be performed without making any material property assumptions. The SASW analysis can then take place to determine the depth profile allowing the user to use the IE data to accurately determine the P-wave velocity of specific layers and identify any voids.

5. In this case, data was measured using the CSWP method that would not have been provided by performing the SASW or IE tests and analysis independently.

6. This study indicates that the CSWP method is an extremely efficient and effective tool to analyze in-place properties of concrete tunnel linings and that it could be extended for use on other concrete structures. It is useful to determine the in-place properties of the materials within the tunnel lining and also in determining the location of voids within the concrete or underlying bedrock. The method is

more efficient than performing SASW and IE alone, and by incorporating FFRC

testing, no material properties must be assumed.

CHAPTER 4

HIGH PERFORMANCE SELF-CONSOLIDATING CONCRETE

Abstract

Self-consolidating concrete (SCC) utilizes highly refined mix proportions and mixing sequences to produce a concrete that consolidates completely without the need for vibrating by flowing under its own weight. This type of concrete can result in a reduction in labor demand, accelerate curing processes and formwork removal, and allow better consolidation in areas of very dense reinforcement.

This research investigates the structural properties of concrete specimens made using two high performance SCC (HPSCC) mixes used to fabricate a series of prestressed concrete bridge girders. Because the removal of formwork for quick fabrication of the girders was of extreme importance, high design strengths were required within 1 day. A laboratory investigation was completed that measured compressive strength, static Young's modulus, and drying shrinkage measurements as a function of time. Results indicate that the two SCC mixes exhibit strength and stiffness that are larger than that of even high performance concrete. Drying shrinkage results indicate that the HPSCC measured exhibits shrinkage characteristics within the range of other SCCs reviewed in existing literature.

Introduction

Self-consolidating concrete is a relatively new type of concrete characterized by its ability to consolidate completely under its own weight. This type of concrete can be used to increase production quality and efficiency while reducing labor costs because of

its ability to consolidate without the need for vibration. This allows for quality

placements of SCC without the need for large casting crews. These characteristics are

achieved by a stringent mix design that produces the fundamental rheological properties

of SCC. Rheology is the study of the deformation and flow of matter under the influence

of an applied stress. In the case of SCC, the applied stress is simply the self weight of the

material and the fundamental rheological properties required to obtain such flow are

based on a low yield stress, moderate viscosity, and retention of the kinetic energy of the

flowable mix by the reduction of the volume of coarse aggregate (Bonen and Shah 2004).

Typically, the low yield stress is attained through the addition of a high range

water reducer, or super plasticizer. The flow characteristics of the mix are obtained

through specific combinations of course to fine aggregate volume, composition of the

cementitious materials, and overall reduction of course aggregate volume. Finally, the

viscosity is controlled through the w/c ratio, amount of super plasticizer, and the possible

addition of a viscosity enhancing agent (VEA). All of the properties are essential to limit

the interparticle friction among the course aggregate, sand, and cementitious materials

included in the mix (Bonen and Shah 2004; Khayat 1999).

The amount of super plasticizer required becomes a function of the amount of

course aggregate. Because the amount of course aggregate is reduced, the amount of

cementitious materials required is increased. Often, SCC has large amounts of pozzolans

such as fly ash, oven blasted furnace slag, or kaolin to increase the volume of the

cementitious materials without the need for a large portion of cement. The w/c ratio is

then decided upon through trial batches to insure high fluidity using an inverted slump

test (Fig. 4.1). The targeted shape and size of the concrete flow is perfectly circular with

a diameter of 22 in. to 26 in. (ASTM C 1611 – Standard Test Method for Slump Flow of Self-consolidating Concrete (2005)).

In order to ensure flowability, the w/c is typically kept at a low ratio (0.3) and a super plasticizer is added to enhance the cohesiveness of the paste and allow the material to maintain adequate performance with regards to strength, durability, and stiffness. However, this low w/c ratio may require a relatively high doses of super plasticizer. Other approaches allow for the w/c ratio to be as high as 0.45 with the addition of a VEA and less super plasticizer required. The use of both a VEA and a super plasticizer allows the mix to achieve design performance parameters while ensuring high flowability (Khayat 1999).

Fig. 4.1. Inverted slump test

Background

The concept of SCC is not new. However, the consistency of its design specifications and performance standards among the existing literature is widely variable.

Khayat (1999) performed an investigation of the workability, testing, and performance of seven self-consolidating concrete mixes. In this investigation, the seven concrete mixes used varied in cementitious volume as well as composition. The w/c ratio varied from 0.35 to 0.50 and the addition of super plasticizer and VEA was varied with each mix. He found that the reduction of cementitious material content and increase in coarse aggregate volume caused some interference with concrete deformability in narrow areas such as narrowly spaced reinforcement. The incorporation of VEA at moderate dosages was shown to enhance deformability and stability, despite larger w/c ratios. Khayat performed only relative flow resistance, relative viscosity, filling capacity, settlement, and flow time measurements. Although this investigation is extremely important with regards to the flowable characteristics of SCC, it gives little insight as to what mix proportions lead to which performance properties such as strength or stiffness.

Khayat et al. (2000) investigated the performance of SCC for casting basement and foundation walls. In this study, two SCC mixes were used that were found to be optimized for casting concrete in narrow spaces with a high density of reinforcement. The two mixes used varied in both cementitious volume and content as well as aggregate distribution, super plasticizer content, and VEA content. Compressive strength measurements were made on control cylinders and cored cylinders from the walls constructed using the SCC. Young's modulus measurements were made only on the control cylinders. Control cylinder compressive strengths were measured to be 2320 psi

and 1250 psi at 1 day and 6570 psi and 8370 psi at 28 days for the two mixes, respectively. Compressive strengths measurements of the cored samples varied from 4130 psi to 5660 psi and 5980 psi to 7220 at 56 days for the two mixes, respectively. Young's modulus was measured to be 4500 ksi and 4420 ksi at 28 days for the two mixes, respectively.

Khayat et al. (2000) performed a study on the optimization and performance of air-entrained SCC. The investigation included two phases. The first phase involved nine trial batches and fourteen mixtures that were prepared with different concentrations of cementitious materials, VEA, and super plasticizers. The second phase involved five optimized mixtures that were chosen to ensure good balance between restricted deformability and resistance to surface settlement, super plasticizer and VEA demands, and material costs. The second phase mixtures were tested for compressive strength, Young's modulus, and drying shrinkage development, among other tests. Compressive strengths ranged from 440 psi to 1450 psi at 1 day and 4200 psi to 7100 psi at 28 days for the five mixes. Young's modulus ranged from 3630 ksi to 4500 ksi at 28 days. The drying shrinkage values after 180 days of drying ranged between approximately 0.0150 and 0.0240 in./in.

Kaszynska (2006) investigated the effect of temperature on properties of fresh SCC. Two SCC mixtures were made based on optimized results of previous studies. The two SCCs were tested for slump, heat of hydration, compressive strength, and Young's modulus, among other tests, as a function of curing temperature. Compressive strengths varied between 4300 psi and 6720 psi at 1 day and 10460 psi and 11020 psi at 28 days for the two mixes, respectively. Young's modulus measurements varied between 2930 ksi

and 4270 ksi at 1 day and 4940 ksi and 5420 ksi at 28 days for the two mixes,

respectively. The investigation indicated that the initial temperature of the concrete had a

large influence of the growth of the mechanical properties.

Naito et al. (2006) investigated the performance of bulb-tee girders made with

SCC. A total of four 35-ft girders were produced. Two girders were fabricated using

high early strength concrete (HESC) and two were fabricated using SCC. The

investigation found that both concretes gained over 90% of their design 28 day

compressive strengths within the first 24 hours. The actual compressive strengths were

not reported but appear to be approximately 8000 psi and 9000 psi at days 1 and 28 for

the SCC, respectively, from Fig. 1 of the report. The average Young's modulus

measured was approximately 5000 ksi. Also, shrinkage values at 56 days were found to

be between 0.0002 in./in. and 0.0003 in./in.. The investigation found that early strength

gain properties of SCC were comparable to those of HESC. ACI 209 over predicted the

shrinkage characteristics of the SCC. The ACI-estimated creep coefficient calculated for

the SCC was less than the actual value. The in place creep and shrinkage were

consistently lower than estimates, resulting in less prestressing force losses in the girders.

The SCC girders exhibited fewer losses than the HESC girders. At 28 days, the effective

prestress was 16% higher than the PCI estimated values. Their final results indicated

that, although SCC is not used significantly in pretensioned concrete bridge members due

to stringent material quality control standards specific by states' departments of

transportation, the studied SCC provided mechanical properties that outperformed current

industry recommendations.

Material Testing Program

The Utah Department of Transportation (UDOT) requires that concrete mix designs used to construct prestressed concrete bridge girders meet certain requirements. It was the goal of this investigation to determine the properties of two SCC concrete mixes sampled from a prestress precasting plant in Magna, Utah. For proprietary reasons the two mix designs were unobtainable.

Concrete samples for the two mixes were taken independently from front delivery concrete trucks on March 12, 2007 and October 9, 2007, respectively. The material was sampled and specimens were made in accordance with ASTM C31 (2003), Standard Practice for Making and Curing Concrete Test Specimens in the Field. Specimens included a variety of 4 in. x 8 in. and 6 in. x 12 in. cylinders and 3 in. x 3 in. x 17 in. beams. The 4 in. x 8 in. specimens were typically used for compressive strength measurements, while the 6 in. x 12 in. cylinders were typically used for static Young's modulus measurements. The beams were used to measure drying shrinkage.

Results

Compressive strength and static Young's modulus measurements are presented in Table 4.1. The American Concrete Institute (ACI) committee 209 suggests Eq. (4.1) to calculate compressive strength as a function of time.

$$f_{cm} = f_{c28}\left(\frac{t}{4 + 0.85t}\right) \qquad (4.1)$$

where: f_{cm} = mean compressive strength at age t days

f_{c28} = mean 28-day compressive strength

t = time in days.

Values calculated using Eq. (4.1) are presented with measured values in Fig. 4.2.

Equations suggested by ACI committee 318 (Eq. (4.2)) and the Prestressed

Concrete Institute (PCI) (Eq. (4.3)) are presented along with measured values in Fig. 4.3.

$$E_s = 33000 w_c^{1.5} \sqrt{f_c'} \qquad (4.2)$$

$$E_s = \left(40000\sqrt{f_c'} + 1000000\right)\left(\frac{w_c}{145}\right)^{1.5} \qquad (4.3)$$

where: E_s = static Young's modulus of elasticity

w_c = weight of concrete

f_c' = compressive strength of concrete.

Measurements of shrinkage are presented in Fig. 4.4 along with values

calculated using Eq. (4.4) recommended by AASHTO LRFD 2004 Specifications.

$$\varepsilon_{sh} = k_s k_h \left(\frac{t}{35+t}\right) 0.51 \times 10^{-3} \qquad (4.4)$$

where: ε_{sh} = strain due to shrinkage

k_s = size factor

k_h = humidity factor

t = drying time.

Discussion of Results

The HPSCC mixes testing during this investigation exhibit measured properties of

compressive strength and static Young's modulus that are much higher than those

reviewed in the existing literature.

Minimum compressive strengths measured at 1 day of the HPSCC exceed all

standard cured SCC specimens compressive strengths posted in the literature by 160%.

Twenty-eight day and 56 day measurements exceed those posted in the literature by an average of 47% and 44%, respectively. The measured values exceed values calculated using Eq. (4.1) by up to 311% at day 1 measurements. However, calculated values correlate with measured values within 8%, 7%, and 10% at days 14, 28, and 56. Values of compressive strength at the final day measured were 15500 psi and 14800 psi for mixes 1 and 2, respectively.

Static Young's modulus measurements of the SCC exceed 28 day and 56 day measurements of SCC posted in the literature by a minimum of 1% and 18% respectively. Eq. (4.2) underestimates the measured modulus by 27% at day 1, correlates within 12% at day 3, and then begins to overestimate the measured values by as much as 29% at day 56. The equation suggested by PCI for high strength concretes correlates much better with the measured values. Results again indicate an underestimation of as much as 25% at early ages. However, from an age of 7 days on, the calculated values determined using Eq. 4.3 correlate within a maximum of 15% with measured values. Values of static Young's modulus at the final day measured were 6.4 x 10^6 psi and 6.2 x 10^6 psi, for mixes 1 and 2, respectively.

The average 56 day drying shrinkage for mixes 1 was 0.00040 in./in.. This value exceeded measurements made by Naito et al. by a factor of approximately 2 (Naito et al. 2006). However, this measurement was minute compared to those measured by Khayat of 0.015 in./in. and 0.024 in./in. (Khayat et al. 2000). The SCC mix correlates well with a maximum difference of 15% when compared to values calculated using Eq. (4.4).

Table 4.1. (a) Compressive Strength Measurements (b) Static Young's Modulus
Measurements

(a)

Days after Casting	Mix 1		Mix 2	
	Load (lb.)	f'c (psi)	Load (lb.)	f'c (psi)
1	106209	8452	77169	6141
1	103699	8252	74825	5954
3	130759	10405	105223	8373
3	126313	10052	137702	10958
7	135282	10765	122474	9746
7	147390	11729	127473	10144
14	149990	11936	138246	11001
14	154171	12269	139284	11084
28	160736	12791	151423	12050
28	161867	12881	157200	12510
56	180397	14356	161375	12842
56	164793	13114	157762	12554
Final	195303	15541	185690	14776

(b)

Days after Casting	Mix 1 E_s (psi)	Mix 2 E_s (psi)
1	4.09E+06	3.30E+06
1	4.33E+06	3.34E+06
3	4.58E+06	3.94E+06
3	4.63E+06	4.10E+06
7	4.71E+06	4.42E+06
7	4.84E+06	4.50E+06
14	4.65E+06	4.78E+06
14	5.03E+06	5.20E+06
28	5.60E+06	4.86E+06
28	5.42E+06	4.77E+06
56	5.63E+06	4.90E+06
56	5.71E+06	5.25E+06
Final	6.39E+06	6.22E+06
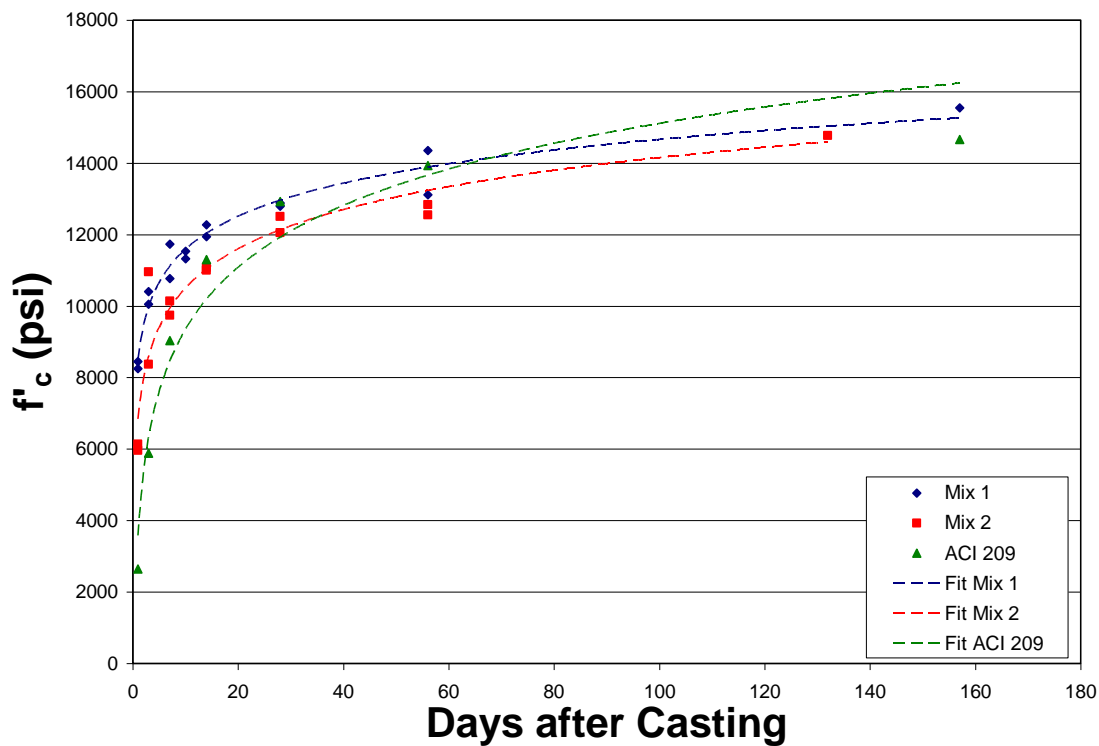
Fig. 4.2. Compressive strength measurements
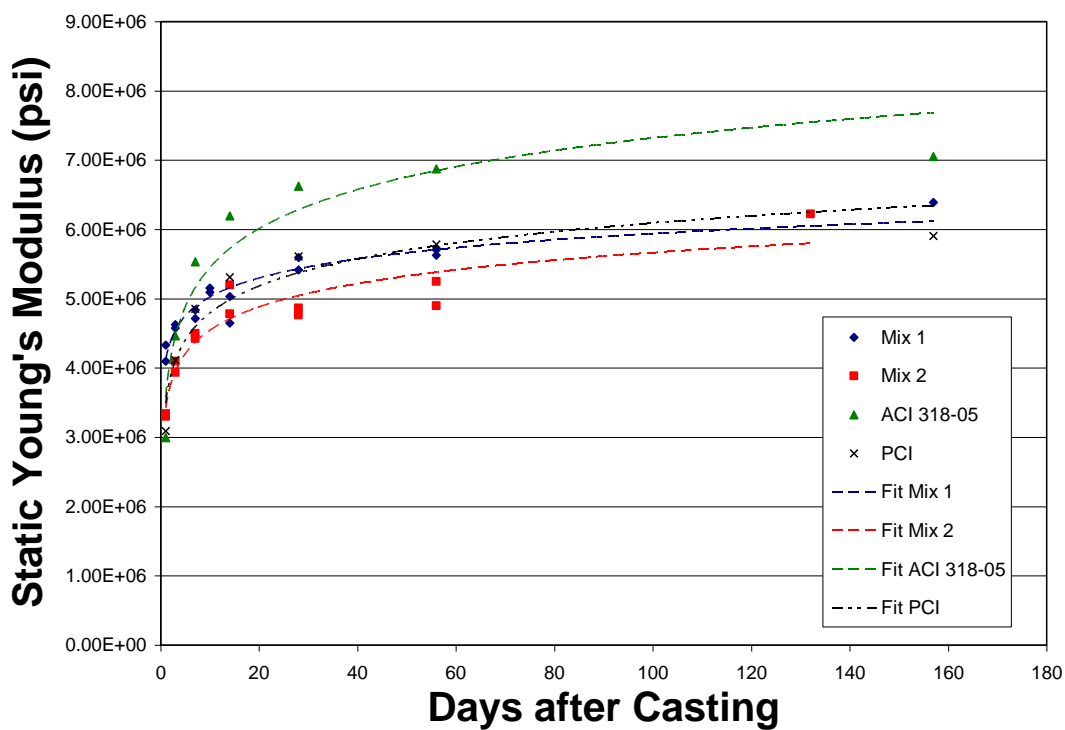
Fig. 4.3. Static Young's modulus measurements
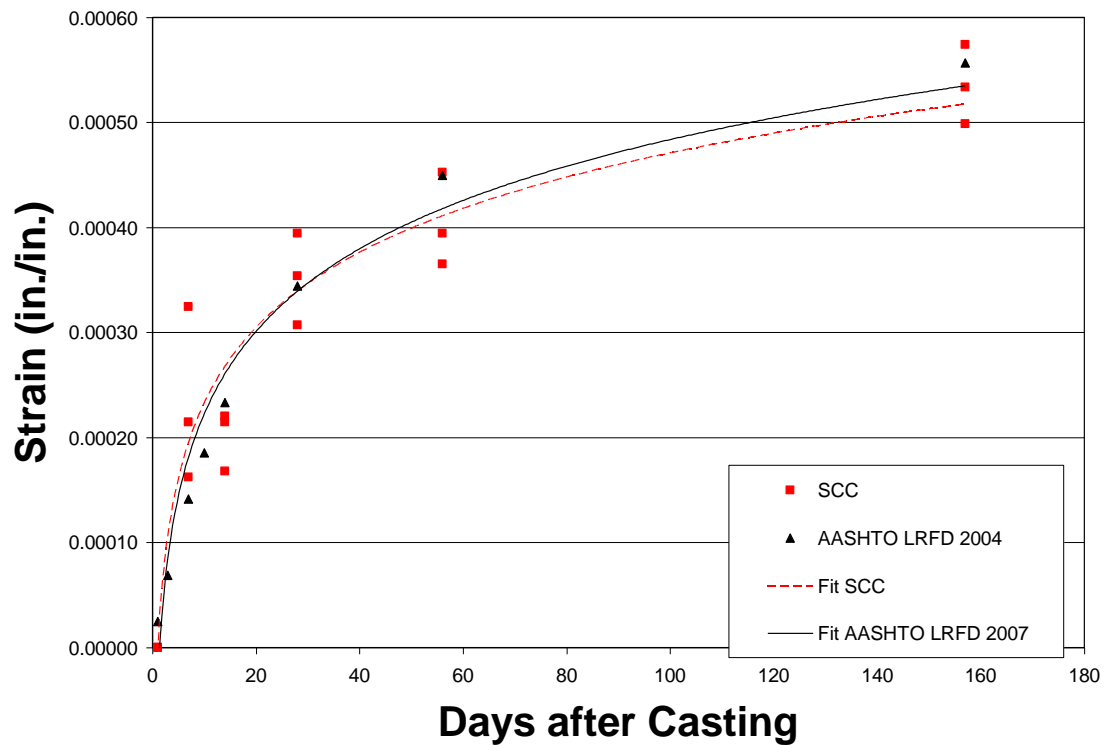
Fig. 4.4. Drying shrinkage measurements

Conclusions

A laboratory investigation was completed on two high performance self consolidating concrete (HPSCC) mixes to measure compressive strength, static Young's modulus, and drying shrinkage as a function of time. Results indicate that these concretes exhibit strength and stiffness far beyond that of even high performance concrete.

Compressive strengths measured on HPSCC specimens at days 1, 28, and 56 exceed those posted in existing literature by a minimum 160%, 47%, and 44%, respectively. The measured values exceed values calculated using an equation suggested by ACI committee 209 by up to 311% at day 1 measurements. However,

calculated values correlate with measured values within 8%, 7%, and 10% at days 14, 28, and 56.

Static Young's modulus measurements of the SCC exceed 28 day and 56 day measurements of SCC posted in the literature by a minimum of 1% and 18% respectively. An equation suggested by ACI committee 318 underestimates the measured modulus by 27% at day 1, correlates within 12% at day 3, and then begins to overestimate the measured values by as much as 29% at day 56. However, the equation suggested by PCI for high strength concretes correlates much better with the measured values. Results again indicate an underestimation of as much as 25% at early ages. However, from an age of 7 days on, the calculated values determined using Eq. 4.3 correlate within a maximum of 15% with measured values.

Drying shrinkage results indicate that the HPSCC measured exhibits shrinkage characteristics within the range of other SCCs reviewed in existing literature. The SCC mix correlates well with a maximum difference of 15% from values calculated using an equation suggested by AASHTO LRFD 2004 Specifications.

CHAPTER 5

THE USE OF STRESS WAVE PROPAGATION TO QUANTIFY DAMAGE IN

CONCRETE SPECIMENS

Abstract

The development and coalescence of microcracks is the reason a concrete member fails. As concrete is loaded, work is performed through the opening of microcracks or the absorption of energy. This growth of microcracks in concrete specimens has been found to affect the propagation of stress waves. Unconstrained compression waves were measured in this study to determine the variation in first mode longitudinal frequency and damping ratio as a function of cyclic loading to failure. The amount of absorbed energy by various concrete specimens was calculated from hysteretic curves measured during testing. Several concrete mixes were sampled to include a variety of compressive strengths. As part of the research, a new device was developed to induce a short impulse excitation to the concrete specimens as they were being loaded. This new device allowed for fast testing that produced accurate results. Longitudinal frequency and cumulative energy variations were shown to depend on concrete strength. These results imply that the ability of higher strength concrete to more easily absorb energy restricts the growth of microcracks. Thus, a new damage model is proposed that is a function of compressive strength, modal frequency, and energy.

Introduction

Methods to determine the in-place physical properties of concrete structures are important tools to engineers and researchers. Code based procedures that result in the

evaluation of the integrity of existing structures depend on accurate material properties to correctly determine the condition of these structures. Currently, there are many such methods (i.e. stress wave propagation methods) in existence that allow engineers to determine these material properties. However, these tools and techniques have been developed under the assumption that dynamic material measurements are not affected by the inherent stress history applied to structures by self weight, super imposed dead loads, and live loads. Such loading causes fatigue and damage in the form of microcracking that can change a structures behavior with regards to wave propagation. These long-term changes in the propagation velocities of stress waves should be understood so that nondestructive measurements of existing structures are not only quantitative, but also correctly analyzed.

In the case of a heterogeneous material like concrete, the assumption that it is homogenous is made in order for the basic theories and techniques of stress wave propagation methods to be applicable. The result is that the waves that can be measured are typically of wavelength sizes that are too large to determine properties such as porosity, interfacial bond quality between aggregate and matrix material, or the presence of microcracks. Instead, the wave characteristics measured during these tests represent the average physical properties of the concrete structure or specimen analyzed (i.e. a homogenous measurement).

When concrete is loaded with any significant amount of stress, microcracks form. These cracks typically begin to form around the aggregate to matrix interfaces and then spread as more stress is applied. It is the eventual growth and coalescence of these microcracks that causes the failure of concrete (Neville 1996). Because the growth of

microcracks leads to the failure of concrete, it is reasonable to assume that the growth of these cracks is a good indicator of damage.

Several methods have been developed to model the damage in concrete structures. The majority of these models use energy-related damage indicators to quantitatively assess the damage in such structures (Rao et al. 1998; Garstka et al. 1993; Sadeghi et al. 1993; Park and Ang 1985). Also, Hsu (1981) has developed relationships for the calculation of fatigue of plain concrete to incorporate indicators such as stress versus number of cycles, ratio of minimum stress to maximum stress, and rate of loading. Other models have used other various indicators such as splitting tensile strength (Gettu et al. 1996), stress-strain relationships (Gao and Hsu 1998; Bahn Hsu 1998), and strain-cycle relationships (Alliche and Francois 1989).

As cycling and fatigue occurs in concrete, the primary reason for a decrease in structural related properties is the continuous microcrack growth. Thus, research interest to investigate procedures to measure the growth of these cracks has been conducted (Suaris and Fernando 1987; Suaris et al. 1990; Nogueria and Willam 2001). All of these studies have incorporated nondestructive testing (NDT) techniques to quantify crack growth as a function of loading cycles. Measurements of pulse velocity, acoustic emission, and ultrasonic wave attenuation are methods that have been used to determine the growth of microcracks. All of these methods use similar techniques to excite the specimens and measure the elastic wave characteristics of the material during and after the specified loading cycles. The free-free resonant column (FFRC) method has been used to quantify damage in terms of the fundamental longitudinal, transverse, and torsional frequencies as well as damping (Gheorghiu et al. 2005). The results from all of

the NDT research indicate that measurements of elastic wave properties are a good indicator of damage in concrete.

A more recent study (Shokouhi 2008) indicates that not only are the elastic properties of the material dependent on the growth of microcracks, but also on the closing of microcracks. Shokouhi has shown in a feasibility study that surface wave velocities propagating parallel to the direction of loading demonstrate a distinct stress sensitive behavior. During this study, surface wave velocities were measured while concrete specimens were uniaxially loaded to 35% and 80% of the ultimate compressive strength. Her results indicate that as load and inherent stresses increase, microcracks in the specimens close and the surface wave velocities increase.

There is also an anisotropic behavior of elastic waves in loaded concrete specimens that depends on the direction of loading relative to the direction of wave propagation (Shokouhi 2008). Thus, the presence of microcracks forming in the same direction of loading can be measured by determining the changes in stress wave propagation in that direction.

Studies that have used the FFRC method to determine the decrease in fundamental longitudinal, transverse, and torsional frequencies have shown that for a specific concrete mix, these natural frequencies decrease (Gheorghiu et al. 2005). However, a trend to quantify this reduction has not been determined. It is the goal of this study to show that for a variety of concrete specimens varying in strength, a general trend exists for all concrete specimens and a specific trend exists for defined concrete strengths with regards to the decrease in first mode longitudinal frequency and increase in damping

ratio. This information will provide engineers a new tool to continue the development of

the understanding of concrete behavior in fatigue.

The variation in longitudinal compression wave velocity, damping ratios, and

energy absorption of a variety of concrete specimens under fatigue loading conditions is

investigated in this study. The details of the concrete mixes tested, instrumentation used,

experimental setup, and the methods of measurement and analysis are provided. The

theoretical background applying to wave propagation in elastic solid media is briefly

discussed. The measurement results of the changes in dynamic properties as well as the

cumulative energy absorbed during cyclic loading of several concrete mixes are

presented.

**Review of the Basic Theory of the
Propagation of Waves in Elastic
Solid Media**

Short duration impulses applied to an elastic body produce a variation of stresses

that can most easily be described using equations of equilibrium in terms of

displacements and described in rectangular coordinates. Assuming there are no body

forces, and adding inertial forces caused by the imposed excitation, the equation of

equilibrium for displacement in the x direction is (Timoshenko and Goodier 1970):

$$(\lambda + G)\frac{\partial e}{\partial x} + G\nabla^2 u - \rho\frac{\partial^2 u}{\partial t^2} \tag{5.1}$$

where: ρ = mass density

u = displacement in the x direction

t = time

G = shear modulus

$$\lambda = \frac{\nu E}{(1+\nu)(1-2\nu)} \tag{5.2}$$

$$G = \frac{E}{2(1+\nu)} \tag{5.3}$$

$$\nabla^2 = \frac{\partial^2}{\partial x^2} + \frac{\partial^2}{\partial y^2} + \frac{\partial^2}{\partial z^2} \tag{5.4}$$

$$e = \frac{1-2\nu}{E}\theta \tag{5.5}$$

$$\theta = \sigma_x + \sigma_y + \sigma_z \tag{5.6}$$

where: E = Young's modulus

σ_i = stress in the i direction

ν = Poisson's ratio of the material

There are two types of waves that satisfy the solution to Eq. (5.1), waves of dilation and waves of distortion. Waves of dilation are irrotational, and by solving Eq. (5.1) to satisfy the assumption that an elastic body subjected to forces has no rotational displacements the equation becomes (Timoshenko and Goodier 1970):

$$(\lambda + 2G)\nabla^2 u - \rho \frac{\partial^2 u}{\partial t^2} = 0 \tag{5.7}$$

When an excitation is produced at a point on an elastic medium, waves radiate from the point where the disturbance occurred in all directions. At great distances from this point of disturbance, however, it may be assumed that all particles are either moving parallel to the direction of wave propagation or perpendicular to that direction. The particles that are moved in a parallel manner are moved by waves of dilation and produce longitudinal waves (Timoshenko and Goodier 1970).

In the case of longitudinal waves propagating in the x direction, u becomes a function of x only and Eq. (5.7) can be described as (Timoshenko and Goodier 1970):

$$\frac{\partial^2 u}{\partial t^2} = V_p^2 \frac{\partial^2 u}{\partial x^2} \tag{5.8}$$

$$V_p = \sqrt{\frac{E(1-\nu)}{(1+\nu)(1-2\nu)\rho}} \tag{5.9}$$

When these plane longitudinal waves exist in bars of rectangular cross section and the lateral surface is free, there is a simple approximation to solve for the stress and strain conditions present due to particle displacements in the x direction. In this approximation, each cross section of the bar is considered to be in tension corresponding to the axial strain caused by the longitudinal waves, $\partial u/\partial x$, where u is a function of x and t only. Because the other stress components are considered negligible, this leads to (Timoshenko and Goodier 1970):

$$\sigma_x = E \frac{\partial u}{\partial x} \tag{5.10}$$

Considering an element between cross sections at x and $x+dx$, the equation of motion can be described as (Timoshenko and Goodier 1970):

$$\frac{\partial^2 u}{\partial t^2} = V_{Rod} \frac{\partial^2 u}{\partial x^2} \tag{5.11}$$

$$V_{Rod} = \frac{V_p}{\sqrt{\frac{1-\nu}{(1+\nu)(1-2\nu)}}} = \sqrt{\frac{E_d}{\rho}} \tag{5.12}$$

Because Eq. (5.12) defines that the rod-wave velocity is dependent on the dynamic modulus of elasticity, it is apparent that as the stiffness of a material

deteriorates, the rod-wave velocity will also decrease. When a disturbance is caused in a bar of rectangular cross section and known length, *l*, the first mode longitudinal frequency can be described as (Rayleigh 1976):

$$V_{Rod} = f_l \lambda \qquad (5.13)$$

where: f_l = first mode longitudinal frequency

λ = wavelength, $2l$

Thus, by measuring the first mode longitudinal frequency of a bar of rectangular cross section, the stiffness of that material can be determined. Also, as the stiffness varies due to fatigue, this variation can be determined by measuring the first mode longitudinal frequency.

The theory and measurement of rod waves in concrete is relatively simple and has been performed by numerous researchers. However, research regarding the measurement of rod wave's frequency during cyclic testing is rare. Many researchers have used piezoelectric devices to excite concrete specimen. However, because the measurements recorded on the concrete specimens during this study were analyzed in the frequency domain, the excitation device had to be one that would not ring after excitation. Piezoelectric devices such as accelerometers that are sometime used to excite concrete specimens unfortunately have this ringing characteristic, and thus, for this research, a new device was developed.

New Instrumentation

There were several iterations of the design during the development of the new excitation device. However, the core design philosophy remained consistent. When a

copper coil is subjected to a voltage, a magnetic field is produced. By placing a series of magnets within this copper coil, the magnets are forced to move directly with the change in voltage. When the magnets are in a free boundary condition, they move up and down within the coil. However, when they are forced against another surface, they exert a force on that surface. By placing a spring loaded series of magnets within a copper coil, the free end of the magnets can be set against a surface to exert a short duration force against it. Thus, it was decided to build a device to produce short duration impulse forces using these ideas. The core design consisted of a spring loaded series of magnets surrounded by a copper wire coil (Fig. 5.1).

Originally, the coil and magnets were fitted into a PVC housing (Fig. 5.2) to provide the coil and springs into a fixed position. This housing was meant to sit flush against one end of the concrete cylinder to force the magnets against the concrete surface as it was loaded cyclically. This would ensure the impulses produced by the movements of the magnets would exert a force onto the cylinder. Because the PVC housing could not support the loads to which it was subjected to during the tests, a specialized aluminum end plate was fabricated to allow the device to sit on the end of the concrete specimen during compression tests (Fig. 5.3). A similar aluminum end plate was fabricated so that a unidirectional accelerometer could be mounted on the opposite end to measure the wave propagation created by the excitation device.

It was quickly discovered that the PVC housing simply was not rigid enough to provide adequate protection for the magnetic coil. The neoprene rings that were used as end plates were continuously squeezing in on the PVC housing during the compression tests causing the entire device to be crushed. Therefore, the design was reduced in size to

avoid being crushed by the neoprene pads. The new design consisted of two small steel

plates connected to a series of magnets surrounded by a small copper coil (Fig. 5.4). The

entire assembly was then protected by a thin plastic tube (Fig. 5.5). The plastic tube

restricted the movement of the copper coil, however, and the design was disregarded.

(a) Copper coil

(b) Spring attached to series of magnets
Fig. 5.1. Core design of new instrumentation

Fig. 5.2. PVC housing

(a) Top of aluminum housing
Fig. 5.3. Aluminum housing

(b) Bottom of aluminum housing
Fig. 5.3. (continued)

The original design was then modified to include a stronger housing. Several copper coils were made and fit into aluminum and steel tube housings. However, the end of the coils was continuously crushed during the compression tests. A coil was then fit into a steel housing and potted with epoxy for protection (Fig. 5.6). This design worked adequately, but due to the creep of the epoxy, the coil was crushed inwards towards the spring loaded magnet assembly and the magnets were not able to move freely (Fig. 5.7). Finally, an aluminum tube was placed on the interior of a magnetic copper coil which was housed in a steel tube. The entire assembly was potted with 2500 psi epoxy (Fig. 5.8). This final design of the excitation device allowed continuous measurements while the specimen was being tested.

Because of the intense pressures associated with the cyclic compression tests, the recorded data also included a great deal of background noise. As a result, it was very

difficult to interpret the correct longitudinal frequencies and associated half power bandwidths. An experiment to mount the excitation device on the side of the specimen was conducted and it was found that adequate energy was produced in the longitudinal direction to allow for this configuration (Fig. 5.9).

Fig. 5.4. Copper coil with steel end plates

Fig. 5.5. Plastic tube housing

Fig. 5.6. Steel housing with epoxy protection

Fig. 5.7. Coil crushed inwards

Fig. 5.8. Final design

Fig. 5.9. Excitation device mounted on side (in circle)

Fig. 5.10. Final configuration for experiment (LVDT on right, excitation device on left)

Finally, the extensometer with an LVDT was mounted on the cylinder to measure static axial stress-strain behavior during the cyclic tests completed the configuration for the experiment (Fig. 5.10).

A compression machine was controlled by a servo unit capable of loading and unloading the concrete specimens at specific rates was used to apply force to the cylinders at specified percentages of their predetermined ultimate compression strength. Simultaneously, the LVDT on the extensometer measured changes in axial length which was used to calculate strain. From this data, load-deflection hysteretic curves were created. Before and after each loading cycle, the excitation device was turned on and readings of first mode longitudinal frequency and the half power bandwidth were measured. The cylinder was then immediately loaded again. Cylinders were tested in this manner until failure.

Experiment

Five concrete mixes were tested which included the effects of multiple aggregate types, water / cement ratios, and cement types. This range in concrete mixes was chosen in order to measure concrete properties representing several different compressive strengths. The concrete designs ranged in mix proportions and had 28 day compressive strengths ranging from 1880 psi to 12560 psi (Table 5.1). Concrete specimens were 4 in. x 8 in. and 6 in. x 12 in. cylinders.

The stress-strain curve calculated from measurements of concrete specimen, when loaded in compression, is typically linear up to 40% of the compressive strength. Thus, cylinders were tested cyclically at loads ranging from zero to 50% - 90% of the compressive strength in order to determine a good testing range for the specimen. In order to produce an ideal experiment, several criteria were established. First, the specimens were loaded to a range at which the measured stress-strain curve became nonlinear, ensuring some type of irreversible damage. Secondly, the desired range of cycles was set to be more than 5, but less than 100. This was to ensure an efficient experiment. Finally, the desired failure would occur gradually, rather than during a single cycle. This final criterion was put into place in an effort to quantify the final stages of damage before failure.

After testing several specimens, it was decided that the most effective and efficient experiment would be as follows. Four cylinders from each strength class were loaded cyclically with an initial load at 80% of their respective ultimate compressive strength. The load was increased each cycle in 1% increments up to 90%. Once the 90% mark was reached, the cylinders were loaded cyclically at that magnitude until failure.

Table 5.1. Mix Designs for 0.5 ft^3 and 28 Day Compressive Strengths

Mix	Cement	Fly Ash	Course Aggregate	Fine Aggregate	water	w/c ratio	f'c (psi)
Low Strength	9.5	0.0	0.0	70.0	4.9	0.51	1880
Low/Medium Strength	12.6	0.0	38.6	34.0	5.4	0.43	3800
Medium Strength	10.3	1.9	25.1	29.7	5.0	0.48	5350
Medium / High Strength	13.2	3.3	29.4	19.0	5.2	0.39	8920
High Strength			Proprietary				12560

Some cylinders failed before the 90% mark was reached. After each cycle, longitudinal frequencies were measured using an innovative source, acceleration transducer, and digital signal analyzer. The first mode longitudinal frequency and the half power bandwidth of the frequency peak were recorded after each cycle.

In addition to monitoring the longitudinal frequency, an extensometer with a DC-DC linear voltage displacement transducer (LVDT) was used to measure the displacement of the concrete samples as they were loaded. These measurements were used to produce hysteretic curves which allowed the calculation of the absorbed energy absorbed by the specimen during each cycle.

Results

Measurements of the first mode longitudinal frequencies and half power bandwidths were recorded at the end of each cycle on every examined specimen. Simultaneously, load and deflection measurements were recorded during each cycle. Initial, undamaged frequencies, f_o, and damping ratios were measured before any loading occurred and used as baseline data. The percentage decrease in frequency was determined by dividing each measured frequency, f_i, by this initial frequency. The

percentage of failure was taken as the cycle number divided by the total number of cycles

required for failure (Table 5.2). The damping ratio was determined using the measured

half-power bandwidth and Eq. (5.14) (Chopra 2003).

$$\zeta = \frac{f_b - f_a}{2f_l} \tag{5.14}$$

where: $f_b\text{-}f_a$ = half power bandwidth

f_l = first mode longitudinal frequency

A typically frequency plot is presented in Fig. 5.11. As displayed in Fig. 5.11,

there was little background noise due to the efficiency of the new instrumentation. This

figure also shows the location of f_l, f_b, and f_a, for use in Eqs. (5.13-5.14) From this plot,

both first mode longitudinal frequency and half-power bandwidth could be determined.

Measured frequencies were plotted against the percentage of failure. Fig. 5.12(a)

presents the general decrease of frequencies as a function of damage for all the concrete

mixes examined. Damping ratios were plotted against the percentage of failure (Fig.

5.12(b)). The individual mixes exhibit varying decreases in longitudinal frequency and

maximum damping ratios. These variations are presented in Tables 5.3 and 5.4.

Table 5.2. Example of Measurements for Frequency and Damping Ratio

Cycle #	% of Failure	f_l (kHz)	f_l/f_o	$f_b\text{-}f_a$ (Hz)	ζ
0	0.000	9.832	1.000	240	0.012
1	0.125	9.496	0.966	320	0.017
2	0.250	9.384	0.954	448	0.024
3	0.375	9.240	0.940	320	0.017
4	0.500	9.176	0.933	240	0.013
5	0.625	9.048	0.920	304	0.017
6	0.750	8.936	0.909	376	0.021
7	0.875	8.840	0.899	432	0.024
8	1.000	8.712	0.886	512	0.029
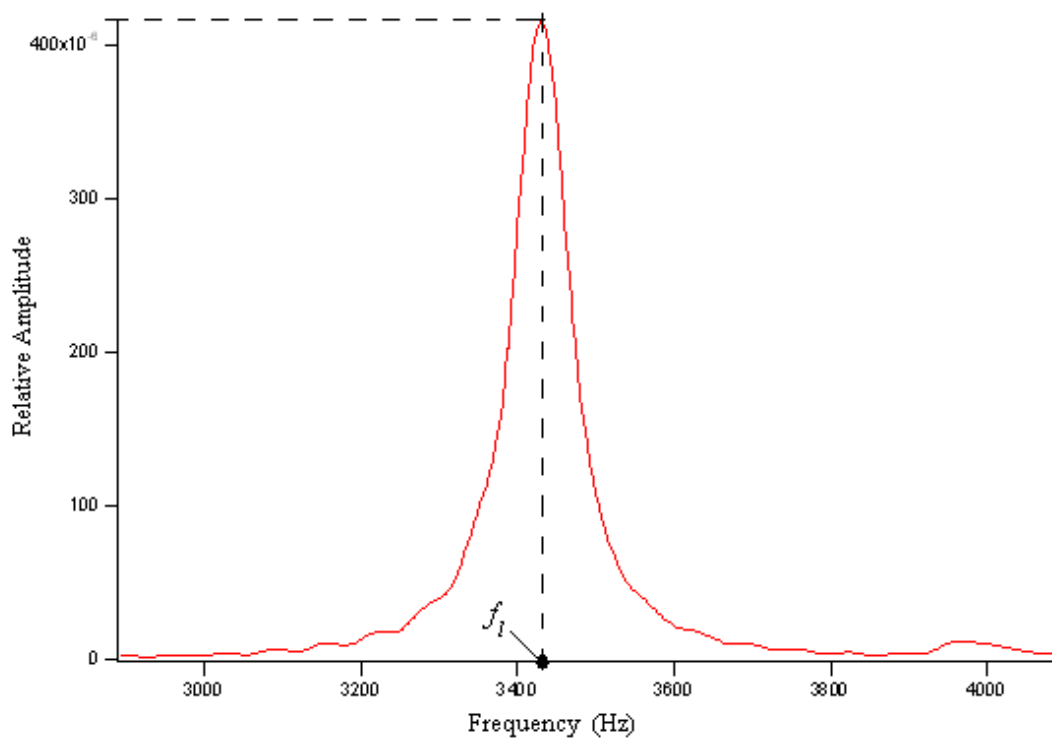
(a) Location of the first mode longitudinal frequency
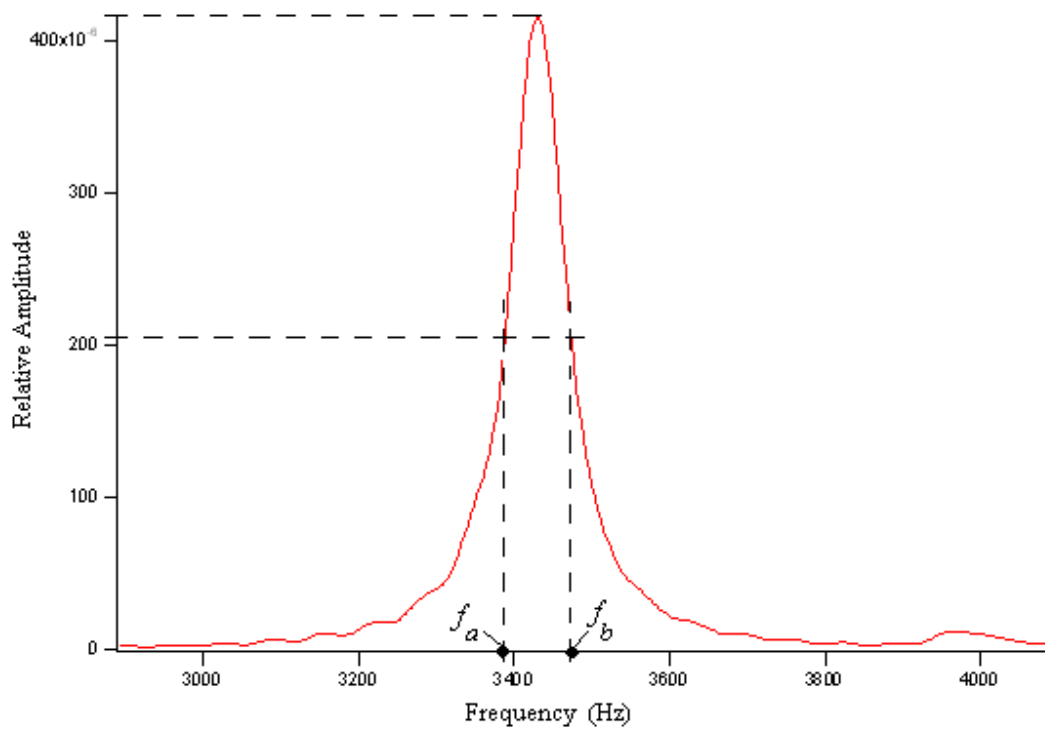
(b) Half power bandwidth
Fig. 5.11. Typical frequency plot

Examination of Figs. 5.12(a) leads to the conclusion that the longitudinal
frequency of a concrete cylinder decreases as a function of damage. This is because as
microcracks develop in the concrete specimens as a function of loading the stiffness of
the material deteriorates. As the specimens continued to be cyclically loaded, microcrack
growth continued, the concrete became more fatigued, and the longitudinal frequency
continued to decrease as demonstrated in Figs. 5.12(a). Eventually, the coalescence of
the microcracks reached a point at which the concrete specimen failed. Fig. 5.12(a)
demonstrates that the decrease in longitudinal frequency with damage appears to be a
function of the concrete strength. This fact is further demonstrated by the average
decrease in longitudinal frequency presented in Table 5.3. These decreases represent the
average amount of frequency loss measured on the 4 cylinders from each concrete mix at
the point of failure.
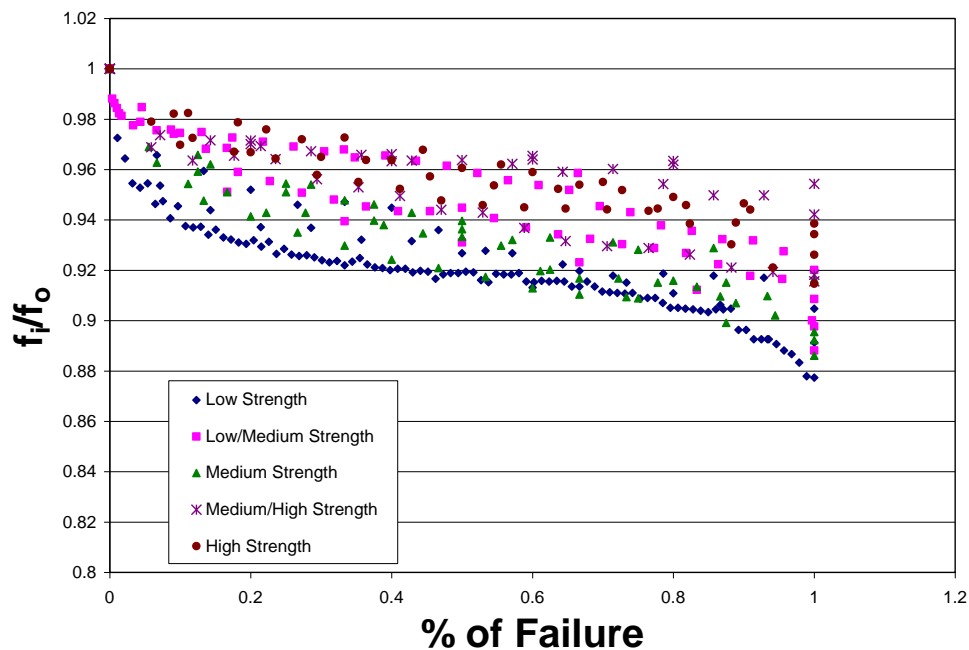
(a) First mode longitudinal frequency as a function of percentage failure
Fig. 5.12. Changes in dynamic stiffness properties due to damage
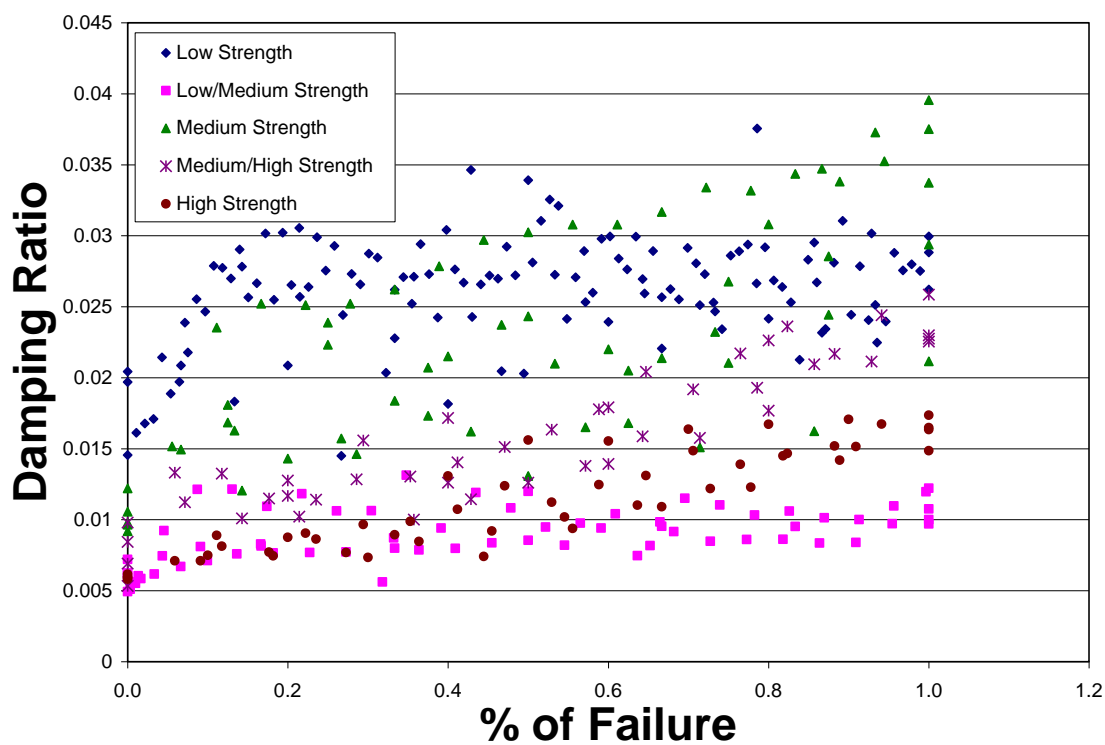
(b) Damping ratio as a function of percentage failure
Fig. 5.12. (continued)

Table 5.3. Final Frequency Divided by Initial Frequency

Mix	f_i/f_o
Low Strength	89.11%
Low/Medium Strength	90.36%
Medium Strength 1	90.13%
Medium / High Strength	93.26%
High Strength	92.84%

Table 5.4. Average Maximum Damping Ratio

Mix	Maximum Damping Ratio
Low Strength	0.028
Low/Medium Strength	0.011
Medium Strength 1	0.034
Medium / High Strength	0.024
High Strength	0.021

Although damping ratios demonstrate a general increase among all concretes sampled as a function of damage, the maximum ratios achieved are inconsistent between mixes (Table 5.4). The scatter of data among all concrete mixes presented in Fig. 5.12(b) further demonstrates this conclusion. Data from each concrete mix had correlation factors ranging from 0.11 to 0.84. Although the correlation factor of 0.84 indicates a good correlation within one concrete mix, the scatter of data among all concrete mixes follows no general trend and indicates that the damping ratio is not a good tool to quantify damage.

The amount of absorbed energy during each cycle was calculated from the hysteretic curves measured using the LVDT and extensometer instrumentation. A typical hysteretic curve is presented in Fig. 5.13. The hysteretic curve represents the amount of deflection that is measured per a specific load. By measuring the area within the curve, the amount of absorbed energy was calculated by determined (shaded area in Fig. 5.13). Fig. 5.14 presents the measured energy as a function of damage. The values for the total cumulative energy for each concrete mix are presented in Table 5.5.

As concrete strength increases, the total amount of energy absorption increases (Fig. 5.14). This effect demonstrates that higher strength concrete mixes have the ability to absorb more energy during cyclic fatigue (Table 5.5). This implies that as the bond between matrix material and aggregate increases due to increased concrete strength more energy is absorbed in modes other than the formation of microcracks.
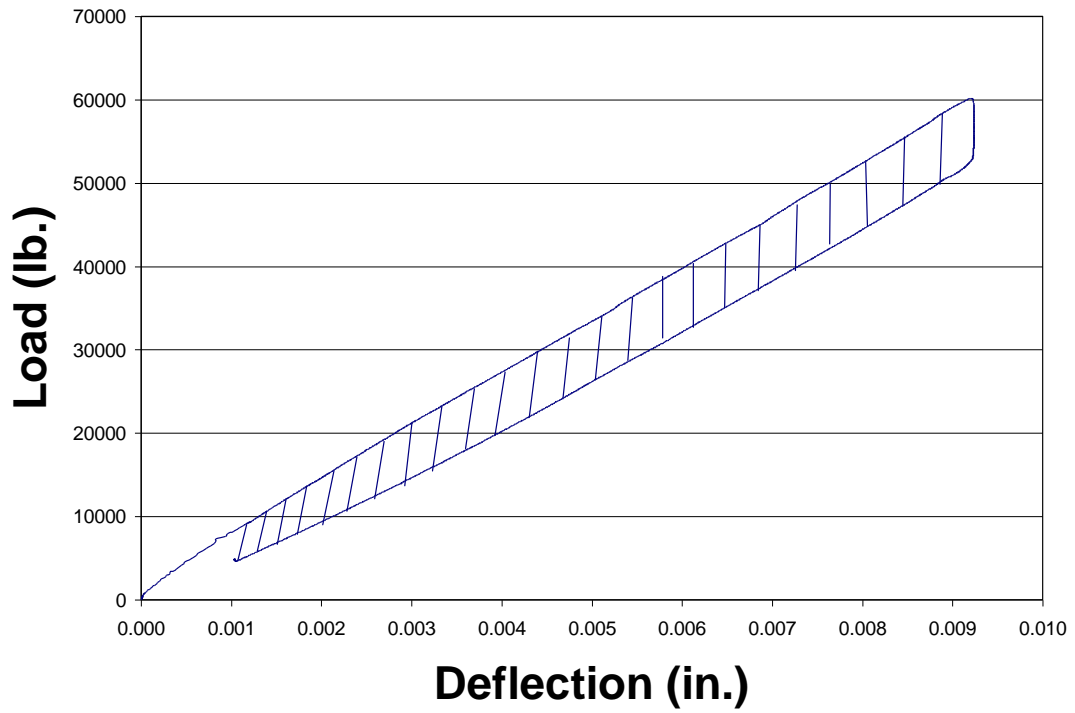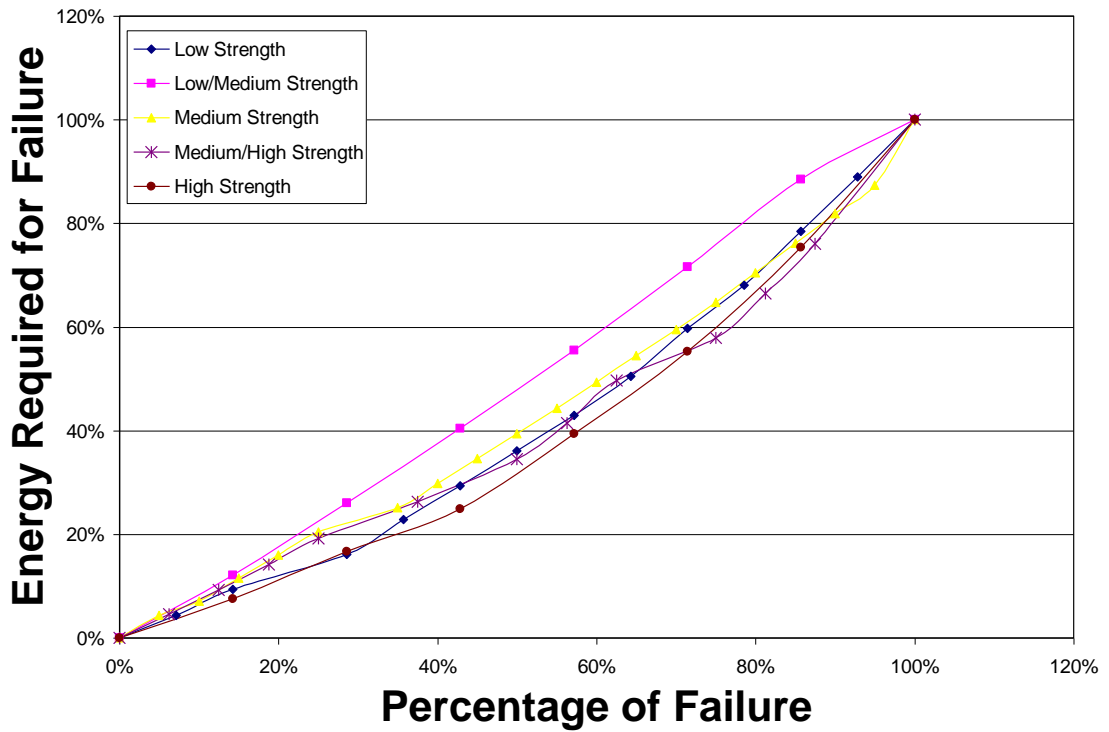
Fig. 5.13. Typical hysteretic curve

Fig. 5.14. Cumulative energy percentage required as a function of damage

Table 5.5. Average Values of Total Energy Increase per Concrete Strength

Mix	Average Total Cumulative Energy (ft.-lb.)
Low Strength	1262
Low/Medium	2318
Medium Strength 1	2925
Medium/High Strength	2684
High Strength	3528

Fig. 5.15 presents the total average percentage loss of initial frequency as a function of compressive strength. Each data point represents the average of the total loss measured from the four cylinders tested from each compressive strength class. Within each compressive strength class, total frequency loss differed by a maximum of 3.5%. When these values are plotted as a function of compressive strength, a correlation factor of 0.95 is determined. These results indicate that as microcracks develop and grow, the first mode longitudinal frequency decreases and is an excellent indicator of damage in concrete specimens as a function of strength.

Fig. 5.16 presents the total cumulative energy required to fail a concrete specimen of specific strength. With each ensuing cycle, more damage occurred to the cylinders. By measuring the total amount of energy absorbed during all cycles, the total amount of energy that can be absorbed by a specific strength concrete can be determined. Once, again, each data point represents the average cumulative energy absorbed from the measurements on the four cylinders from each strength class. The general trend indicates that as compressive strength increases, the total amount of energy required to fail a specimen increases. Within each compressive strength class, cumulative energy absorption differed by a maximum of 11%. When these values are plotted as a function of compressive strength, a correlation factor of 0.72 is determined.
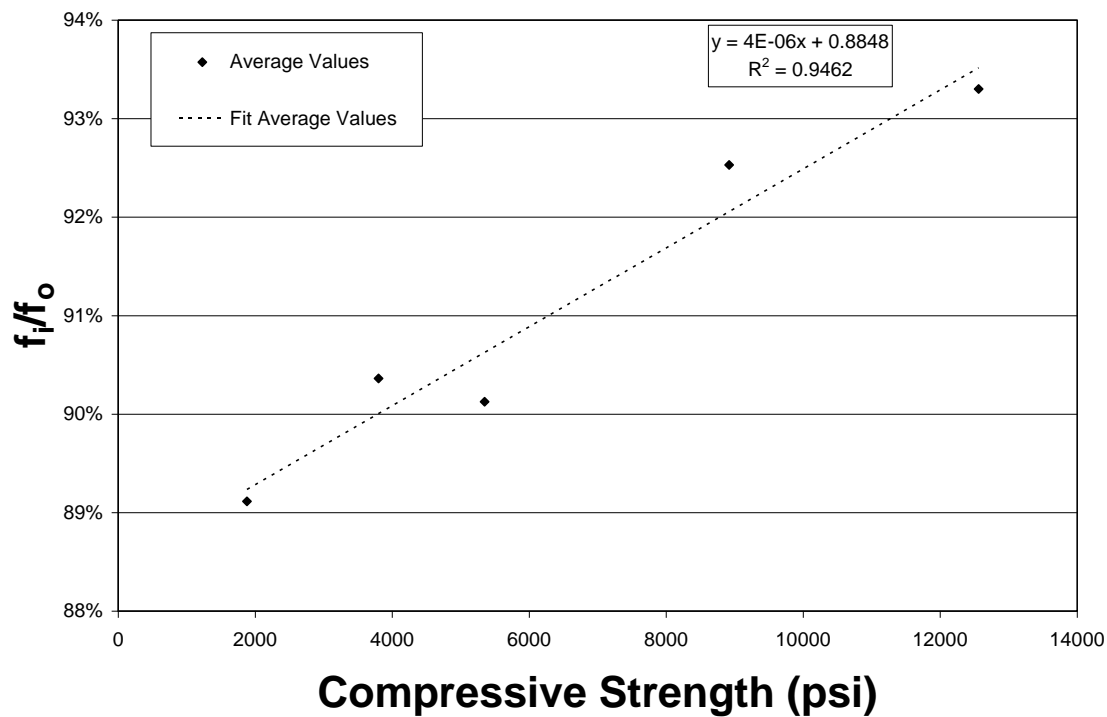
Fig. 5.15. Change in frequency response (f_i/f_o) as a function of compressive strength
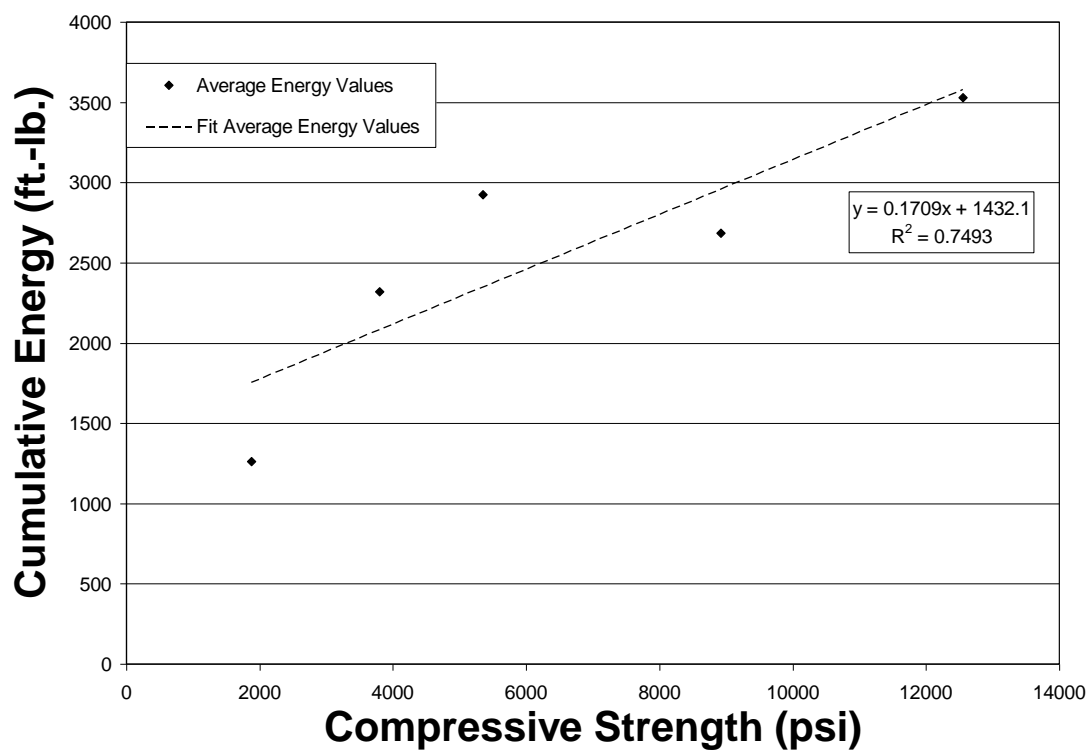
Fig. 5.16. Cumulative energy required for failure as a function of compressive strength

Finally, the amount of energy determined from each measured hysteretic curve is plotted as a function of percentage of failure (Fig. 5.17). The percentage of failure was calculated by dividing the number of cycles, N, by the total number of cycles required to fail a cylinder, N_f. This plot presents the determined energy from each cycle measured on all concrete specimens. The trend for data is logarithmic indicating it requires less damage to develop small values of damage. However, as indicated by the logarithmic trend of the data, higher amounts of energy causes more damage. With a correlation factor for all data of 0.95, this plot demonstrates the amount of energy absorbed by a concrete specimen is an excellent indicator of damage accumulation.
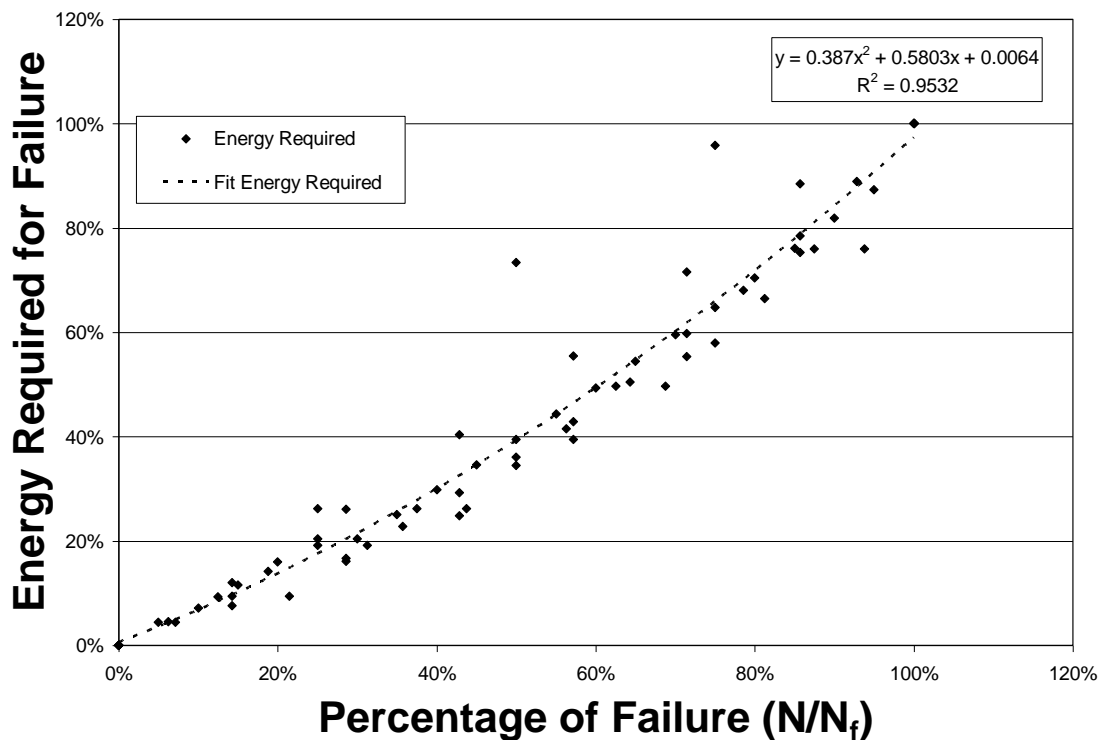
Fig. 5.17. Percentage of total cumulative energy as a function of percentage of failure

Proposed Damage Model

It was found that both measured frequency loss and absorbed energy were both excellent indicators of damage accumulation in concrete specimens. Thus, the results from the measured results of the two factors were combined to determine a proposed damage model.

Combining the results presented in Figs. 5.12 - 5.14, an indicator of damage can be developed based on compressive strength, energy, and frequency variation for concrete specimen. From the fitted trend line presented in Fig. 5.16, Eq. (5.15) is:

$$\frac{E_i}{E_f} = 0.387D^2 + 0.5803D + 0.0064 \tag{5.15}$$

where: E_i = energy measurement at cycle i

E_f = total cumulative energy required for failure of the specimen

D = percentage of damage

The fitted trend line in Fig. 5.16, Eq. (5.16) is:

$$E_f = 0.17f'_c + 1504 \tag{5.16}$$

where: f'_c = the compressive strength of the specimen

Finally, from the trend line presented in Fig. 5.15, Eq. (5.17) is:

$$\frac{f_i}{f_o} = 4 \times 10^{-6} f'_c + 0.89 \tag{5.17}$$

where: f_l = initial frequency

f_i = frequency measurement after cycle i.

Eq. (5.17) can be solved for f'_c (Eq. 5.18)):

$$f'_c = \frac{\left(\dfrac{f_i}{f_o}\right) - 0.89}{4 \times 10^{-6}} \qquad (5.18)$$

and by substituting Eq. (5.18) into Eq. (5.16), Eq. (5.19) is:

$$E_f = 45875\left[\left(\frac{f_i}{f_o}\right) - 0.8855\right] + 1282.6 \qquad (5.19)$$

Substituting Eq. 5.19 into Eq. (5.15), an equation to determine percentage damage of a concrete cylinder based on measured first mode longitudinal frequency and hysteretic energy is:

$$\frac{E_i}{45875\left[\left(\dfrac{f_i}{f_0}\right) - 0.8855\right] + 1282.6} - 0.0064 = 0.387D^2 + 0.5803D \qquad (5.20)$$

Finally, solving for damage, the proposed damage model is:

$$D = \frac{0.0075\left[\sqrt{E_i + 9685\left(\dfrac{f_i}{f_o} - 0.858\right)} - 99.90\sqrt{\dfrac{f_i}{f_o} - 0.858}\right]}{\sqrt{\dfrac{f_i}{f_o} - 0.858}} \qquad (5.21)$$

Using the proposed model and measured values of energy and frequencies, Fig.5.18 presents a precise comparison between the damage calculated using Eq. (5.21) and the cyclic failure ratio. A theoretical fit line is also presented in Fig. 5.18 and displayed along with other known indices of damage in Fig. 5.19. Values calculated with the proposed model correlate within 6.7% of measured values. Other studies present damage indices that generally increase as a function of percentage of failure, Miner's hypothesis is the most crude displaying only a linear increase. Gao and Hsu (1998) found that the trend was logarithmic, but found that at low percentages of failure,

the damage index was also relatively low. Finally, Suaris et al. (1990) found that there was initial jump in damage at low failure percentage and then a logarithmic increase at mid to high levels of failure percentage. Eq. (5.21) demonstrates a logarithmic trend and differs by a maximum 20%, 54%, and 12%, with Miner's hypothesis, Gao and Hsu (1998), and Suaris et al. (1990), respectively. Miner's hypothesis values differ from measured data by a maximum of 24% and an average of 17%. Values using the equation suggested by Gao and Hsu (1998) differ from measured data by a maximum of 47% and an average of 23%. Finally, values calculated using the equation suggested by Suaris et al. (1990) differ from measured values by a maximum of 13% and an average of 8%. Values calculated using Eq. (5.21) correlate with measured data within 7% indicating that the proposed method is more effective in predicting the amount of damage induced on cyclically loaded cylinders than the other models reviewed.
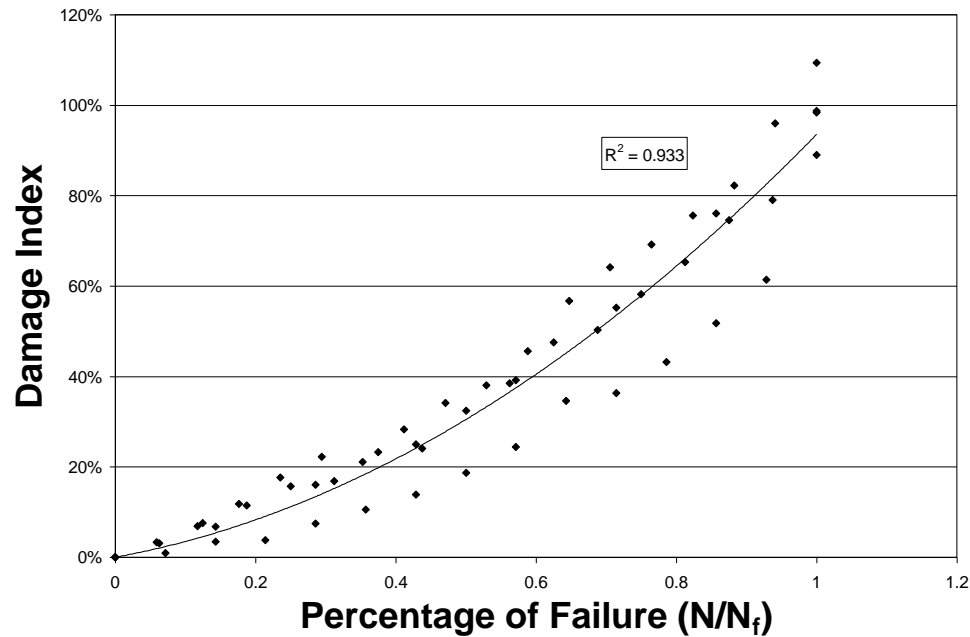
Fig. 5.18. Damage calculated by Eq. (5.21) as a function of the percentage of failure calculated from measured values
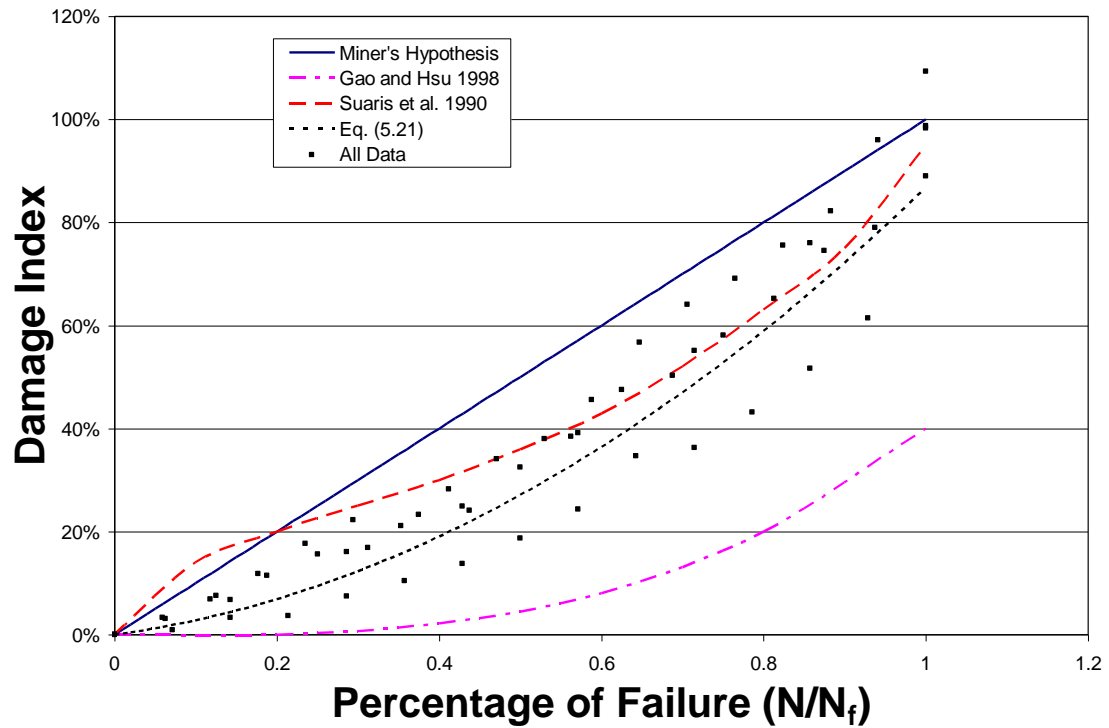
Fig. 5.19. Damage calculated from Eq. (5.21) compared to other known damage indices

Conclusions

Unconstrained compression waves were used in this study to determine the variation in first mode longitudinal frequency and damping ratio as a function of cyclic loading to failure. The amount of energy absorbed by individual concrete specimen was calculated from hysteretic curves measured during testing. Several concrete mixes were sampled to include a variety of compressive strengths. Results indicate that:

1.   First mode longitudinal frequencies were shown to decrease to a range of 88.5% to 93.3% of their initial, undamaged frequency. In general, higher strength concretes exhibited less percentage loss of initial frequency.

2. Damping ratio variation was shown to be inconsistent both among concrete types and percentage of failure and was determined to not be a precise indicator of damage.

3. Measurements of total cumulative energy were shown to correlate with percentages of failure within 4.7%. Also, higher strength concretes exhibited an ability to absorb more energy through modes other than the formation of microcracks.

4. A proposed damage model was created involving the use of compressive strength, frequency, and energy. This model was shown to correlate with measured values within 7%. This proposed model was shown to have a closer correlation than Miner's hypothesis and damage index models from other reviewed research.

5. Variation in first mode longitudinal frequency and total energy accumulation have been shown to be excellent indicators of damage in cyclically loaded concrete specimens of varying strength.

CHAPTER 6

A COMPARISON OF PRESTRESS LOSSES IN A PRESTRESSED CONCRETE

BRIDGE MADE WITH HIGH PERFORMANCE SELF-CONSOLIDATING

CONCRETE

Abstract

Many existing design procedures have been shown to miscalculate prestress losses in high strength, prestressed concrete bridge girders because they have been developed based on conventional strength concrete. This study describes the measured behavior of six, high strength, self-consolidating concrete, prestressed bridge girders. Measured strains were used to determine prestress losses that were compared to calculated values obtained using the 2004 and 2007 AASHTO LRFD Specifications. The prestress losses calculated using the AASHTO design practices underestimated the measured elastic shortening losses and overestimated the total long term losses measured. This study shows that design practices for high strength concrete are improving, and that these procedures adequately predict the long-term prestress losses for high strength self-consolidating concrete.

Introduction

High-performance concrete (HPC) is a unique type of concrete that provides superior physical properties such as increased strength for specific applications like prestressed concrete bridge girders. A specific type of HPC investigated during this research is self-consolidating concrete (SCC). SCC is a relatively new type of concrete characterized by its ability to consolidate completely under its own weight. This type of

concrete can be used to increase production quality and efficiency while reducing labor

costs because of its ability to consolidate without the need for external vibration. This

allows for quality placements of SCC without the need for large labor crews. These

enhanced concrete characteristics are achieved by a stringent mix design that produces

the fundamental rheological properties of SCC. By definition, rheology is the study of

the deformation and flow of matter under the influence of an applied stress. In the case

of SCC, the applied stress is simply the self weight of the material and the fundamental

rheological properties required to obtain this flow are based on a low yield stress,

moderate viscosity, and retention of the kinetic energy of the flowable mix by the

reduction of the volume of coarse aggregate (Bonen and Shah 2004). SCC is discussed in

detail in Chapter 4 of this document.

SCC has been shown to increase in strength relatively quickly within its first few

days of curing (Khayat et al. 2000). Because of this rapid increase in compressive

strength, prestressed concrete girders can be removed from the formwork and

prestressing strands can be released as early as one day. Bridges that incorporate the use

of high performance SCC (HPSCC) girders can be fabricated with longer spans, fewer

girders, and more clearance. It is anticipated that by using HPSCC, prestressed concrete

bridges can be produced for a smaller cost than those using conventional, normal-strength

concrete.

Although the benefits of using HPSCC are somewhat apparent, few bridge girders

are in place that utilize the material. There are two main reasons for this lack of use. The

first is the stringent mix design that is required. The second is that a majority of the work

done with SCC has been focused in the conventional strength ranges, whereas long span,

prestressed girders typically require higher-strength concrete. This research presents the measured behavior of a prestressed concrete girder bridge where the fabricator was able to produce a high strength SCC that was used for each of the bridge girders.

Previous Research

The measurement and prediction of prestress losses in HPC prestressed bridge girders is highly documented in literature. Kukay et al. (2007) presented a comparison of time dependent prestress losses in a two-span, prestressed concrete bridge. The four bridge girders studied in this investigation were made of HPSCC and were instrumented with vibrating wire strain gages with integral thermistors. The study compared values of prestress loss calculated from measured strain to predictive values found using the NCHRP 18-07 method. The study found that there was a relatively low percentage (11.5% of the jacking stress) of total measured prestress loss. This smaller than expected loss was due to a significantly higher actual concrete strength than was required by design. Using the NCHRP design procedures, the study also found that when actual concrete strengths were used the predicted values of prestress losses corresponded closely with the measured values up through deck casting. After deck casting, the predicted values of total loss were found to be un-conservative when actual compressive strengths were used in the calculations.

Barr et al. (2007) instrumented and monitored five precast, prestress girder made with HPC. These girders were monitored for prestress losses for three years after the time of casting. The observed values of prestress losses were compared with values calculated using the AASHTO LRFD specifications (2004) and the methods based on the

results of NCHRP 18-07 (Tadros et al. 2003). The study found that by using a calibrated modulus of elasticity, total losses calculated using the NCHRP method were within 10% of the measured total losses. However, this calibrated modulus resulted in the AASHTO calculated values being 30% higher than the total measured losses. The study found that, on average, the observed elastic shortening losses were found to be 21% higher than those calculated using AASHTO and 11% lower than those calculated using the NCHRP method. The difference between the measured and predicted losses was reduced to within 3% difference when the calibrated modulus was used.

Kowalsky et al. (2001) instrumented and measured prestress losses in several HPC bridge girders in North Carolina. The researchers found shrinkage losses were a small component of the overall prestress losses and that the elastic shortening and creep losses were the major contributors. These larger than expected losses from elastic shortening and creep were attributed to an actual modulus of elasticity that was lower than predicted. The total prestress losses ranged from 12.9% to 19.1% of the initial jacking stress.

Yang and Myers (2005) instrumented four HPC prestressed bridge girders in Missouri with a total of 16 internal thermocouples, 64 VWSGs, and 14 internal bonded electrical resistance strain gages (ERSG). The researchers incorporated eight commonly used loss estimate models for calculating total prestress losses, including the AASHTO, Prestressed Concrete Institute (PCI), and NCHRP methods. They reported total measured average losses of 20.7% of the initial jacking stress with elastic shortening accounting for the largest portion of the total loss. Also, they concluded that for prestress precast HPC girders, the PCI handbook method, the method recommended by Gross

(1999), and the NCHRP method to be optimal for prestress losses estimation in the design.

Ahlborn et al. (1995) tested two full-size composite I-girders fabricated with HPC. Two different mix designs were used for these girders, which had a span length of 133 feet. Prestress losses predicted by incorporating measured material properties into the PCI general time step approach were 5 to 10 percent larger than measured in the instrumented girders.

Roller et al. (1995) fabricated and tested four prestressed high strength concrete bulb-tee girders. They found that the AASHTO 1989 LRFD Specifications provisions for calculating creep and shrinkage prestress losses may be overly conservative for high strength concrete. In their study, measured prestress losses were significantly less than the total long-term prestress losses predicted using the provisions in the AASHTO LRFD 1989 Specifications. They also found that measured creep and shrinkage deformations of cylinders representing the concrete in the instrumented girders were consistent with the finding regarding the measured prestress loss. Their study concluded that high strength bridge girders could be expected to perform adequately over the long-term when designed and fabricated in accordance with the 1989 AASHTO LRFD 1989 Specifications. However, the measured prestress losses in one of the girders instrumented was 50% less than the expected value indicating that the AASHTO LRFD 1989 Specifications were grossly conservative.

Additional literature regarding prestress losses in prestressed HPC bridge girders can be found in Cole (2000), Tadros et al. (2003), Stallings et al. (2003), and Gilbertson and Ahlborn (2004).

Legacy Parkway Bridge 669

State Street Bridge 669 of the Legacy Parkway in Farmington, Utah was designed by UDOT engineers as a precast, prestressed three-span bridge. The bridge was designed as simply supported for girder and deck self weight and three-span continuous for live load and superimposed dead weight. The first, second, and third spans are 132.2 ft., 108.5 ft., and 82.2 ft., respectively. The bridge had a width of 76.3 ft. and a skew of approximately 25°. Fig. 6.1 presents a typical elevation and cross sectional view of Bridge 669.

Eleven AASHTO Type VI precast, prestressed girders spaced at 6.9 ft. on center were used to support the 8 in. thick composite bridge deck for each span (Fig. 6.2(a)). Each girder contained 0.5 in. diameter low relaxation prestressing strands harped at 0.4 times the span length for each girder. The concrete strengths and number of prestressing strands for each girder were designed based on an HL-93 loading per AASHTO LRFD 2004 Bridge Design Specifications. Using these design criteria the first, second, and third spans were required to have 66, 39, and 26 strands in each girder, respectively (Fig. 6.2(b)). The specified compressive strength for all girders was 6.5 ksi and 7.5 ksi at release of the prestressing strands and 28 days, respectively. The 28 day design compressive strength specified for the composite deck concrete was 4 ksi.

The girders were placed in steel formwork and set to cure for 1 day before the formwork was removed and the prestress was transferred. There was no external heat or steam applied to the girders during curing. However, due to the low ambient temperatures, steam was released as the formwork was removed (Fig. 6.3).
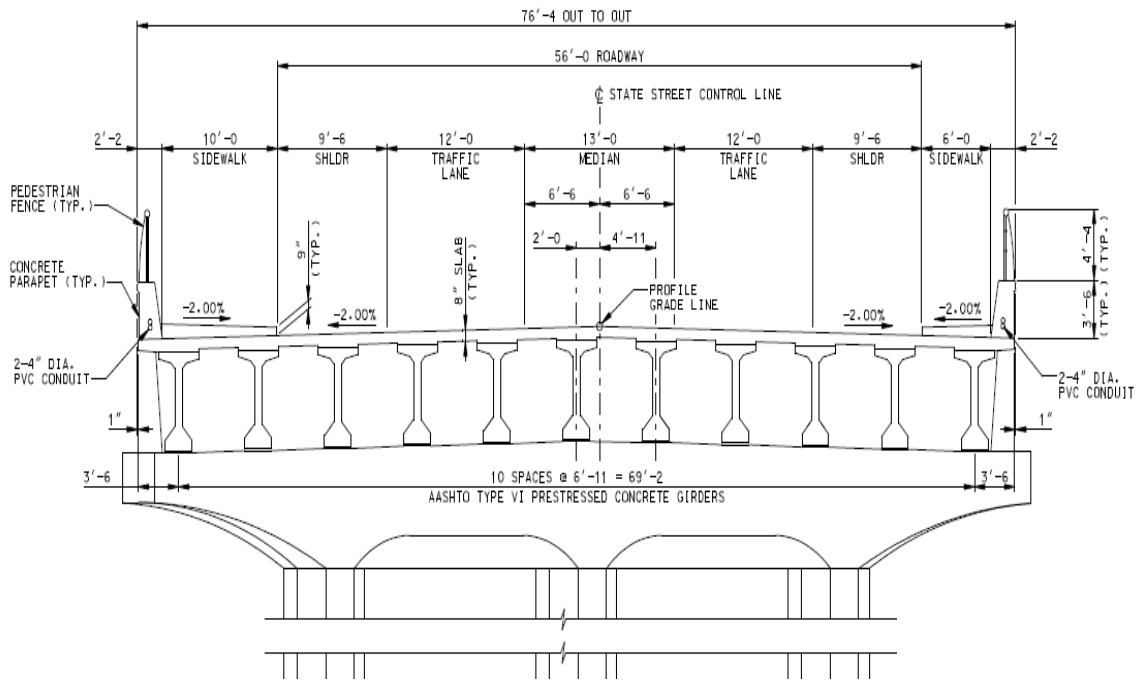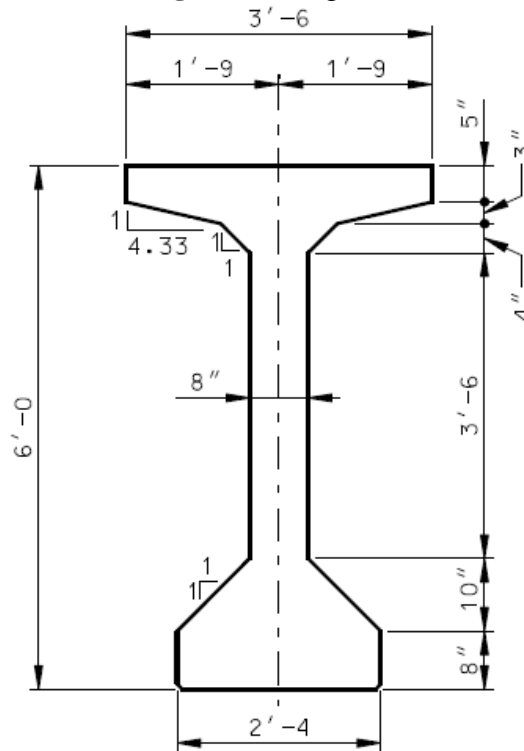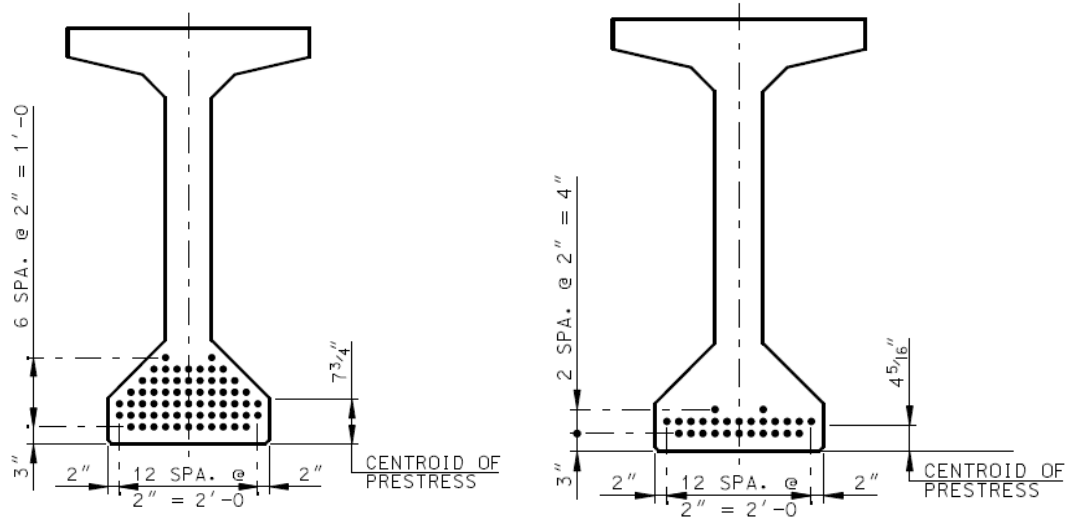
(a) Elevation view
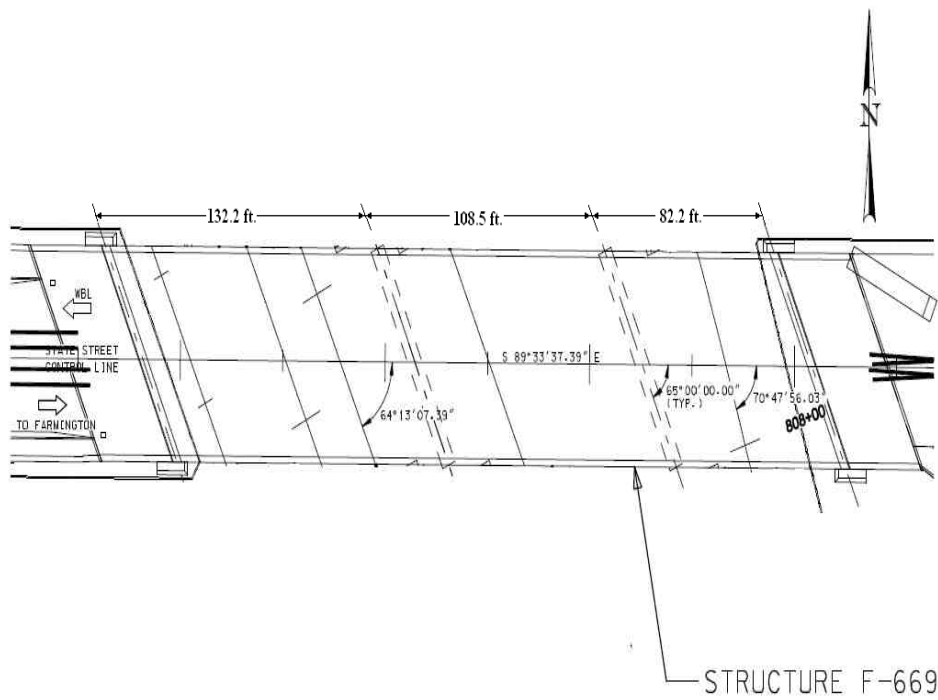
(b) Plan view

Fig. 6.1. Bridge 669

(a) Typical AASHTO type VI girder

(b) Design of prestressing strands for first and third spans, respectively
Fig. 6.2. Bridge 669 girders

(c) Girders in place before placement of composite concrete deck
Fig. 6.2. (continued)

Fig. 6.3. Girders were cured in steel forms with no external steam

Although the specified strengths of the girder concrete were relatively low, the fabricator elected to use a HPSCC mix design in part to reduce labor costs. As a result, the average compressive strengths at release and at 28 days were 8.4 ksi and 12.8 ksi, respectively. The average 28 day compressive strength of the composite deck concrete was 5.8 ksi. The composite deck was cast between approximately 2 and 5 months after the fabrication of the third and first spans, respectively.

Instrumentation and Monitoring
Program

A total of 24 vibrating wire strain gages (VWSG) with integral thermistors were installed at midspan in the first and third spans of Bridge 669. Three girders from each span were instrumented with two VWSGs at the centroid of the prestressing strands and two VWSGs in the web of the girder. The centroid of the prestressing strands was 7.75 in. and 4.31 in. from the bottom of the girder for the 132 ft. and 82 ft. spans, respectively. The two VWSGs embedded in the web of the girder were installed at 29 in. and 59 in., respectively from the bottom of the girder (Fig. 6.4). These gages were embedded to obtain strain and temperature readings over the height of the section throughout time (Fig. 6.5). The gages measured variations in strain and temperature for approximately 10 months and 7 months for the first and third spans, respectively, beginning at the time of casting. During destressing the gages were monitored every minute. During curing and placement the reading interval increased to fifteen minutes.

The large increase in strain at day 0 is due to elastic shortening and is caused by the transfer of prestress to the concrete girder when the prestressing strands are cut. The change in strain displayed at days 156 and 73 for the 132 ft. and 82 girders, respectively,

is due to the deck placement. Strain gages in the top of the web experience an increase in strain during deck casting due to their position relative to the centroid of the composite section. Strain gages in the bottom of the web are closer to this centroid and thus see a smaller variation. The strain gages located at the strand centroid experience an increase in strain due to the deck placement. The gap in the data for both spans between transfer of prestress and deck casting was during transportation of the girders to the bridge site. At this time, the instrumentation was disconnected and no readings were recorded. The small change in strain shown directly after deck placement is due to the addition of super imposed dead load due to sidewalks and traffic barriers. The larger amount of prestress force and subsequent losses in the 132 ft. girder cause the strains measured and presented in Fig. 6.5(a) larger than those for the 82 ft. girder (Fig. 6.5(b)).

Figs. 6.6 – 6.7 present the changes in temperature as a function of time for both the 132 ft. and 82 ft. spans, respectively. Each figure presents both the long term temperature readings (a) and temperature readings made during the first days of curing (b). During the first few days of curing the highest temperatures are achieved for both spans. As time progresses, the temperatures decrease as the initial curing temperature due to the hydration of the cement cease and ambient temperatures begin to control the temperature of the girder. The high temperatures due to the heat of hydration can be seen in Figs. 6.6(b) and 6.7(b). Temperatures during this phase of curing reach nearly 160° for both spans. It can also be noticed from these figures that the temperatures reached are higher in the web than in the flange. This is contrary to what might be expected. There is more concrete volume in the flange and the hydration should be more complete in this area of the girder than in the web.
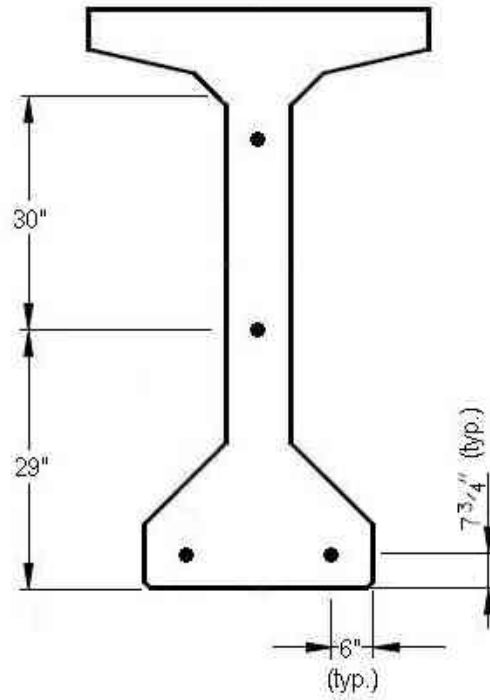
132 ft. girder
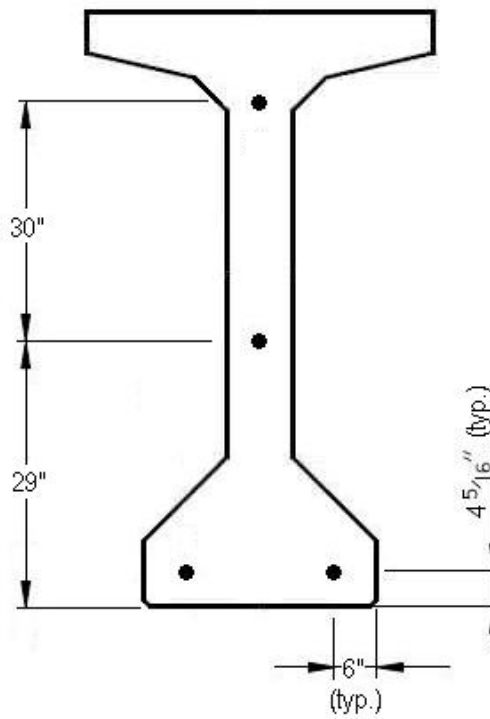
(b) 82 ft. girder

Fig. 6.4. Location of embedded VWSGs
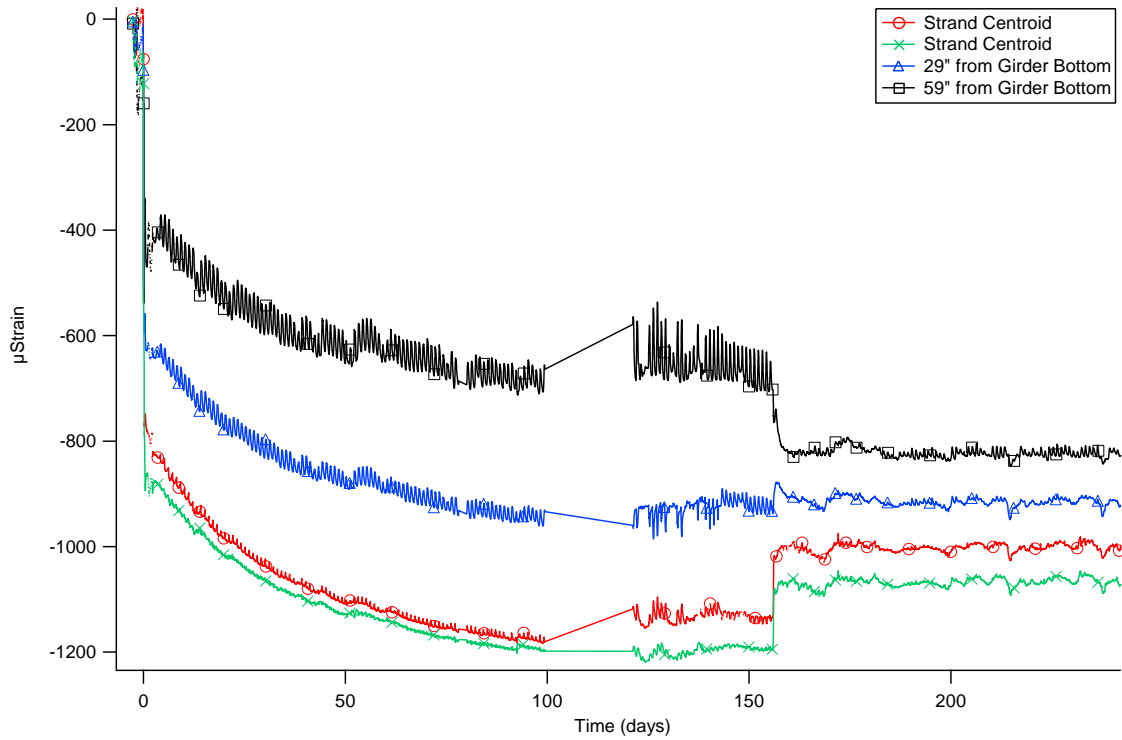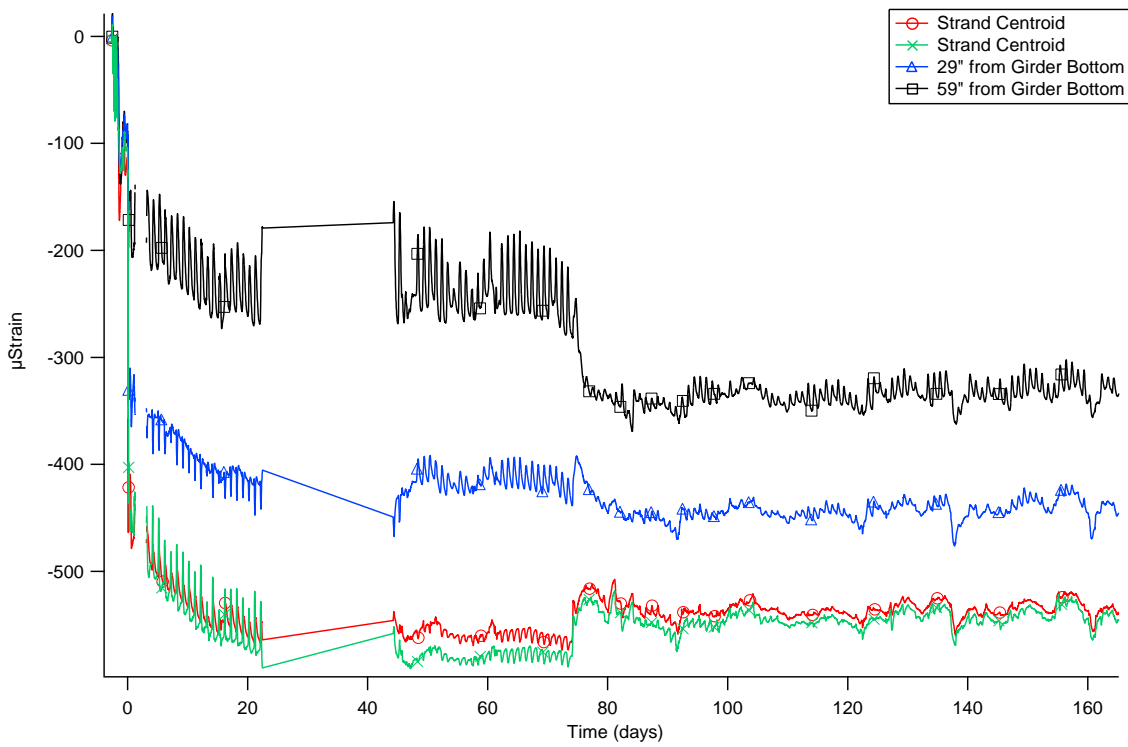
(a) 132 ft. girder

(b) 82 ft. girder

Fig. 6.5. Measured strains
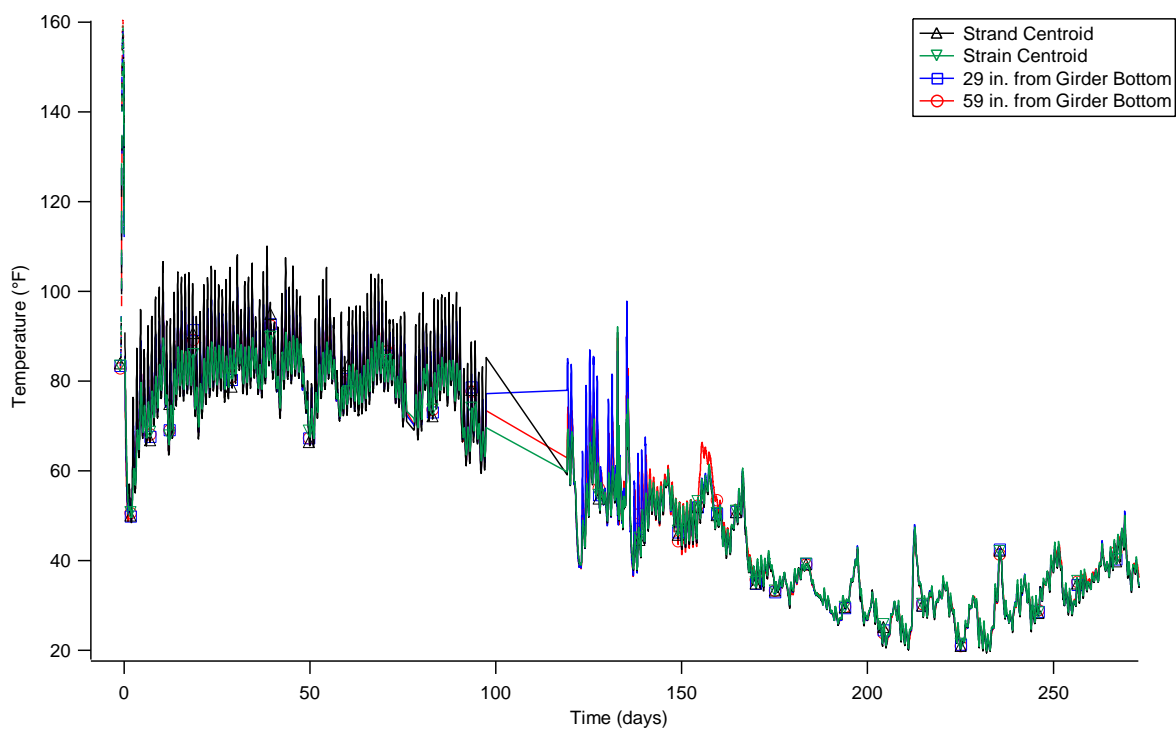
(a) Long term temperature readings
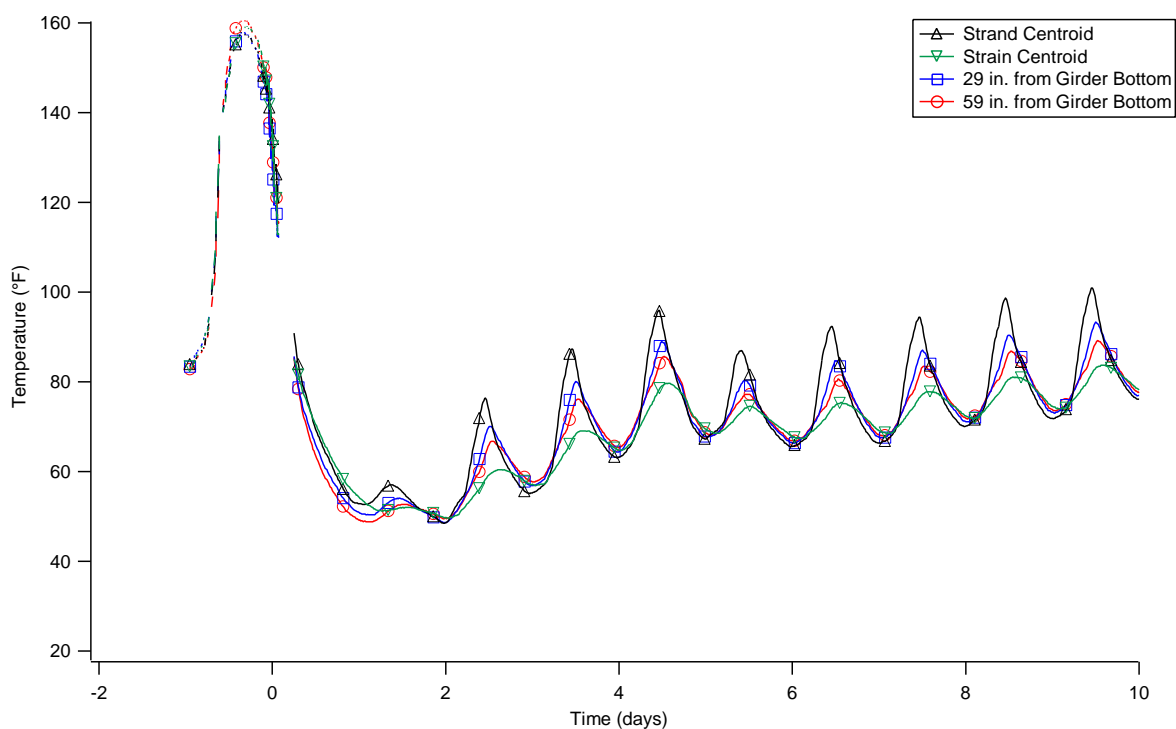
(b) Short term temperature readings

Fig. 6.6. Temperature readings measured on the 132 ft. girders
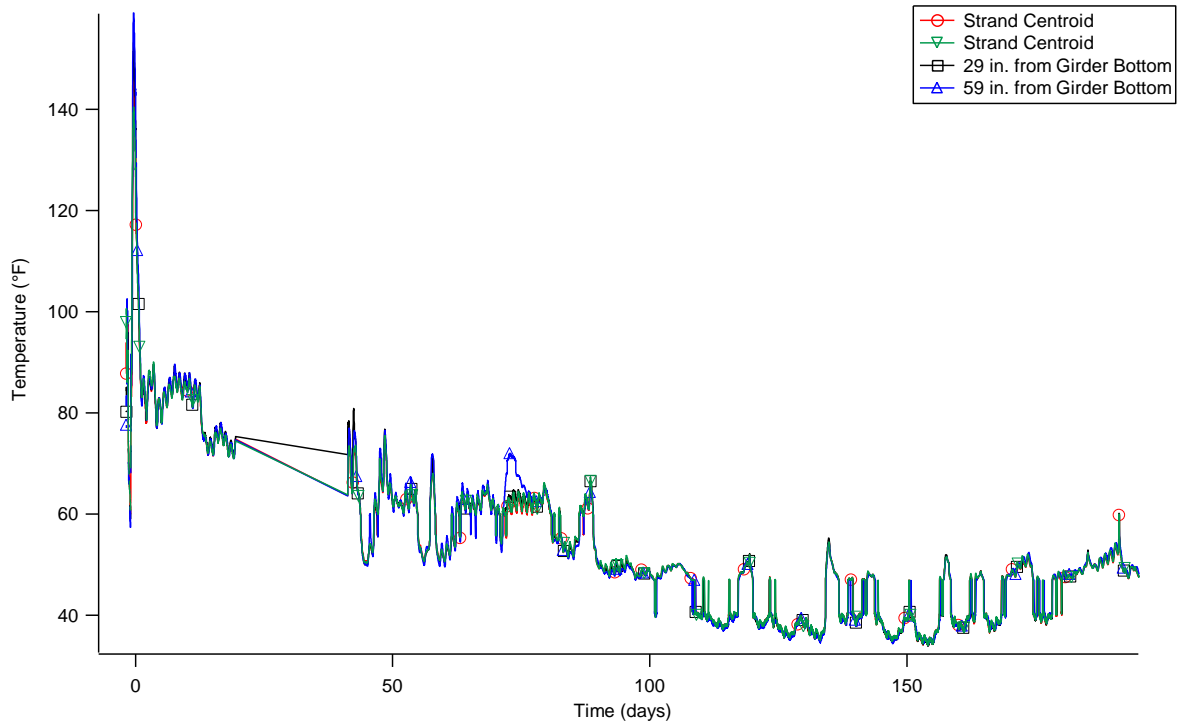
(a) Long term temperature readings
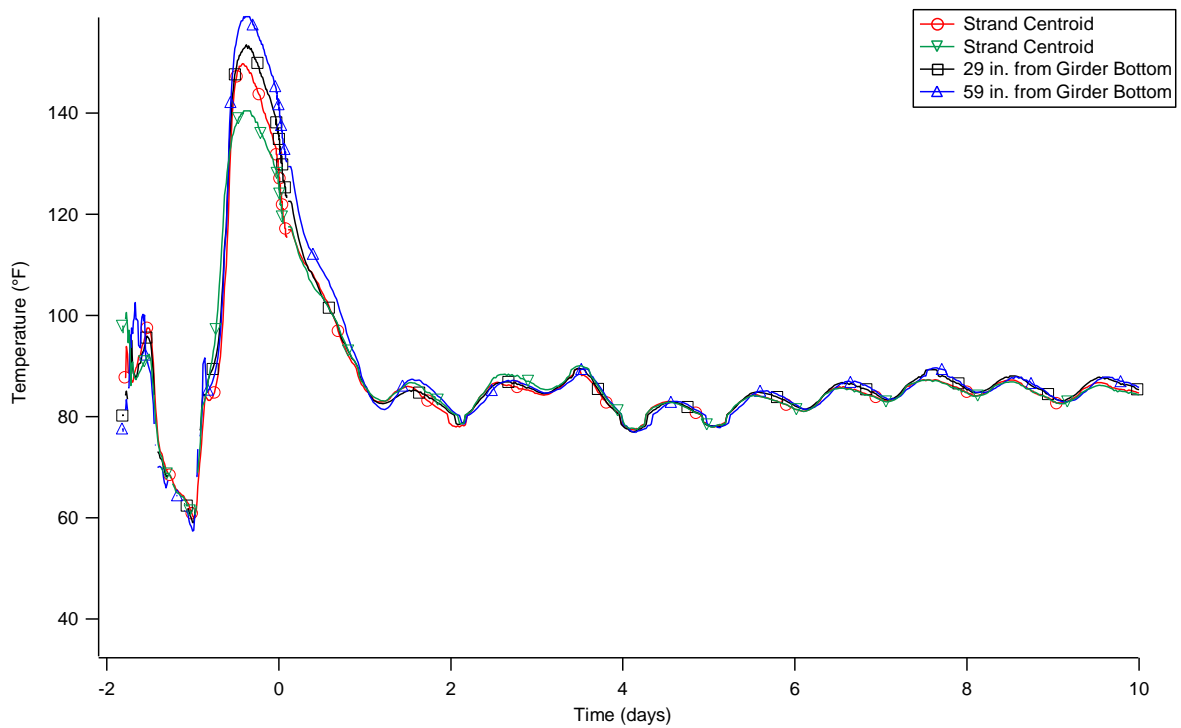
(b) Short term temperature readings

Fig. 6.7. Temperature readings measured on the 82 ft. girders

Material Properties

The HPSCC used to fabricate the girders provided a strength and stiffness above that of conventional HPC. A representative concrete sample was taken from a front delivery concrete truck during the casting of a typical AASHTO Type VI girder. The material was sampled and specimens were made in accordance with ASTM C31 (2003), Standard Practice for Making and Curing Concrete Test Specimens in the Field. Concrete specimens included a variety of 4 in. x 8 in. and 6 in. x 12 in. cylinders and 3 in. x 17 in. beams. The 4 in. x 8 in. specimens were typically used for compressive strength measurements, while the 6 in. x 12 in. cylinders were typically used for static Young's modulus measurements. The beams were used to measure drying shrinkage.

Compressive strength and static Young's modulus measurements are presented in Table 6.1. The American Concrete Institute (ACI) committee 209 suggests Eq. (6.1) to calculate compressive strength as a function of time for moist cured concrete.

$$f_{cm} = f_{c28}\left(\frac{t}{4 + 0.85t}\right) \tag{6.1}$$

where: f_{cm} = mean compressive strength at age t days

f_{c28} = mean 28-day compressive strength

t = time in days

Compressive strength values calculated using Eq. (6.1) are presented with measured values in Fig. 6.8.

Equations suggested by ACI committee 318 (Eq. (6.2)) and the Prestressed Concrete Institute (PCI) (Eq. (6.3)) are presented along with measured values in Fig. 6.9.

$$E_s = 33000 w_c^{1.5} \sqrt{f_c'} \qquad (6.2)$$

$$E_s = \left(40000\sqrt{f_c'} + 1000000\right)\left(\frac{w_c}{145}\right)^{1.5} \qquad (6.3)$$

where: E_s = static Young's modulus of elasticity

w_c = weight of concrete

f_c' = compressive strength of concrete

Measurements of shrinkage are presented in Fig. 6.10 along with values

calculated using Eq. (6.4) recommended by AASHTO LRFD 2004 Specifications for

moist cured concrete.

$$\varepsilon_{sh} = k_s k_h \left(\frac{t}{35+t}\right) 0.51 \times 10^{-3} \qquad (6.4)$$

where: ε_{sh} = strain due to shrinkage

k_s = size factor

k_h = humidity factor

t = drying time.

Values calculated for the estimated compressive strength using Eq. (6.1) were

approximately 31.7% smaller than the measured values at day 1. This under estimation

was reduced as a function of time and by day 56 the measured and calculated values

correlated within 1%. This characteristic confirms previous findings that HPSCC

exhibits higher strengths at early ages. This property of HPSCC makes it ideal for

prestressed bridge girders due to the quick fabrication requirement.

Values of static Young's modulus calculated with Eq. (6.2) varied from

approximately 29% smaller to 21% larger than the measured values on days 1 and 56,

respectively. However, values of static Young's modulus calculated using Eq. (6.3) were

approximately 27% smaller at day 1, but within a 2% correlation on days 7, 28, and 56.

This indicates that Eq. (6.3) is more appropriate for calculations of static Young's

modulus than Eq. (6.2) for this specific concrete due to the concrete's high compressive

strength. HPSCC exhibits above normal properties at young ages making it ideal for

prestressed bridge girders. This comparison also shows that equations for high

performance concrete can adequately be applied to HPSCC.

The shrinkage strains calculated using Eq. (6.4) were approximately 40% smaller

than the average measured value at day 7 and 11% at day 56, respectively. Values

presented in Fig. 6.10 exhibit that the shrinkage strain characteristics of SCC are

adequately predicted by Eq. 6.4.

Table 6.1. Compressive Strength Measurements, Static Young's Modulus Measurements

Days after Casting	Load (lb.)	E_s (psi)	f'c (psi)
1	106209	4.09E+06	8452
1	103699	4.33E+06	8252
3	130759	4.58E+06	10405
3	126313	4.63E+06	10052
7	135282	4.71E+06	10765
7	147390	4.84E+06	11729
14	149990	4.65E+06	11936
14	154171	5.03E+06	12269
28	160736	5.60E+06	12791
28	161867	5.42E+06	12881
56	180397	5.63E+06	14356
56	164793	5.71E+06	13114
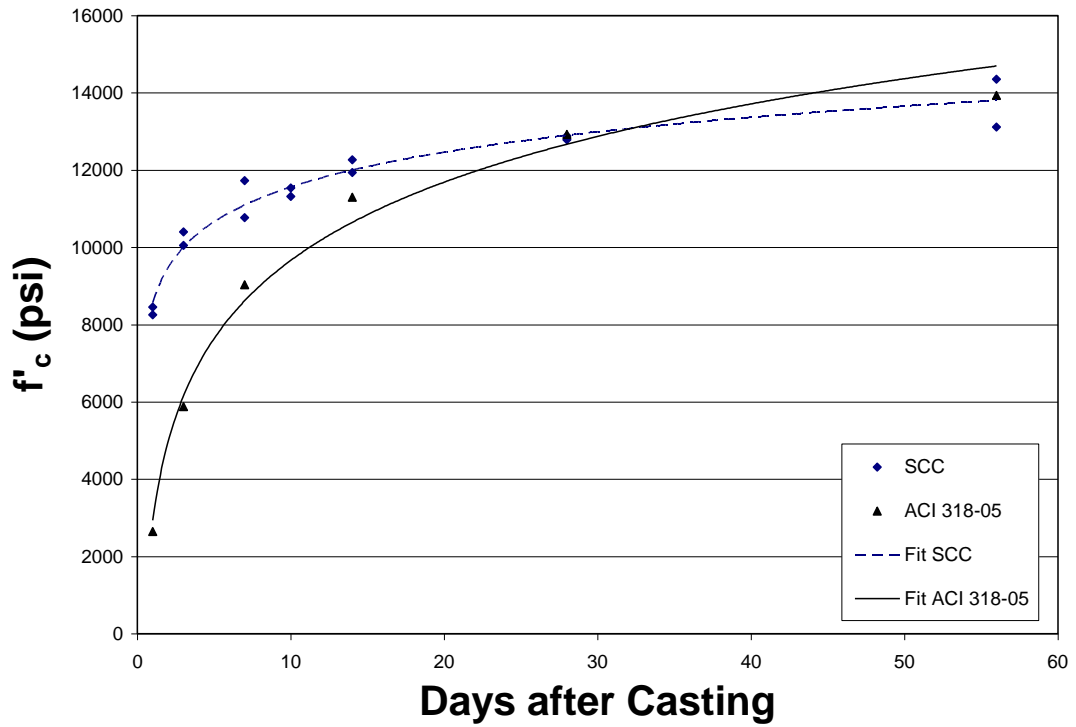
Fig. 6.8. Measured and calculated compressive strength values
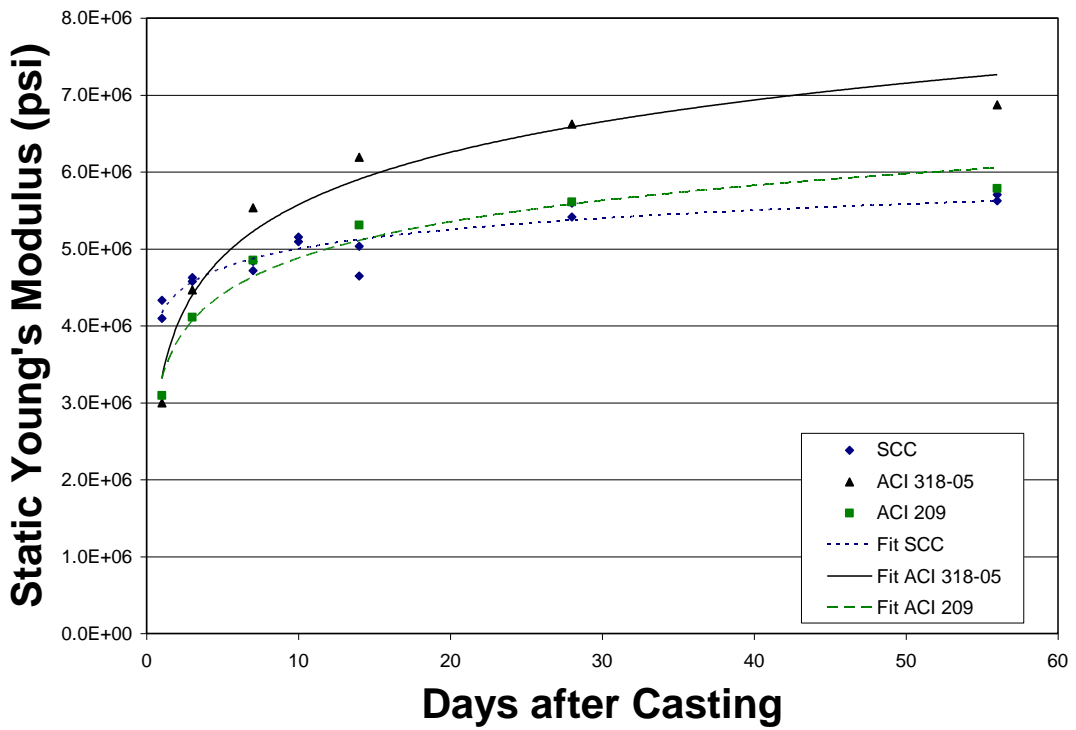
Fig. 6.9. Measured and calculated static Young's modulus values
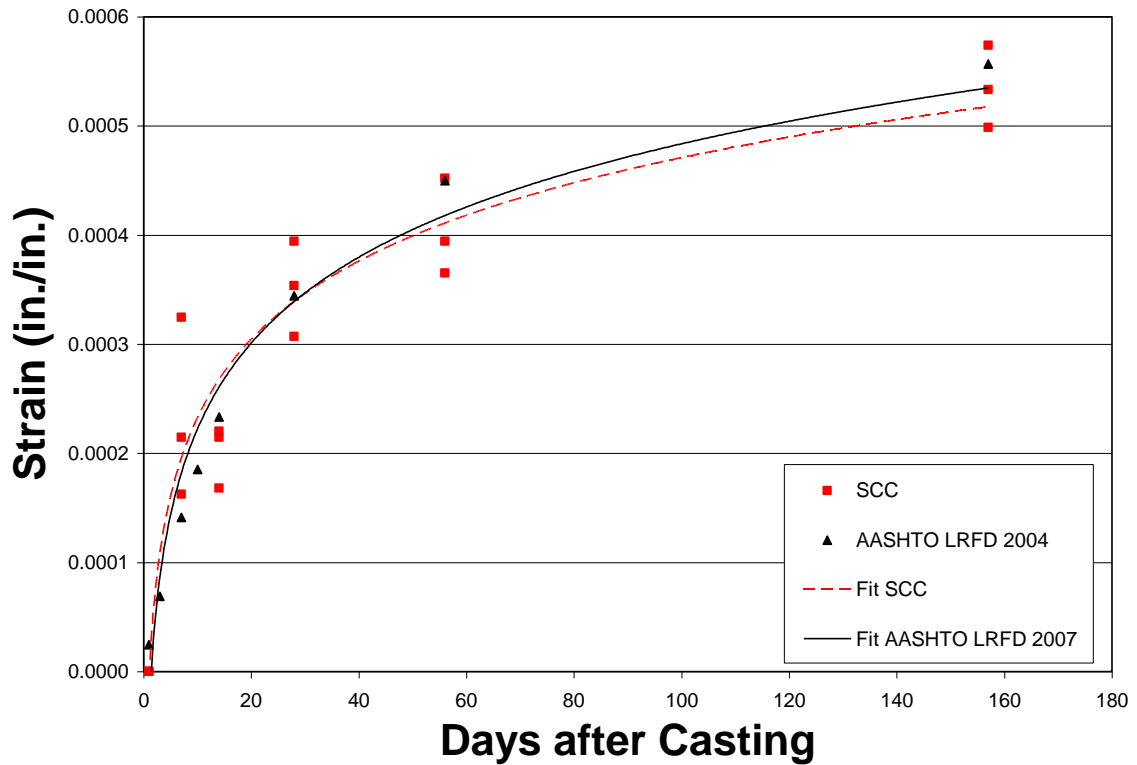
Fig. 6.10. Measured and calculated shrinkage values

Total Prestress Loss

The prestressing force in a girder is lower during its service life than at initial

stressing. This loss of prestress over time is due to relaxation of the prestressing steel,

elastic shortening of the concrete when the prestress force is applied, creep and shrinkage

of the girder, and depending on the support conditions, differential shrinkage of the deck.

In addition to the reduction in stress, some stress is regained with the addition of external

loads caused by superimposed loads such as the cast in place deck, concrete barriers, or

sidewalks. The total prestress losses must accurately be estimated during the design of

the girder so that, when subtracted from the initial jacking stress, there is sufficient

remaining prestress force to provide the necessary concrete stress during service.

Changes in stress due to elastic shortening, creep and shrinkage of the girder concrete,

differential shrinkage of the deck, and the effects of the self weight of the deck and sidewalks were monitored for this research. The relaxation of the prestressing steel is relatively small and was not directly measured. AASHTO 2004 designates losses due to relaxation as 1.2 ksi before and after transfer. AASHTO LRFD 2007 Specifications define the loss due to relaxation as approximately 2.0-4.0 ksi.

The strain measured by the VWSGs located at the centroid of the prestressing strands in each girder can be used to calculate the change in prestress (Eq. (6.5)).

$$\Delta f_{pT} = E_p \Delta \varepsilon_c \tag{6.5}$$

where: Δf_{pT} = the change in steel stress due to total prestress loss

E_p = modulus of elasticity of the prestressing steel (28,500 ksi)

$\Delta \varepsilon_c$ = measured change in strand strain

Eq. (6.5) was used with the strains measured at the centroid of the prestressing strands to calculate the total prestress losses for each of the instrumented girders. Figs. 6.11 – 6.12 present the measured prestress losses for the 132 ft. span and 82 ft. span instrumented girders, respectively.

The average measured long-term prestress losses at the last day of readings were 29.8 ksi and 16.1 ksi corresponding to approximately 14.7% and 8.0% of the initial jacking stress (202.5 ksi) for the 132 ft. and 82 ft. girders, respectively. The 82 ft. girders experienced smaller losses due to the smaller prestress force requirements. Each girder experienced a high rate of stress loss initially, but the rate of loss diminished as both a function of time, the casting of the deck, and the addition of other superimposed loads such as a sidewalk and traffic barriers. Among both the 132 ft. and 82 ft. girders, the variation in measured prestress was a maximum of 8%.

Also presented in Figs. 6.11 – 6.12 are the calculated prestress loss according the

AASHTO LRFD 2004 and 2007 Specifications as well as a refined method of the 2004

Specifications using measured values of compressive strength and static Young's

modulus. The lump sum method is consistent in all AASHTO LRFD Specifications and

is given by Eq. (6.6). For both spans, the AASHTO LRFD 2004 predictions were higher

than those made by the AASHTO LRFD 2007 Specifications. The AASHTO LRFD

2007 calculates the nearest prediction to the measured losses for both girders. However,

even with the AASHTO LRFD 2007 method, the predicted total losses are still

overestimated.

Figs. 6.13 – 6.14 presents the calculated prestress loss according the AASHTO

LRFD 2004 and 2007 Specifications as well as a refined method of the 2004

Specifications using the specified design values of compressive strength and static

Young's modulus.

Table 6.2 presents total measured and predicted losses (using measured values of

compressive strength and static Young's modulus) for each of the methods at the final

reading day. Also presented in Table 6.2 are values of percentage difference between the

calculated values and the measured values. Similarly, Table 6.3 presents total measured

and predicted losses (using specified design values of compressive strength and static

Young's modulus) for each of the methods at the final reading day. Also presented in

Table 6.3 are values of percentage difference between the calculated values and the

measured values.

$$\Delta f_{pT} = 33\left[1.0 - 0.15\frac{f_c' - 6.0}{6.0}\right] + 6.0 PPR \qquad (6.6)$$

where: Δf_{pt} = Total loss of prestress

PPR = partial prestressing ratio

Values of prestress loss calculated using measured values of compressive strength and static Young's modulus, presented in Table 6.2, indicate that the calculated prestress losses according to the AASHTO LRFD 2007 Specifications correspond most accurately with the measured losses. For the 132 ft. girders, the AASHTO LRFD 2007 losses were 3.7% smaller. For the 82 ft. girders, the difference was 7.9%. In contrast, the AASHTO LRFD 2004 Specification calculated losses that were 76.4% and 125% overestimates of the total prestress losses measured for the 132 ft. and 82 ft. girders, respectively. Finally, using the AASHTO LRFD 2004 Refined method, calculated losses were 16.5% and 59.2% overestimates of the measured losses on the 132 ft. and 82 ft. girders, respectively.
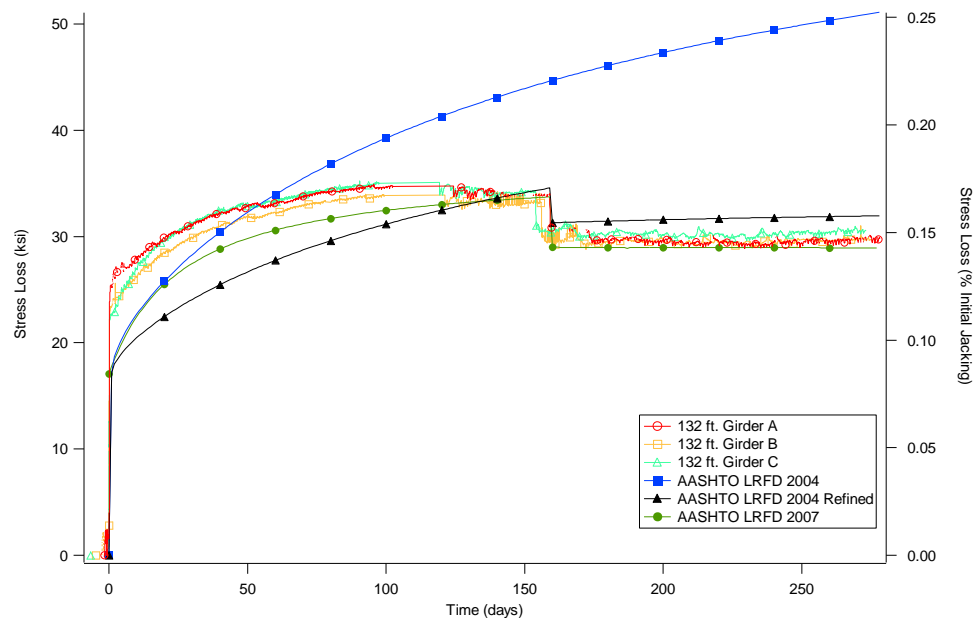
Fig. 6.11. Measured and calculated (using measured values) prestress losses for the 132 ft. girders
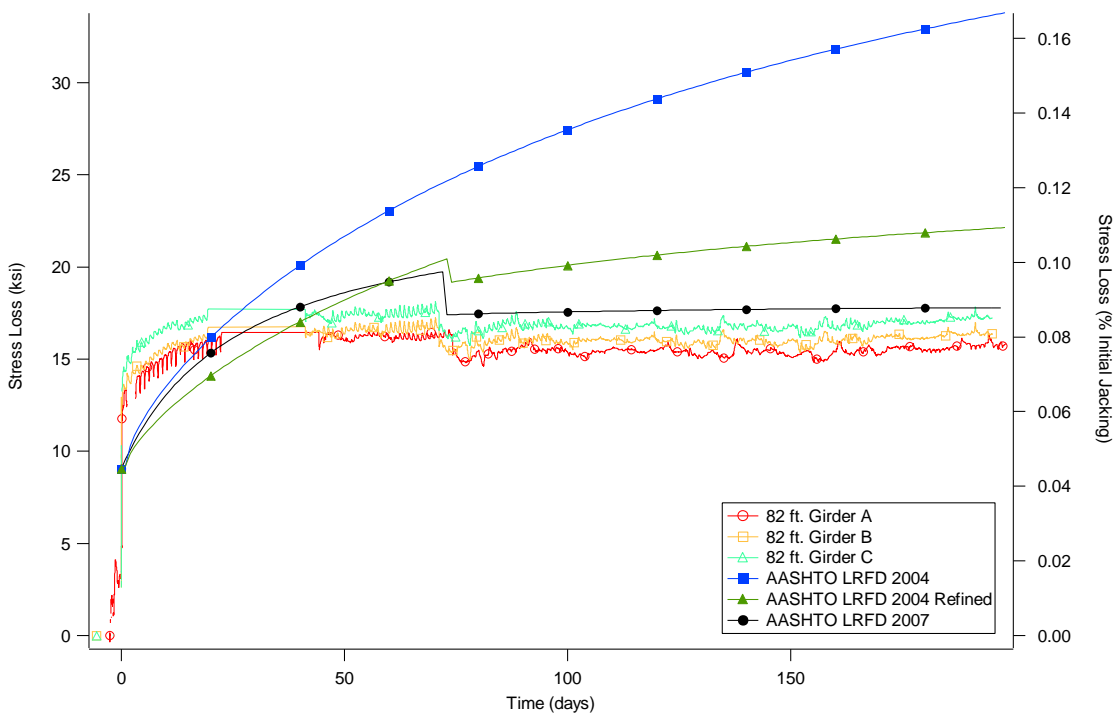
Fig. 6.12. Measured and calculated (using measured values) prestress losses for the 82 ft. girders
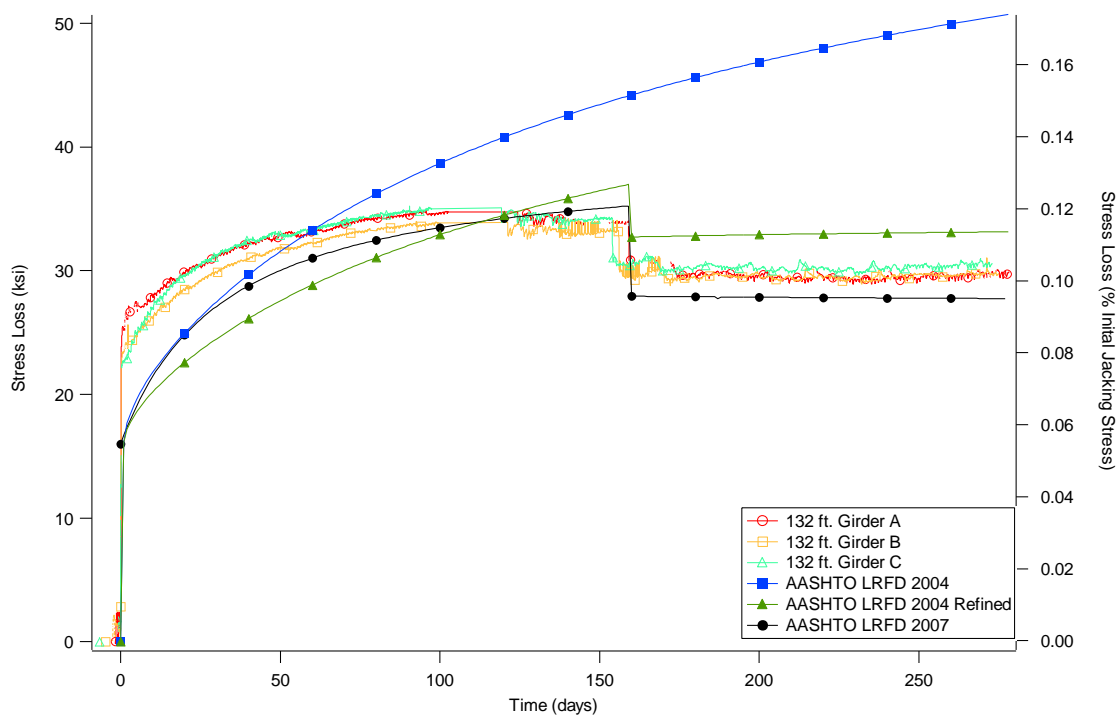
Fig. 6.13. Measured and calculated (using specified values) prestress losses for the 132 ft. girders
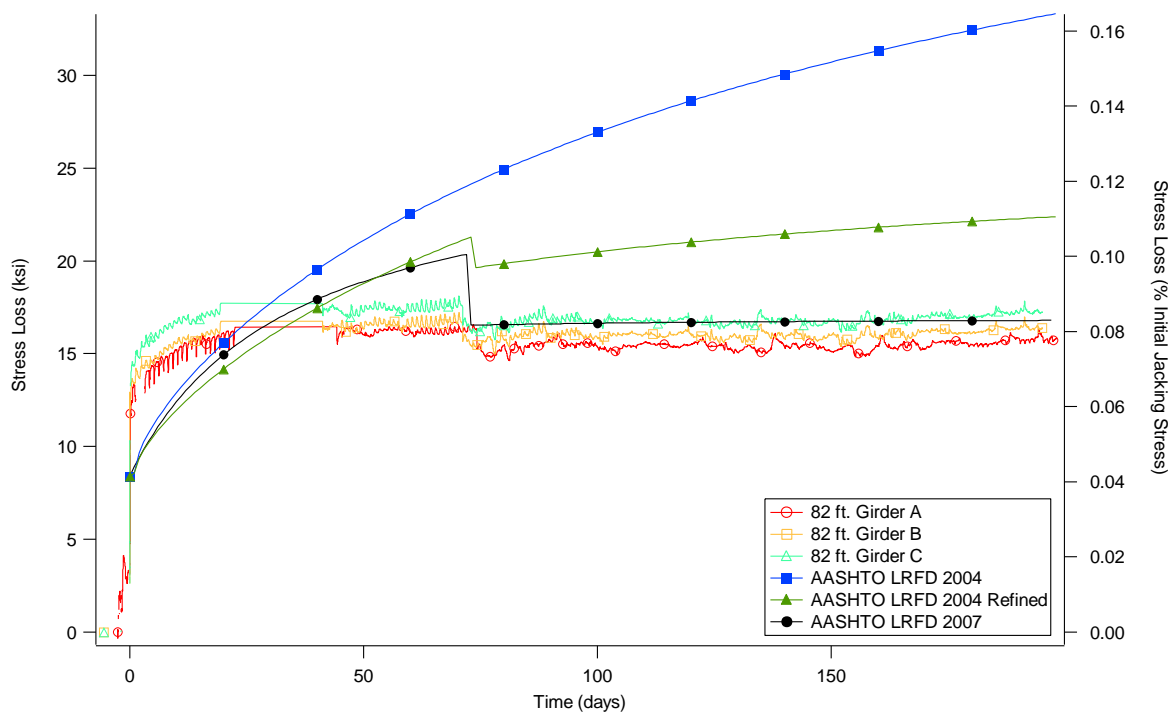
Fig. 6.14. Measured and calculated (using specified values) prestress losses for the 82 ft. girders

Similarly, values of prestress loss calculated using specific design values of compressive strength and static Young's modulus, presented in Table 6.3, indicate that the AASHTO LRFD 2007 Specifications most accurately predict the values of measured losses. This method predicts prestress losses correlating within 7.6% and 1.9% of the measured values for the 132 ft. and 82 ft. girders, respectively. Calculated losses determined using the AASHTO LRFD 2004 Specifications were 68.8% and 122% overestimates of the measured losses. Finally, using the AASHTO LRFD 2004 Refined method, losses calculated were 10.3% and 60.9% overestimates of the measured losses.

These results indicate that although the specified values of compressive strength static Young's modulus were lower than the measured values, all of the methods used to calculate prestress losses produced consistent results. The largest difference was found

using the AASHTO LRFD 2007 Specifications. For the 132 ft. girders, values calculated

using the measured values and specified design values were 3.7% smaller and 7.6%

larger than the measured losses, respectively. This represents a difference of only 1.18

ksi.

In order to investigate the discrepancies, the measured and predicted prestress loss

components (elastic shortening, creep and shrinkage, and differential shrinkage) were

compared.

Table 6.2. Total Calculated (using Measured Values) and Measured Prestress Losses for
the (a) 132 ft. and (b) 82 ft. Girders

(a)

	Prestress Loss (% Initial Jacking)	Percent Difference
AASHTO LRFD Lump Sum	0.16	10%
AASHTO LRFD 2004	0.26	76%
AASHTO LRFD 2004 Refined	0.17	17%
AASHTO 2007 Simplified	0.18	24%
AASHTO 2007 Refined	0.14	-4%
Average Measured Data	0.15	

(b)

	Prestress Loss (% Initial Jacking)	Percent Difference
AASHTO LRFD Lump Sum	0.16	99%
AASHTO LRFD 2004	0.18	125%
AASHTO LRFD 2004 Refined	0.13	59%
AASHTO 2007 Simplified	0.11	39%
AASHTO 2007 Refined	0.09	8%
Average Measured Data	0.08	

Table 6.3. Total Calculated (using Specified Values) and Measured Prestress Losses for the (a) 132 ft. and (b) 82 ft. Girders

(a)

	Prestress Loss (% Initial Jacking)	Percent Difference
AASHTO LRFD Lump Sum	0.19	25%
AASHTO LRFD 2004	0.25	69%
AASHTO LRFD 2004 Refined	0.16	10%
AASHTO 2007 Simplified	0.20	35%
AASHTO 2007 Refined	0.14	-8%
Average Measured Data	0.15	

(b)

	Prestress Loss (% Initial Jacking)	Percent Difference
AASHTO LRFD Lump Sum	0.18	125%
AASHTO LRFD 2004	0.18	122%
AASHTO LRFD 2004 Refined	0.13	61%
AASHTO 2007 Simplified	0.11	39%
AASHTO 2007 Refined	0.08	2%
Average Measured Data	0.08	

Elastic Shortening

After the concrete has gained sufficient strength in the casting bed, the forms are removed and the prestressing strands are released. As the prestressing force is transferred to the concrete, the girder axially shortens and cambers due to the prestressing force. Because the strands are now bonded to the concrete, they also shorten and lose a portion of the initial jacking prestressing force. This loss of prestressing force at release is termed elastic shortening loss and can be a significant portion of the total loss of force.

The AASHTO LRFD 2004 and 2007 Specifications present the same two formulas for the calculation of the loss due to elastic shortening:

$$\Delta f_{pES} = \frac{E_p}{E_{ci}} f_{cgp} \tag{6.7}$$

$$\Delta f_{pES} = \frac{A_{ps} f_{pbt} (I_g + e_m^2 A_g) - e_m M_g A_g}{A_{ps}(I_g + e_m^2 A_g) + \frac{A_g I_g E_{ci}}{E_p}} \tag{6.8}$$

where: Δf_{pES} = elastic shortening

E_p = modulus of elasticity of prestressing steel

E_{ci} = modulus of elasticity of concrete at transfer

f_{cgp} = sum of concrete stresses at the center of gravity of prestressing

tendons due to the prestressing force at transfer and the self-weight of the

member at the sections of maximum moment

A_{ps} = area of prestressing steel

A_g = gross area of section

e_m = average eccentricity at midspan

f_{pbt} = stress in prestressing steel immediately prior to transfer

I_g = moment of inertia of the gross concrete section

M_g = midspan moment due to member self-weight

When determining the prestress loss due to elastic shortening at midspan, either

Eq (6.7) or Eq. (6.8) can be used. However, when a more detailed analysis of a specific

section of a girder is required, Eq. (6.7) may be used at each section along the beam, in

places where loading conditions may differ.

The values calculated for elastic shortening using the measured elastic modulus

(Fig. 6.9) in Eqs. (6.7 – 6.8), and the average values measured on the 132 ft. and 82 ft.

girders are presented in Fig. 6.15.

The average measured losses due to elastic shortening were 18.33 ksi, 19.16 ksi, and 16.57 ksi for 132 ft. girders A, B, and C and 8.48 ksi, 10.02 ksi, and 8.98 ksi for 82 ft. girders A, B, and C, respectively. The calculated values for elastic shortening were 17.07 ksi and 9.05 ksi, and correlated to the measured values by 93%, 89%, and 103%, and 94%, 111%, and 99%, respectively. The measured and calculated losses represent 9.1%, 9.5%, and 8.2%, and 4.4%, 4.9%, and 4.4% of the initial jacking stress for the 132 ft. girders A, B, and C, and the 82 ft. girders A, B, and C, respectively.

Also, Eq. (6.2) was used to determine a calculated value of modulus of elasticity. Using this value, the calculated values for prestress loss due elastic shortening for the 132 ft. and 82 ft. girders were 16.0 and 8.4 ksi, respectively. The calculated values for elastic shortening using the calculated value of elastic modulus correlated to the measured values by 114%, 120%, and 104%, and 101%, 119%, and 107%, for the 132 ft. girders A, B, and C, and the 82 ft. girders A, B, and C, respectively.

The results indicate that the measured and calculated values of elastic moduli were very similar, and in fact this was found to be true. The measured value of static Young's modulus at day 1 was an average of 4.21×10^6 psi (Table 6.1) and the value calculated using Eq. (6.2) was 4.6×10^6 psi. The static Young's modulus determined using Eq. (6.3) was not used in the calculation of elastic shortening because it is not suggested by any of the AASHTO LRFD Specifications.

On average, the measured value of elastic modulus was a better indicator of prestress loss due to elastic shortening.
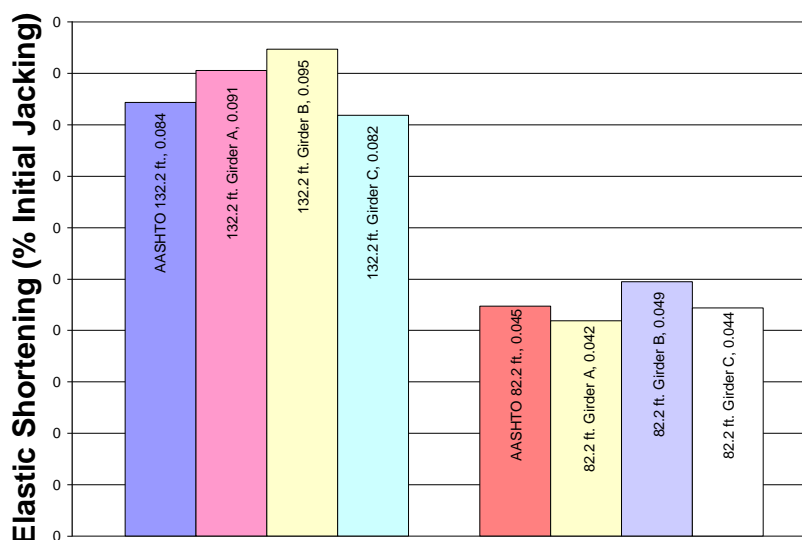
Fig. 6.15. Measured and calculated prestress losses due to elastic shortening

Creep and Shrinkage

Creep is defined as an increase in strain as a function of time due to a constant stress. In the case of concrete, the constant stress is due to prestress force, self weight, and superimposed dead loads. Thus, concrete creep is a time-dependent flow caused by its subjection to stress. This deformation occurs rapidly at first and then decreases with time, and, in prestressed concrete girders, can be several times larger than the deformation due to elastic shortening. Creep has been found to depend on mix proportions, humidity, curing conditions, and maturity of the concrete when first loaded (Neville 1996). The creep deformation causes a change of the prestressing strand strain, which changes the strand stress.

There are two types of shrinkage that affects the girder concrete, basic and drying shrinkage. Basic shrinkage is caused by the hydration of the cement as the concrete cures and is independent of the volume or surface of the concrete structure. The evaporation of excess water during curing is the cause of drying shrinkage. Drying shrinkage is

unrelated to load application or thermal effects. The amount of water contained in most

concrete mixes is more than is needed for the complete hydration of the cementitious

materials. This excess water leaches to the surface and evaporates as a function of time.

As the excess water makes it to the surface and evaporates the concrete structure is

reduced in volume. The rate of volume reduction occurs initially at a high rate and later

diminishes with time. This is due to both the lack of excess water and increase in

stiffness as the concrete cures. Shrinkage is affected by many parameters, including mix

proportions, type of aggregate, cement type, time between the end of external curing and

the application of loading, and environmental conditions (Neville 1996). As was the case

for creep, shrinkage of the concrete causes shortening of the prestressing strands which

reduces the prestressing force.

The measured change in strain in the prestressing strands due to creep and

shrinkage was computed by subtracting the measured strain due to elastic shortening

from the average measured change in strain at the prestressing centroid as a function of

time. Corresponding values of creep and shrinkage were also calculated using the

AASHTO LRFD 2004, 2004 Refined, and 2007 Specifications.

The AASHTO LRFD 2004 Specification defines the prestress losses due to creep

and shrinkage as:

$$\Delta f_{pCR} = 12.0 f_{cgp} - 7.0 \Delta f_{cdp} \geq 0 \tag{6.9}$$

$$\Delta f_{pSR} = (17.0 - 0.15H) \tag{6.10}$$

where: Δf_{pCR} = prestress loss due to creep

Δf_{cdp} = change in concrete stress at center of gravity of prestressing steel due to permanent loads, with the exception of the load acting at the time the prestressing force is applied

Δf_{pSR} = prestress loss due to shrinkage

H = the average annual ambient relative humidity

The AASHTO 2004 Refined method specifies the prestress losses due to creep and shrinkage as:

$$\Delta f_{pCR} = \eta_{CR,TR}(t, t_{i,TR}) f_{cgp} - \eta_{CR,LT}(t, t_{i,LT}) \Delta f_{cdp} \tag{6.11}$$

$$\Delta f_{pSR} = E_p \varepsilon_{SH} \tag{6.12}$$

$$\varepsilon_{SH} = -k_s k_h \left(\frac{t}{35+t} \right) 0.51 \times 10^{-3} \tag{6.13}$$

where: $\eta_{CR,TR}$ = creep modular ratio at transfer

t = time

$t_{i,TR}$ = age of concrete at transfer

$\eta_{CR,LT}$ = creep modular ratio for permanent loads

$t_{i,LT}$ = age of concrete when permanent loads are applied

ε_{SH} = strain due to shrinkage at time, t

k_s = factor for the effect of the volume to surface ratio

k_h = humidity factor.

Finally, the AASHTO LRFD 2007 Specifications define prestress losses due to creep and shrinkage as:

$$\Delta f_{pCR} = \frac{E_p}{E_{ci}} f_{cgp} \psi_b(t_d, t_i) K_{id} \tag{6.14}$$

$$\Delta f_{pSR} = \varepsilon_{bid} E_p K_{id} \qquad (6.15)$$

where: $\psi_b(t_d,t_i)$ = girder creep coefficient at time of deck placement due to loading

introduced at transfer

K_{id} = transformed section coefficient that accounts for time dependent

interaction between concrete and bonded steel in the section being

considered for time period between transfer and deck placement

ε_{bid} = concrete shrinkage strain of girder between the time of transfer and

deck placement

The calculated values of prestress loss due to creep and shrinkage are

overestimated by nearly all design specifications (Fig. 6.16, Tables 6.4 – 6.5). The

AASHTO LRFD 2007 Specifications did the best job and predicted the losses due to

shrinkage and creep for the 132 ft. and 82 ft. girders within 1.3% and 19.3%,

respectively. This discrepancy is mostly likely due to the irregularly high values of

compressive strength and modulus of elasticity. The AASHTO LRFD 2004 and 2004

Refined Specifications are based on conventional strength concrete which is believed to

have larger creep and shrinkage losses. Although the AASHTO LRFD 2007

Specifications include methodologies to incorporate HPC, the measured values of

compressive strength and modulus of elasticity of the HPSCC used are higher than those

typically recognized for HPC. This may be the cause for the over prediction of prestress

loss due to creep and shrinkage by the AASHTO LRFD 2007 Specifications. Also, Fig.

6.10 presents a close correlation between the shrinkage strain of HPSCC concrete

specimen and the values calculated using AASHTO LRFD Specifications. This close

correlation between measured and calculated strains due to shrinkage indicates that the

discrepancies found in the creep and shrinkage prestress loss predictions may be due

mostly to creep.

Deck Casting

AASHTO LRFD 2004 Refined and 2007 Specifications include provisions to

include the prestress gains during deck placement. The values calculated by these two

codes are presented along with measured values in Fig. 6.17. Fig. 6.17 shows that,

excluding the 132 ft. girder A, the values predicted by both codes correlate within 10%

for the 132 ft. girders and 15% for the 82 ft. girders. The AASHTO LRFD 2004 Refined

method provides this additional prestress through changes in creep induced loads

calculated using Eq. (6.11). The AASHTO LRFD 2007 Specifications suggest formulas

to predict prestress losses from both shrinkage and creep between the time of deck

placement and final time, Eqs. (6.16 and 6.17, respectively).

$$\Delta f_{pSD} = \varepsilon_{bdf} E_p K_{df} \qquad (6.16)$$

$$\Delta f_{pCD} = \frac{E_p}{E_{ci}} f_{cgp} \psi_b \big[(t_f, t_i) - \psi_b (t_d, t_i) \big] K_{df} + \frac{E_p}{E_c} \Delta f_{cd} \psi_b (t_f, t_d) K_{df} \qquad (6.17)$$

where: ε_{bdf} = shrinkage strain of girder between the time of deck placement and

final time

K_{df} = transformed section coefficient that accounts for time-dependent

interaction between concrete and bonded steel in the section being

considered for time period between deck placement and final time

$\psi_b(t_f, t_i)$ = girder creep coefficient at final time due to loading introduced at

transfer

f_{cd} = change in concrete stress at centroid of prestressing strands due to

shrinkage of deck concrete

$\psi_b(t_f,t_d)$ = girder creep coefficient at final time due to loading at deck

placement

Overall, the values of prestress gain due to the deck placement represent only a small component of the overall losses. Also, the measured gains may be smaller than the actual gains due to the boundary conditions of the girders (i.e. they are restrained at the abutments). Finally, the load induced to the exterior girders due to their larger tributary areas would cause a larger gain than measured on the interior girders.
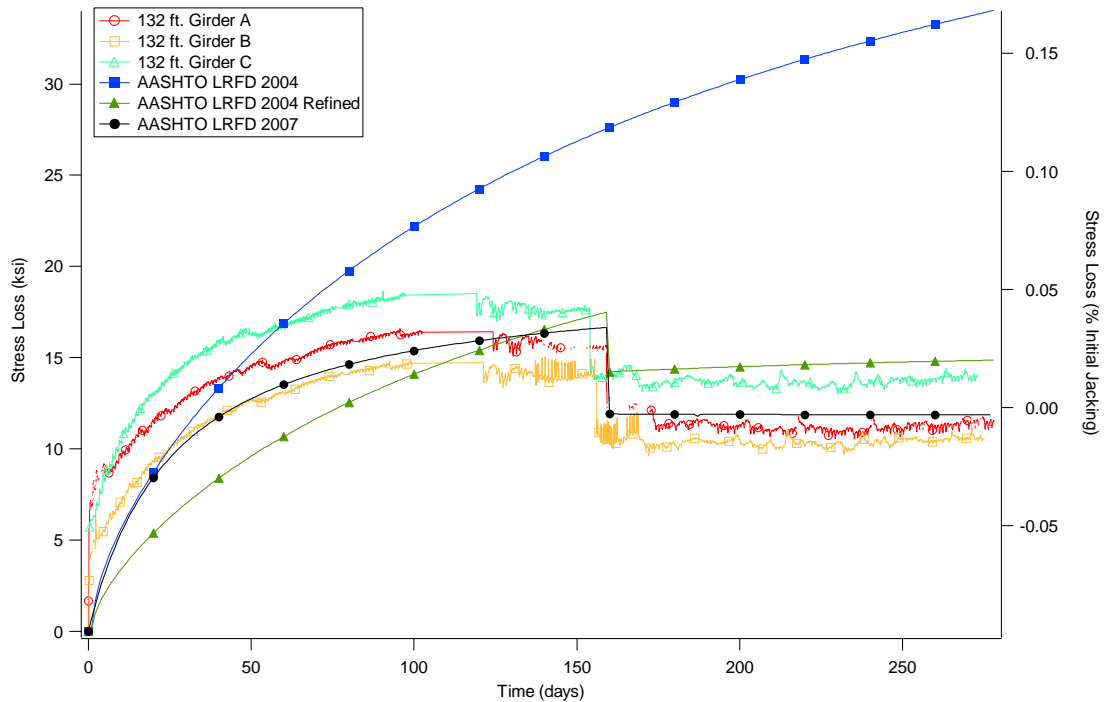
(a) 132 ft. girder

Fig. 6.16. Measured and calculated (using measured values) prestress losses due to creep and shrinkage
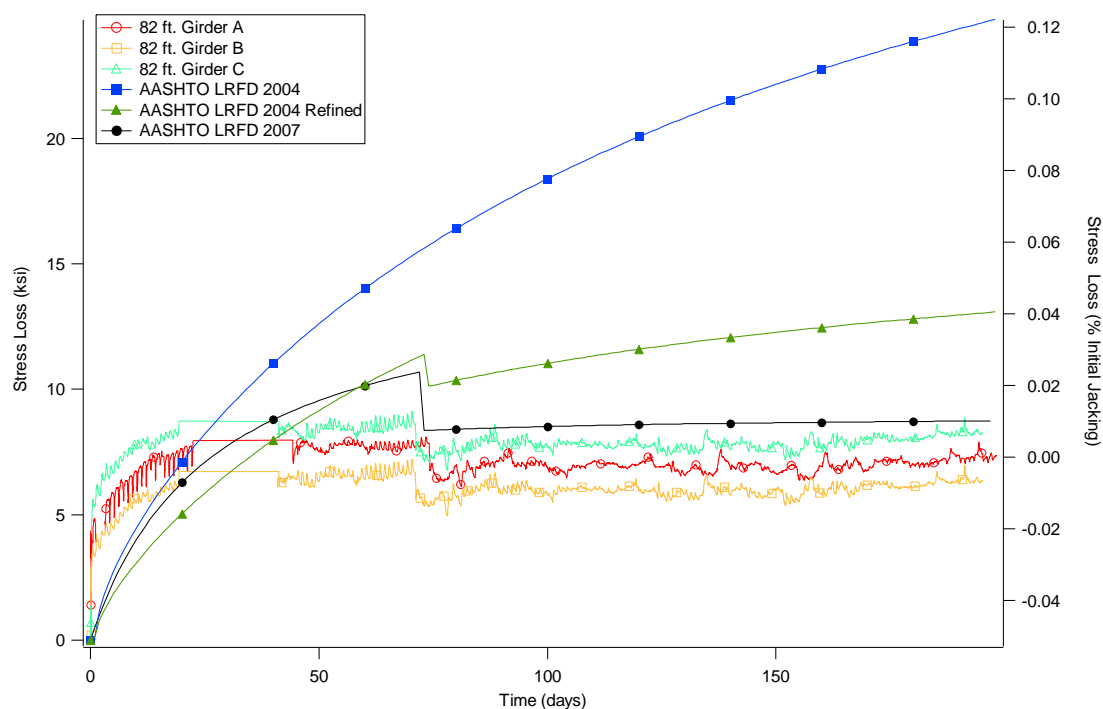
(b) 82 ft. girder

Fig. 6.16. (continued)

Table 6.4. Calculated and Measured Prestress Losses Due to Creep and Shrinkage for the (a) 132 ft. and (b) 82 ft. Girders Using Measured Values of static Young's Modulus

(a)

	Prestress Loss (% Initial Jacking)	Percent Difference
AASHTO LRFD 2004	0.18	199%
AASHTO LRFD 2004 Refined	0.09	49%
AASHTO 2007 Refined	0.06	-1%
Average Measured Data	0.06	

(b)

	Prestress Loss (% Initial Jacking)	Percent Difference
AASHTO LRFD 2004	0.138	282%
AASHTO LRFD 2004 Refined	0.085	135%
AASHTO 2007 Refined	0.043	19%
Average Measured Data	0.036	

Table 6.5. Calculated and Measured Prestress Losses Due to Creep and Shrinkage for the (a) 132 ft. and (b) 82 ft. Girders Using Specified Values of Static Young's Modulus

(a)

	Prestress Loss (% Initial Jacking)	Percent Difference
AASHTO LRFD 2004	0.171	189%
AASHTO LRFD 2004 Refined	0.085	43%
AASHTO 2007 Refined	0.058	-2%
Average Measured Data	0.059	

(b)

	Prestress Loss (% Initial Jacking)	Percent Difference
AASHTO LRFD 2004	0.140	286%
AASHTO LRFD 2004 Refined	0.090	148%
AASHTO 2007 Refined	0.042	15%
Average Measured Data	0.036	
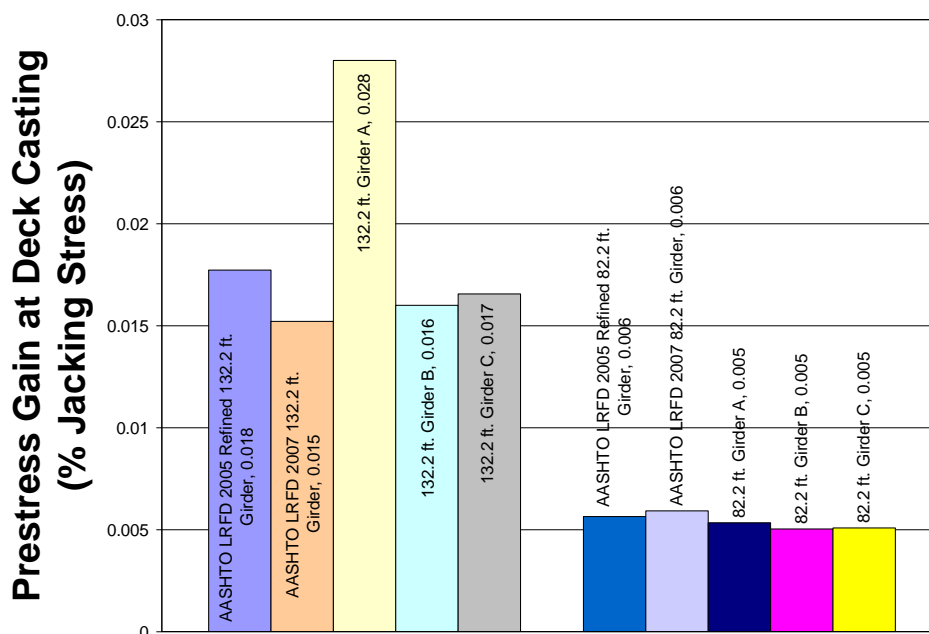
Fig. 6.17. Measured and calculated prestress gains at deck placement

Differential Shrinkage

One explanation as to why the calculated AASHTO LRFD 2007 creep and shrinkage losses were lower than those calculated by the AASHTO LRFD 2004 and 2004 Refined Specifications can be explained by comparing the differential shrinkage losses. Stress loss due to shrinkage of composite, prestressed concrete girders comes from two sources. The first source is the shrinkage of the girder concrete. The second source is the shrinkage of the deck concrete. The deck concrete is typically placed several months after the girder concrete has been cast. Thus, the rate of creep and shrinkage of the girder concrete has decreased by the time the deck is placed. However, the deck concrete has yet to experience its shrinkage. The effect of differences between the shrinkage strain of the deck concrete and the shrinkage strain of the girder concrete is termed differential shrinkage.

The AASHTO LRFD 2004 and 2004 Refined Specifications do not explicitly take into account differential shrinkage in its calculations of changes prestress. The AASHTO LRFD 2007 Specifications does include differential shrinkage. The change in stress due to differential shrinkage can be calculated as:

$$\Delta f_{pSS} = \frac{E_p}{E_c} \Delta f_{cdf} K_{df} \left[1 + 0.7 \psi_d (t_f, t_d) \right] \tag{6.16}$$

where: Δf_{pSS} = the prestress gain due to shrinkage of deck composite section

Δf_{cdf} = change in concrete stress at centroid of prestressing strands due to shrinkage of deck concrete

K_{df} = transformed section coefficient that accounts for time dependent

interaction between concrete and bonded steel in the section being

considered for time period between deck placement and final time

$\psi_d(t_f, t_d)$ = creep coefficient of deck concrete at final time due to loading

introduced shortly after deck placement (i.e. overlays, barriers, etc.)

Values calculated for prestress loss due to differential shrinkage of the 132 ft. and

82 ft. girders were 2.70 ksi and 1.80 ksi, respectively using the measured values of elastic

modulus and compressive strength. The values grew to 4.16 and 3.24, respectively, when

the specified values were used. This is due to the fact that the specified values were

lower than the measured values, thus increasing strains and prestress loss due to

differential shrinkage. Fig. 6.18 presents average measured values of the 132 ft. and 82

ft. girders along with values of prestress loss due to differential shrinkage calculated

using the AASHTO LRFD 2007 Specifications. Values were calculated and are

presented using both measured and specified static Young's moduli and compressive

strengths.

Fig. 6.18 shows that from the time of deck placement to final time, values of

prestress loss due to differential shrinkage do an adequate job of predicting the behavior

for both the 132 ft. and 82 ft. girders. However, there is a great deal of scatter in the

measured values probably due to temperature induced stress changes and traffic. Thus, it

is difficult to measure exactly which calculated value best predicts the measured

behavior. However, the calculated values of differential shrinkage determined using

specified values of elastic moduli and compressive strength appears to provides a closer

fit for the 132 ft. girder. In contrast, the calculated values of differential shrinkage

determined using measured values of elastic moduli and compressive strength appears to

provides a closer fit for the 82 ft. girder.
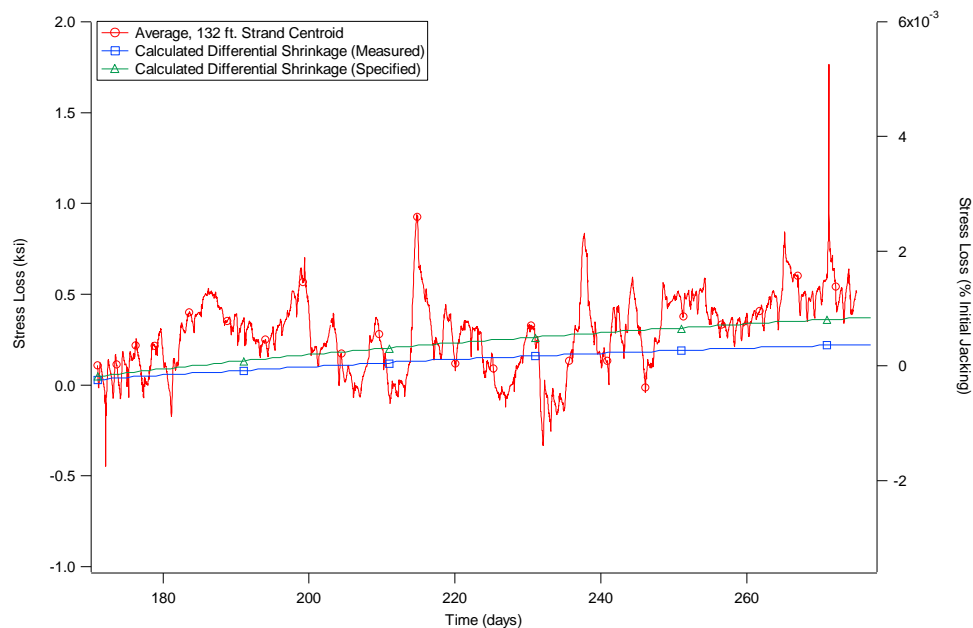
(a) 132 ft. girder
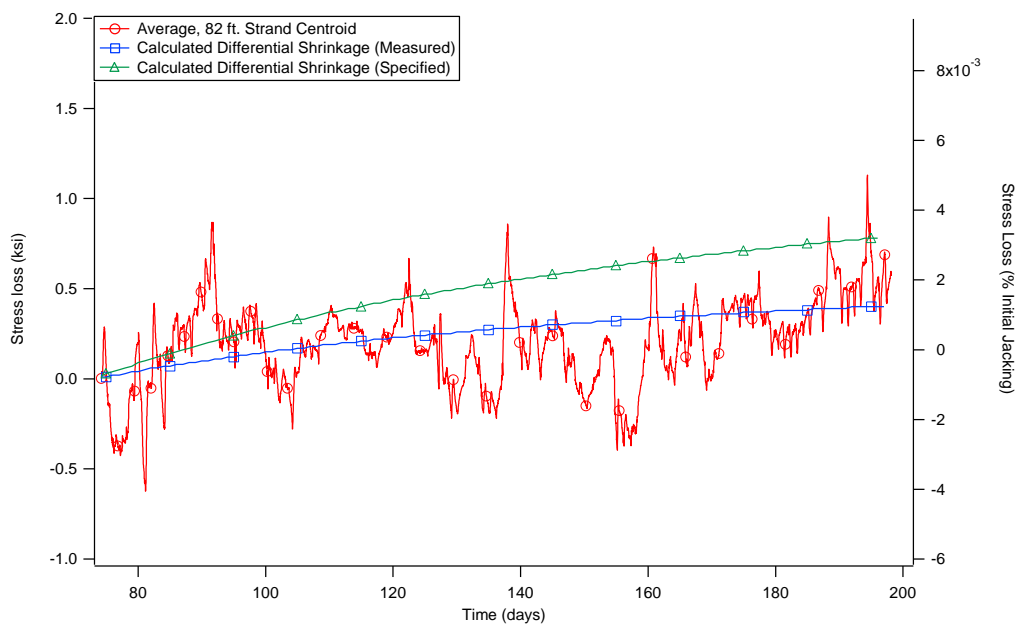
(b) 82 ft. girder

Fig. 6.18. Measured and calculated prestress losses due to differential shrinkage

Conclusions and Recommendations

This study describes the measured behavior of six high performance, self-consolidating concrete (HPSCC), prestressed bridge girders using embedded vibrating wire strain gages (VWSG). Measurements were made on material specimens of the HPSCC used to make the bridge girders. The measured strains for the VWSGs were used to determine prestress losses that were compared to calculated values obtained using the 2004 and 2007 AASHTO LRFD Specifications. The study led to the following conclusions and recommendations:

1. Values calculated for the compressive strength using ACI 318-05 (Eq. (1) in this study) were approximately 31.7% smaller than the measured values at day 1. This under estimation grew smaller as a function of time and by day 56 the measured and calculated values correlated within 1%. Values of static Young's modulus calculated with ACI 318-05 (Eq. (2) in this study) varied from approximately 29% smaller to 21% larger than the measured values on days 1 and 56, respectively. However, values of static Young's modulus calculated using the equation suggested by ACI committee 209 (Eq. (6.3) in this study) were approximately 27% smaller at day 1, but within a 2% correlation on days 7, 28, and 56. Shrinkage strains calculated in accordance with AASTHO LRFD Specifications (Eq. (6.4) in this study) were approximately 40% smaller than the average measured value at day 7 and 1% and 11% at days 28 and 56, respectively.

2. The average measured prestress losses after the deck was cast were 29.8 ksi and 16.1 ksi corresponding to approximately 14.7% and 8.0% of the initial jacking stress of 202.5 ksi for the 132 ft. and 82 ft. girders, respectively.

3. Among both the 132 ft. and 82 ft. girders, the variation in measured prestress was a maximum of 8%.

4. AASHTO LRFD 2007 Specifications predicted the total prestress loss within 3.7% and 7.9% for the 132 ft. and 82 ft. girders, respectively. In contrast, the predictions calculated using the AASHTO LRFD 2004 Specification were 76.4% and 125% overestimates of the total prestress losses measured for the 132 ft. and 82 ft. girders, respectively. Finally, the AASHTO LRFD 2004 Refined method predicted losses within 16.5% and 59.2% of the measured losses for the 132 ft. and 82 ft. girders, respectively

5. Values of prestress loss due to elastic shortening determined using the AASHTO LRFD 2007 Specifications were within 7.0% and 6.2% for the 132 ft. and 82 ft. girders, respectively.

6. The calculated values of prestress loss due to creep and shrinkage calculated using the AASHTO LRFD 2007 Specifications predicted the losses due to shrinkage and creep for the 132 ft. and 82 ft. girders most accurately within 1.3% and 19.3%, respectively.

7. This study shows that design practices are improving, and that prestress losses for high strength self-consolidating concrete can be predicted with them.

8. The largest discrepancies between measured and predicted prestress loss values were due to calculated values of creep and shrinkage. Future AASHTO LRFD Specifications should continue to develop more appropriate equations for the calculation of these values for HPC.

CHAPTER 7

RELATIONSHIP BETWEEN STATIC AND DYNAMIC YOUNG'S MODULI

Abstract

The variation in the ratio of static to dynamic Young's modulus as a function of the compressive strength, time, and damping ratio was studied. The details of the concrete mixes tested, instrumentation used, experimental setup, and the methods of measurement and analysis are provided. It was found that the ratio of static to dynamic Young's modulus is a function of compressive strength, time, and damping. By testing a broader range of concretes comprised of varying compressive strengths at multiple times, a formula to describe the ratio of static to dynamic Young's modulus is proposed. Also, this study shows that the dynamic Young's modulus can be accurately predicted by measuring a small strain secant modulus on statically determined stress-strain curves.

Introduction

In solid mechanics, Young's modulus, E, is a measure of stiffness, and is defined as the ratio of the rate of change in stress with strain. Young's modulus can be experimentally determined, either in tension or compression, from the slope of a stress-strain curve measured during uniaxial loading. Young's modulus is named for the 18th Century British Scientist Thomas Young. However, Leonhard Euler developed the concept in 1727 and Giordano Riccati predated Young's work by 25 years with the first experiments that used the concept of Young's modulus in its current form in 1782 (Wikipedia 2008). When applying these concepts to the testing of concrete, the modulus described above is known as the static Young's modulus, E_s, and methods to determine

its value are specified in ASTM C 469 (2002), the "Standard Test Method for Static

Modulus of Elasticity and Poisson's Ratio of Concrete in Compression."

In addition to research regarding the static Young's modulus in which a

significant stress is required, research has been performed to determine the value at small

stress and strains. In 1877, Lord Rayleigh reported a "mathematical relationship existing

between the velocity of sound through a specimen and its resonant frequency and the

relationship of these two to the modulus of elasticity of the material." The relationship

between the resonant frequency and what is termed the dynamic modulus of elasticity

was thus found. In this case, the resonant frequency referred to is the longitudinal

resonant frequency.

In 1938, T.C. Powers laid the groundwork for the dynamic testing of concrete

samples. He was able to determine the resonant frequency of concrete samples, usually 2

x 2 x 9 ½ in., by supporting the sample at its nodal points (1/3 and 2/3 times the length of

the specimen), striking it with a hammer, and matching the musical tone that was

produced with a calibrated tone source. Powers used a set of Deagan orchestra bells and

a homemade sonometer for the tone source. He found that the error likely to occur using

the bells was on the order of approximately 3% while the error using the sonometer was

much less (Whitehurst 1966). In 1939, Hornibrook refined the method by using

electronic equipment to measure the resonance. Other early investigations on the

development of this method included those by Obert and Duvall (1941), and by Stanton

(1944). In these tests, a sonometer was used to measure the resonant frequencies of the

tested specimens. These processes have evolved into the method that is designated as

standard ASTM C 215 (2002), the "Standard Test Method for Fundamental Transverse,

Longitudinal, and Torsional Resonant Frequencies of Concrete Specimens."

In the case of the dynamic Young's modulus, the measured modulus is almost purely elastic. This is due to the absence of a significant applied stress and as a result, the lack of micro cracking induced creep. In this case, a specimen could be loaded and unloaded without significantly affecting the linear elastic properties of the material. Because the dynamic modulus refers to almost purely elastic response, it has typically been considered equal to the initial tangent modulus determined in the static test (Neville 1996; Mehta and Monteiro 2006).

The difference between static and dynamic Young's modulus is of great importance to engineers for several factors. The static Young's modulus is typically assumed to quantify the stiffness of a material during the design phase of a concrete structure. The American Concrete Institute (ACI), Prestress Concrete Institute (PCI), and American Associate of State Highway and Transportation Officials (AASHTO) all suggest methods to calculate the static Young's modulus. Using the equations suggested by each, an engineer could determine an appropriate value of Young's modulus to use in equations to determine deflection, ductility, and other important properties of a designed structure. The dynamic Young's modulus, however, is a measured value. There are currently no accepted design equations from which the dynamic Young's modulus can be calculated. Also, because it can be measured using nondestructive techniques, it is much easier to determine its value on an in-place structure. Due to these differences, there is a growing need for the capability to calculate one moduli from the other.

There has long been a debate concerning the magnitude of the ratio between the static and the dynamic Young's modulus of elasticity and the difference in material

behavior required to cause this ratio. Most literature defines the static Young's modulus

of elasticity of concrete as a chord modulus calculated based on an initial strain (typically

0.0005) and a higher strain typically determined as the ultimate compressive stress

(typically 40%). These researchers also agree that the dynamic modulus should be

considered the initial tangent modulus of a concrete stress-strain curve (Neville 1996;

Mesbah et al. 2002; Mehta and Monteiro 2006). Because of the nonlinearity of the

stress-strain curve typically measured on concrete specimens, the ratio of static to

dynamic Young's modulus is always less than one. Studies have also shown that as the

strength of the concrete increases, the stress strain curve becomes more nearly linear. As

this happens, the value of the static modulus increases, and the ratio between the dynamic

modulus and the static modulus approaches unity (Neville 1996). Although this ratio

depends entirely on the specific concrete being measured, studies have been performed in

an attempt to quantify the relationship. Several equations have been suggested.

Nagy (1997) obtained moduli measurements on two different concrete mixes and

used the results to develop a relationship between the static and dynamic Young's

moduli. The relationship is based on the damping ratio of the concrete specimen and is

listed as Eq. (7.1).

$$E_s = \frac{E_d}{1 + \eta^\alpha} \tag{7.1}$$

where: E_d = dynamic Young's modulus

η = damping ratio

α = an empirical factor

In his study, Nagy found α to be approximately equal to 0.35. He also found that

the ratio between static and dynamic moduli to be approximately 0.80 after a few days of curing. This value is widely accepted as the approximate ratio between static and dynamic Young's moduli and has been reported as 0.83 by Lydon and Balendran in 1986 (Neville 1996). Nagy found his results to be independent of the w/c ratio or cement type. Seely (2005) also studied three concrete mixes and found α to be approximately equal to 0.359, thus validating Nagy's research.

Mesbah et al. (2002) conducted a study on three different high performance concrete mixes. The researchers also concluded that the dynamic modulus is considered to be approximately equal to the initial tangent modulus obtained during a static test. Because the literature reviewed in their research consisted of measurements performed on normal weight concrete, they proposed a formula to convert dynamic to static Young's moduli for high performance concrete:

$$E_s = 9 \times 10^{-11} \left(65 E_d + 1600\right)^{3.2} \tag{7.2}$$

where moduli are in units of GPa. They found that with this formula they were able to accurately predict either the static Young's modulus from the dynamic Young's modulus or vice versa for the three tested mixes. However, they found this formula to be significantly dependent on age of the concrete and it was only held true for the mixes tested.

Han and Kim (2004) performed a study on four concrete mixes cured at various temperatures. The four concrete mixes were composed of two types of cements with two w/c ratios. The four mix designs had a range in compressive strengths based on the curing temperature from 3800 psi to 6500 psi at 28 days. They found that the slope of the initial chord elastic modulus from values of 10×10^{-6} to 50×10^{-6} was more closely

related to the dynamic Young's modulus than the initial tangent modulus. They proposed

a formula based on several assumptions (Eq. (7.3)). The assumption that as the strength

of the concrete increases, the dynamic elastic modulus increases, and the stress-strain

curve below 40% of the ultimate compressive strength becomes more linear was made.

This led to the assumption that as the linearity of the stress-strain curve increases, the

difference between the static and dynamic moduli decreases. Finally, they assumed that

when the static modulus is zero, the dynamic modulus is zero.

$$E_s = E_d \left(1 - ae^{-bE_d} \right) \tag{7.3}$$

where a and b are constants used to fit the calculated data to the measured data and

moduli are in units of GPa. They found a to range from 0.492 to 1.021 and b to range

from 0.0170 to 0.0431. They concluded that since the experimental data had dissimilar

ranges at different ages, the comparison between dynamic and static moduli could not be

accurately quantified as a function of age. They also concluded that the relationship

between dynamic Young's modulus and compressive strength was not significantly

affected by cement type or age. In addition, the curing temperature did not have a large

influence on the relationship between the initial chord modulus and the dynamic Young's

modulus, and cement types did not significantly affect the relationship between static and

dynamic Young's moduli.

Although the research comparing the static and dynamic moduli appears to be

various, most literature agrees that the ratio between the static and dynamic Young's

modulus is approximately 0.83, and that this difference is mostly dependent on strength

and age (Lydon and Balendran 1986; Neville 1996; Mesbah et al. 2002; Seely 2005;

Mehta and Monteiro 2006). Results from other studies also showed that the static

Young's modulus could be directly calculated using dynamic Young's modulus and damping ratio measurements (Nagy 1997; Seely 2005). Finally, a majority of the reviewed literature agrees that the dynamic Young's modulus is approximately equal to the initial tangent modulus measured using static tests (Neville 1996; Mesbah et al. 2002; Mehta and Monteiro 2006).

The goal of this study is to for accurately quantify the ratio between the static and dynamic Young's modulus. As a result, the variation in the ratio of static to dynamic Young's modulus as a function of the three most consistent factors shown by previous researchers to affect that ratio, compressive strength, damping ratio, and time, was studied. The details of the concrete mixes, instrumentation used, experimental setup, and the methods of measurement and analysis are provided. By testing a wider range of concrete mixes, in comparison to previous research, a formula that describes this ratio was developed. Also, this study will show that the dynamic Young's modulus is more aptly predicted by measuring a secant modulus to small strains rather than an initial tangent modulus on statically determined stress-strain curves.

Young's Modulus of Elasticity

Young's modulus of elasticity is defined as the slope of the elastic portion of the stress–strain curve of a material under uniaxial loading. However, because the shape of the stress-strain curve for concrete is nonlinear, there exist several portions of the stress-strain curve that engineers have used to determine Young's modulus. The tangent modulus is defined as the slope of a line drawn tangent to any point on the stress-strain curve (between points O and T of Fig. 7.1). A secant modulus is defined as the slope of

the line drawn between the origin and any other point on the stress-strain curve (between points O and σ_2, ε_2 of Fig. 7.1). Finally, the chord modulus is defined as the slope of a line drawn between any two points on the stress-strain curve (i.e. between points σ_1, ε_1 and σ_2, ε_2 of Fig. 7.1).

ASTM C 469 (2002) defines the static Young's modulus of elasticity as the slope of the chord modulus drawn between points corresponding to a strain of 0.00005 and 40% of the ultimate compressive stress. According to this procedure, a concrete cylinder is instrumented with a compressometer equipped with a strain gauge. A uniaxial load is applied to the cylinder in the direction parallel with the stroke of the gauge, and a change in length is measured. Cylinders are often also instrumented with an extensometer to measure changes in radial dimensions (Fig. 7.2). Using both axial and radial measurements, the Poisson's ratio of the material can be determined. Due to the difficulty in obtaining reliable extensometer readings, cylinders were instrumented only with compressometers, for this study. From the change in length measured using the compressometer, the strain can be calculated. Eq. (7.4) defines the static Young's modulus according to ASTM C 469 (2002).

$$E_s = \frac{\sigma_2 - \sigma_1}{\varepsilon_2 - \varepsilon_1} \tag{7.4}$$

where: σ_2 = stress corresponding to 40% of the ultimate compressive stress

σ_1 = stress corresponding to ε_1; ε_1 = strain of 0.00005

ε_2 = strain corresponding to σ_2.

ASTM C 215 (2002), or the free-free resonant column method (FFRC), as it will be referred to in this study, designates a technique to determine the dynamic Young's

modulus of a concrete specimen through the use of a nondestructive test. This test requires a digital signal analyzer, accelerometer, and an impact device. The specimen is placed in a free-free condition with an accelerometer attached to one end and an impact is imparted on the other end (Fig. 7.3). The digital signal analyzer then records the time signal recorded by the accelerometer and transforms it into the frequency domain using a Fast Fourier Transform (FFT).

Experimental Testing

Five concrete mixes were tested which included the effects of multiple aggregate types, water / cement ratios, and cement types. Because previous research showed that the ratio of static to dynamic Young's modulus was independent of cement type, w/c ratio, and curing temperatures, the various concrete mixes were chosen to be able to measure concrete properties representing a range in strengths and damping ratios. Also, three mixes previously tested at Utah State University were included in the results. The concrete mixes had 28 day compressive strengths ranging from 1880 psi to 12560 psi (Table 7.1). The available mix designs for the tested and previously tested mixes are presented in Table 7.2. One mix design was not available due to proprietary reasons. All concrete specimens were 6 in. x 12 in. cylinders. A hydraulic compression machine with a computer controlled servo unit was used to load and unload the specimens at a rate of 35 psi/sec. A compressometer equipped with a linear voltage displacement transducer was used to record the measured changes in length during the uniaxial compression testing to determine the stress-strain curve for each specimen (Fig. 7.4).
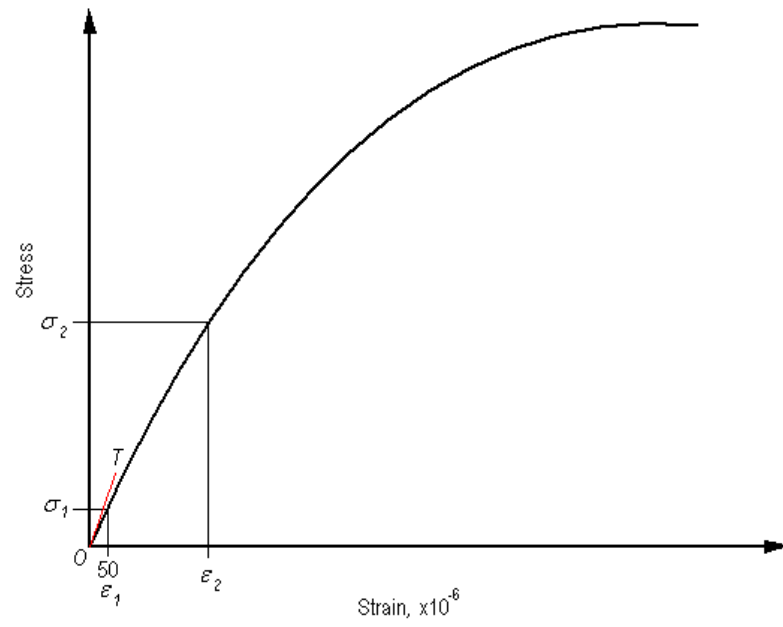
Fig. 7.1. Young's modulus of elasticity

Fig. 7.2. Concrete cylinder instrumented with an extensometer and compressometer

Typical stress-strain curves determined from these measurements for medium strength and low strength concrete at day 1 are presented in Fig. 7.5. Using Eq. 7.4, the static Young's modulus based on the chord modulus was determined. Fig. 7.5 shows that although both high and low strength concrete have a fairly linear stress-strain curve, nonlinearity becomes more prevalent with lower strength concrete. In addition to the chord modulus, the slope of the secant modulus up to a strain value of 0.00005 was calculated and compared to the dynamic Young's modulus. Because of the small variations in the linearity of the stress-strain curve, this small strain secant modulus had a different slope than the chord modulus measured to determine the static Young's modulus (Fig. 7.6).

Before each static modulus test, the cylinder was balanced at its midpoint using a chain and was tested in a free-free condition. An accelerometer was used to record the longitudinal waveform and a small hammer was used as an impact device (Fig. 7.3). The time record measured by the accelerometer was then converted into the frequency domain using a fast Fourier transform (FFT).

A typical frequency plot is presented in Fig. 7.7. Analyzing the data in the frequency domain allows the user to determine the first mode longitudinal frequency by determining the frequency corresponding to the maximum amplitude on the curve. From this frequency peak, the dynamic modulus was calculated using Eqs. (7.5 – 7.6).

$$V_{Rod} = f_l \lambda \tag{7.5}$$

$$E_d = (V_{Rod})^2 \rho \tag{7.6}$$

where: V_{rod} = unconstrained compression wave velocity

f_l = first mode longitudinal frequency

λ = wavelength (2 x specimen length for FFRC measurements)
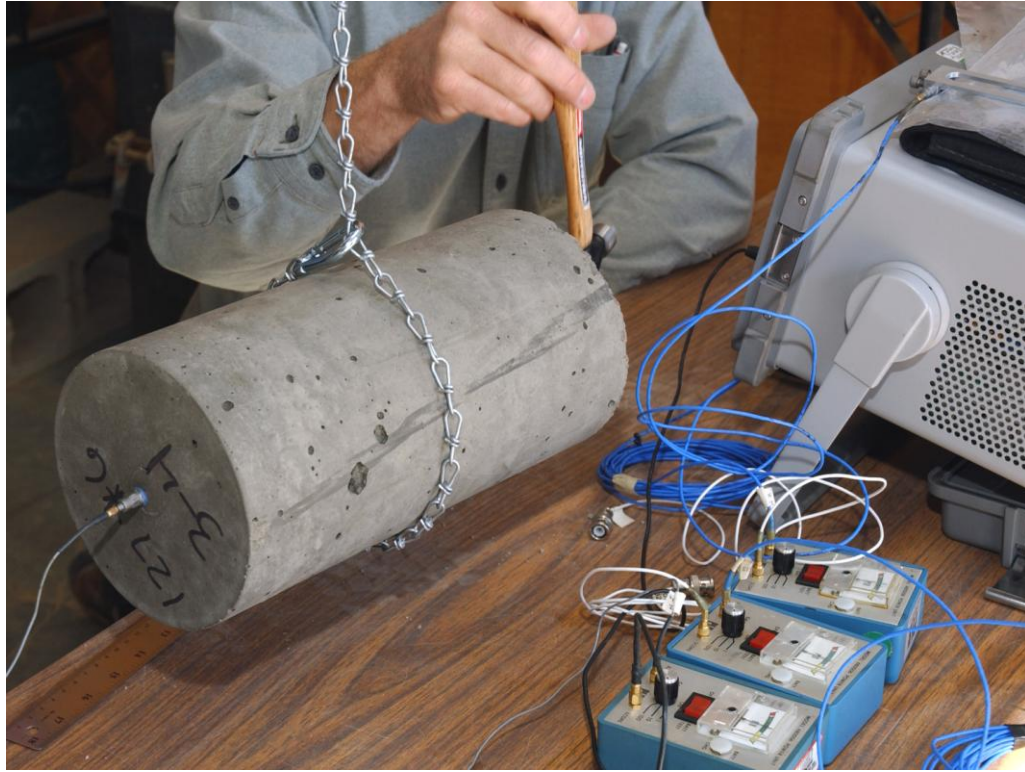
ρ = weight density of the material.

Fig. 7.3. Cylinder tested in free-free condition

Table 7.1. 28 Day Compressive Strengths

Mix	28 Day f'$_c$ (psi)
Low Strength	1880
Medium Strength 1	5350
Medium Strength 2	6102
Medium / High Strength	8920
High Strength	12560
Previous Mix 1	6847
Previous Mix 2	5334
Previous Mix 3	7365

Table 7.2. Mix Designs

Mix	Cement	Fly Ash	Course Aggregate	Fine Aggregate	water	w/c ratio
Low Strength	9.5	0.0	0.0	70.0	4.9	0.51
Low/Medium Strength	12.6	0.0	38.6	34.0	5.4	0.43
Medium Strength 1	10.3	1.9	25.1	29.7	5.0	0.48
Medium Strength 2	15.0	0.0	34.9	29.8	5.5	0.37
Medium / High Strength	13.2	3.3	29.4	19.0	5.2	0.39
High Strength			Proprietary			
Previous Mix 1	17.5	0.0	43.1	40.6	9.0	0.51
Previous Mix 2	19.5	0.0	57.4	57.4	12.1	0.62
Previous Mix 3	29.2	0.0	57.4	49.3	12.0	0.41

Also, the damping ratio of the material was calculated using Eq. (7.7) (Chopra 2003). Damping is defined for a material as a quantity that characterizes the degree of departure from perfect elasticity. Thus, damping is a measure of the plasticity of concrete. Because the damping ratio is typically measured when measuring the dynamic modulus of elasticity, and because it characterizes the material's stiffness, it can be used to convert dynamic to static Young's modulus (Nagy 1997).
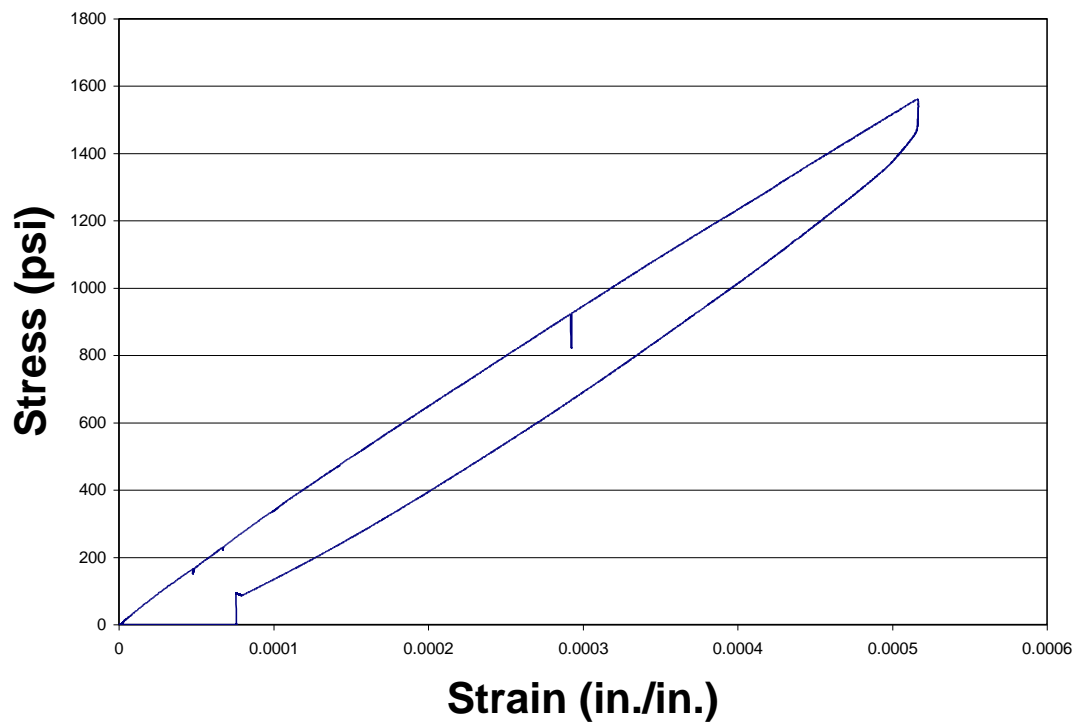
$$\zeta = \frac{f_b - f_a}{f_l} \tag{7.7}$$

where ζ = damping ratio; and f_b-f_a = half power bandwidth.

All measured static and dynamic Young's modulus values are presented in Figs. 7.8 and 7.9, respectively. Each data point represents a measurement on an individual specimen.
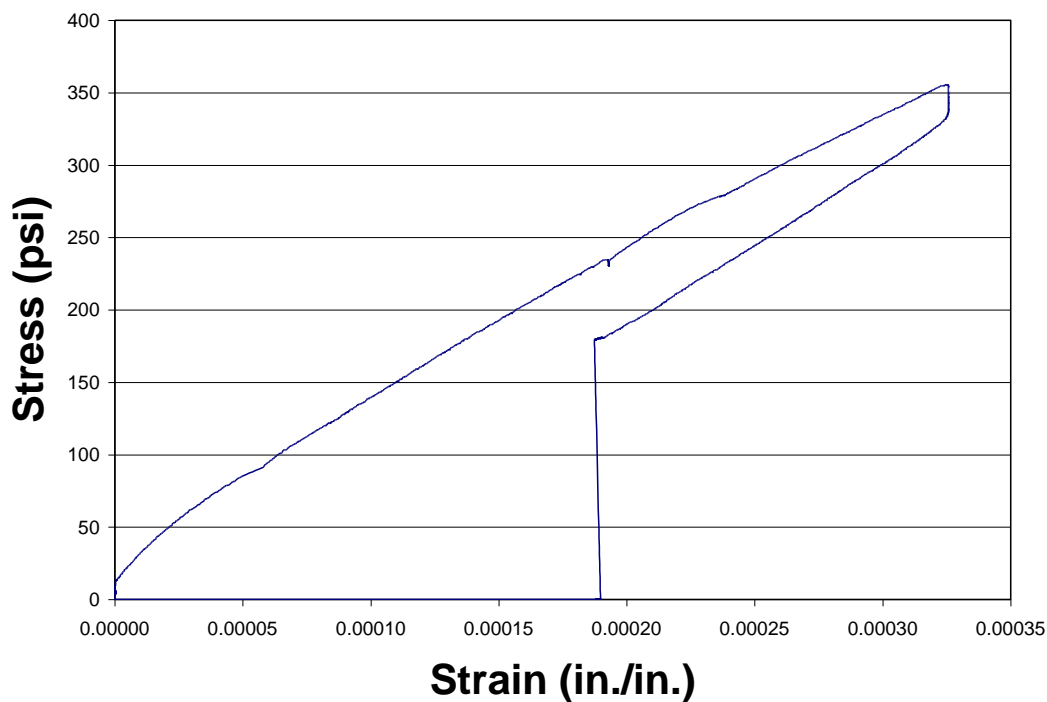
Fig. 7.4. Concrete cylinder instrumented with a compressometer and LVDT

(a) Typical stress-strain curve for medium strength concrete at day 1
Fig. 7.5. Measured stress-strain curves

(b) Typical stress-strain curve for low strength concrete at day 1
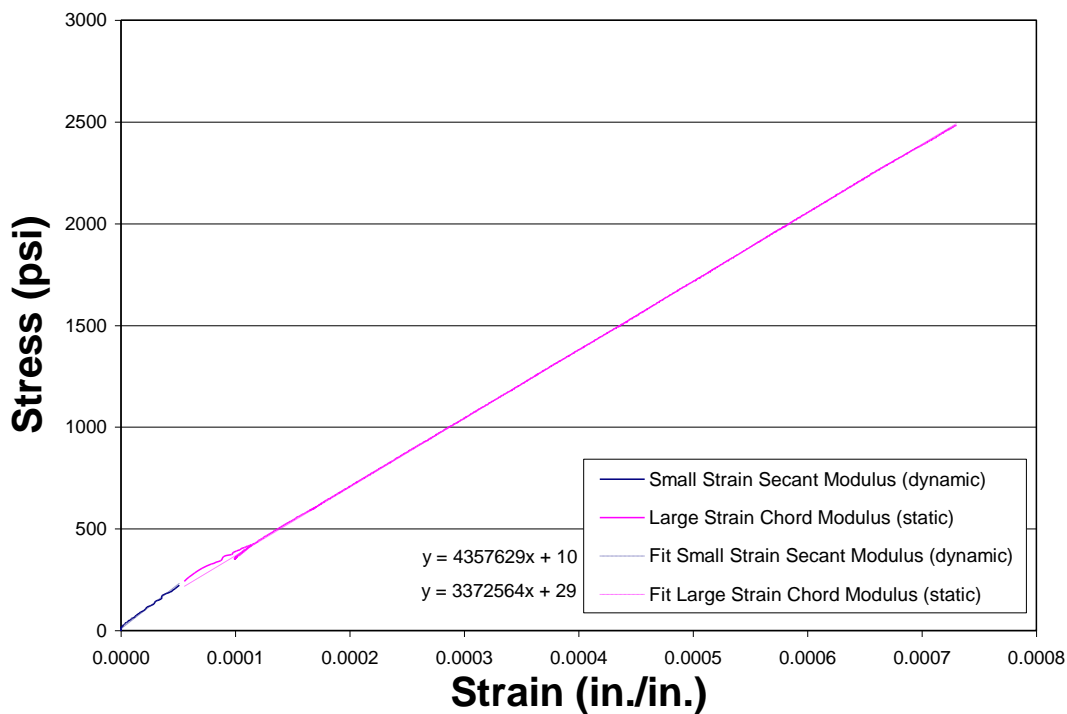**Fig. 7.5.** (continued)

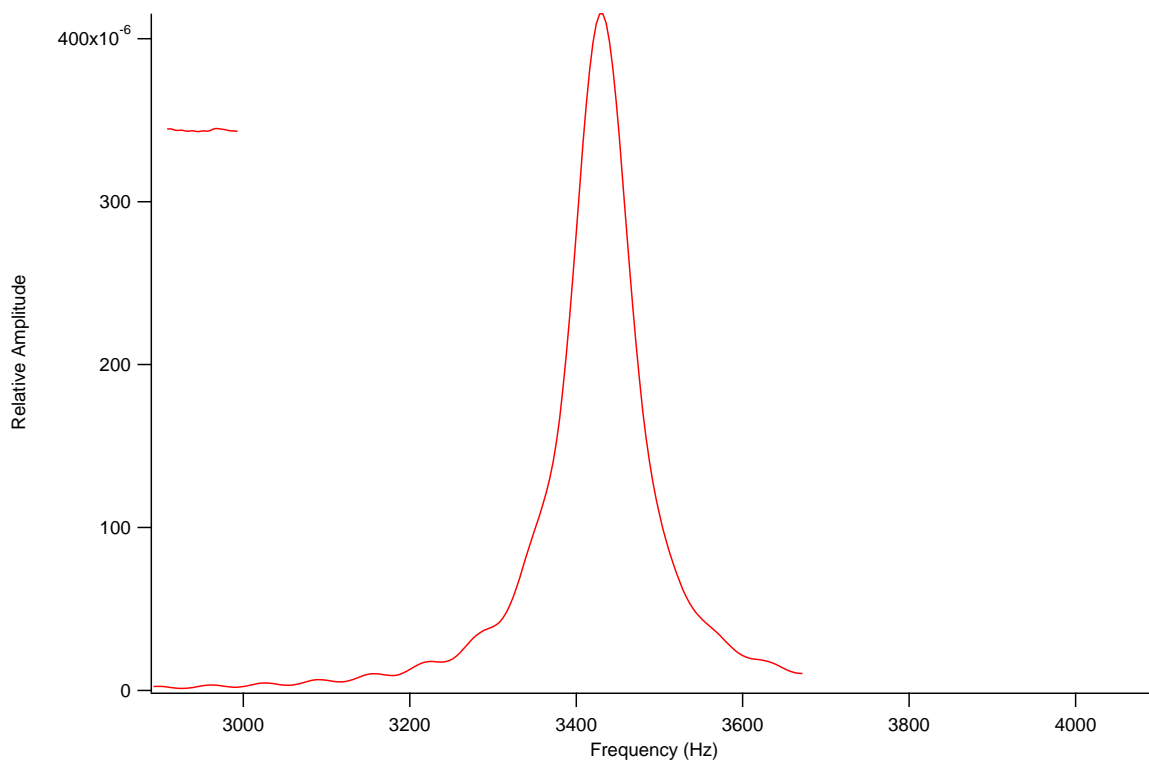**Fig. 7.6.** Measured moduli from static measurement
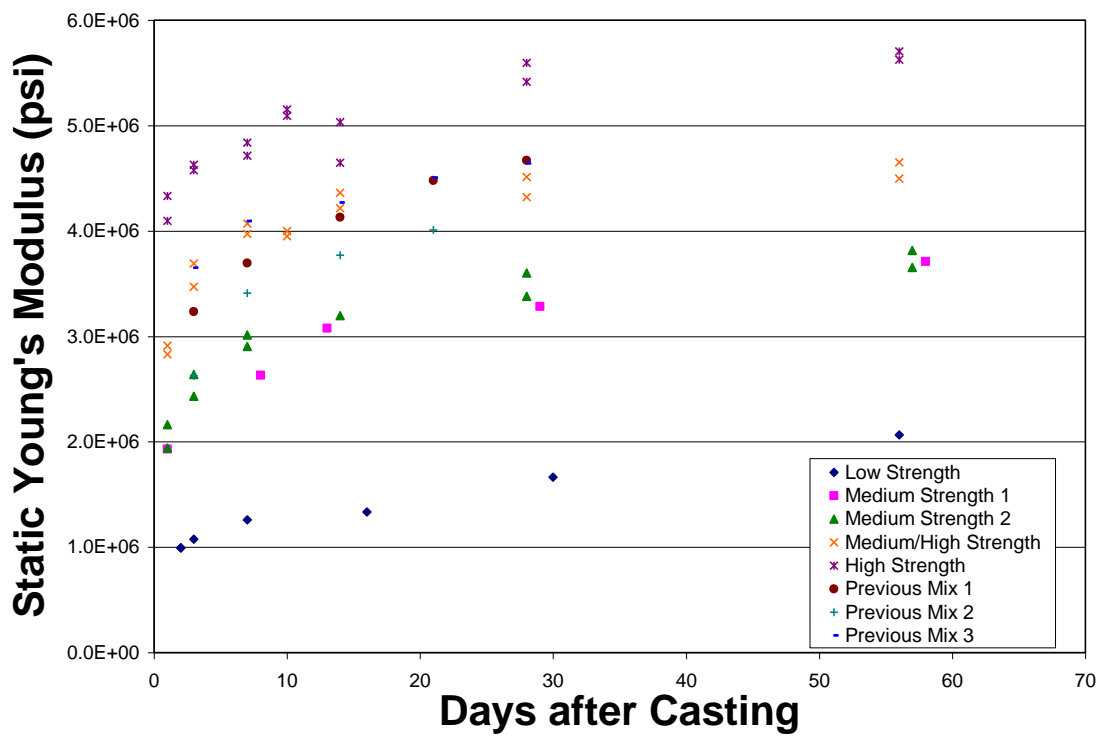
Fig. 7.7. Typical frequency plot

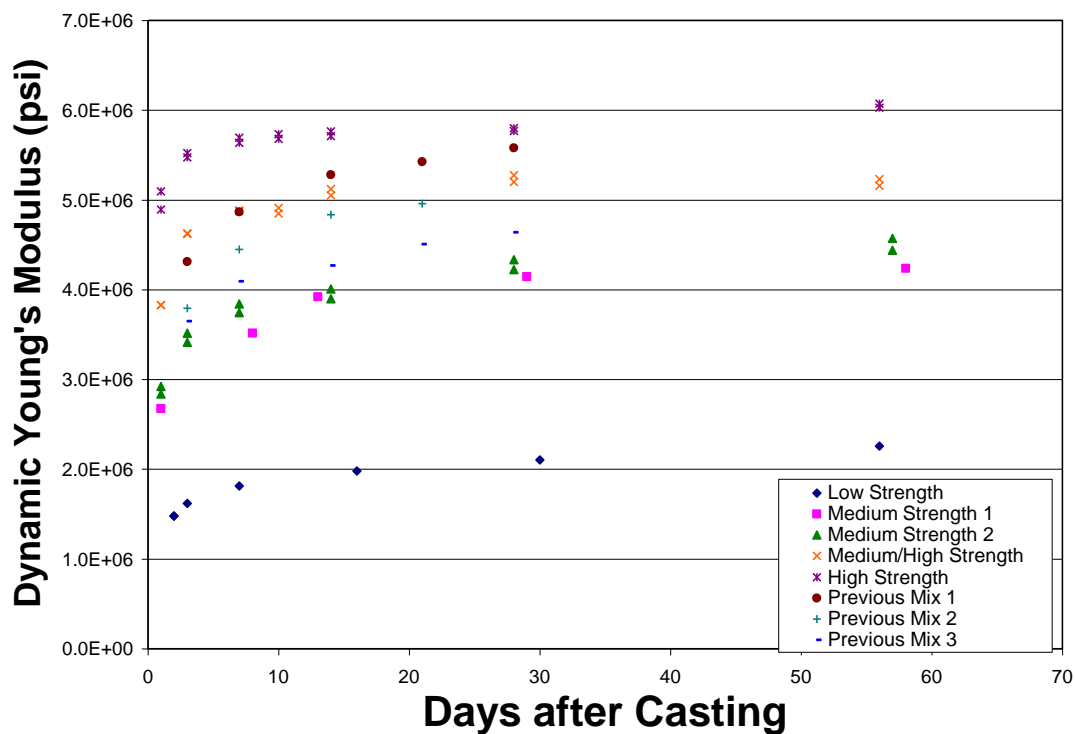**Fig. 7.8.** Measured static Young's moduli as a function of time

Fig. 7.9. Measured dynamic Young's moduli as a function of time

Ratio of Static to Dynamic Young's Modulus

Once the static and dynamic Young's moduli measurements were obtained, the

ratios between the two values were plotted as a function of time (Fig. 7.10). Fig. 7.10

shows that as the compressive strength increases with time, the value of the ratio of static

to dynamic Young's modulus increases. This is consistent with the prior research

presented in the reviewed literature. However, Fig. 7.10 indicates that not only does the

ratio increase as the compressive strength increases with time, but also that higher

strength concretes exhibit higher ratios even at young ages. This indicates that the ratio

must be a function of compressive strength and time. Analyzing the measured data with

regards to the ratio of static to dynamic Young's modulus, strength, and time, the

following formula is proposed:

$$\frac{E_s}{E_d} = 0.04\ln(t) + 1.98 \times 10^{-6} f_{c28} + 0.57 \qquad (7.8)$$

where: t = time in days after casting

f_{c28} = 28 day compressive strength

Calculated values using Eq. (7.8) were compared to the measured values of the ratio of static to dynamic Young's modulus as a function of time. Fig. 7.11 presents all measured values compared to all calculated values determined using Eq. (7.8). A linear regression was performed on the data with a correlation factor of 0.87. Also, the slope of the linear regression is 1.12 indicating that values calculated using Eq. (7.8) correlate very well with measured values of the ratio of static to dynamic Young's modulus. A correlation factor of 1.0 with slope of 1.0 would be a perfect correlation between the two set of data..

Measured values of the damping ratio were also plotted as a function of time (Fig. 7.12). Unfortunately, damping data was not available for the previously tested mixes. Fig. 7.12 shows that the damping ratio decreases as the concrete compressive strength increases indicating that the damping is also a function of compressive strength. The measured dynamic Young's modulus was then plotted as a function of damping ratio (Fig. 7.13). Fig. 7.13 indicates that as the compressive strength of the concrete increases, the dynamic modulus also increases as a function of damping. This agrees with research performed by Nagy (1997). Nagy also showed that the static Young's modulus could be correlated well to the dynamic Young's modulus using values of the damping ratio. However, his study included only two concretes of similar compressive strength. Seely (2005) confirmed this with three mixes of similar compressive strength.
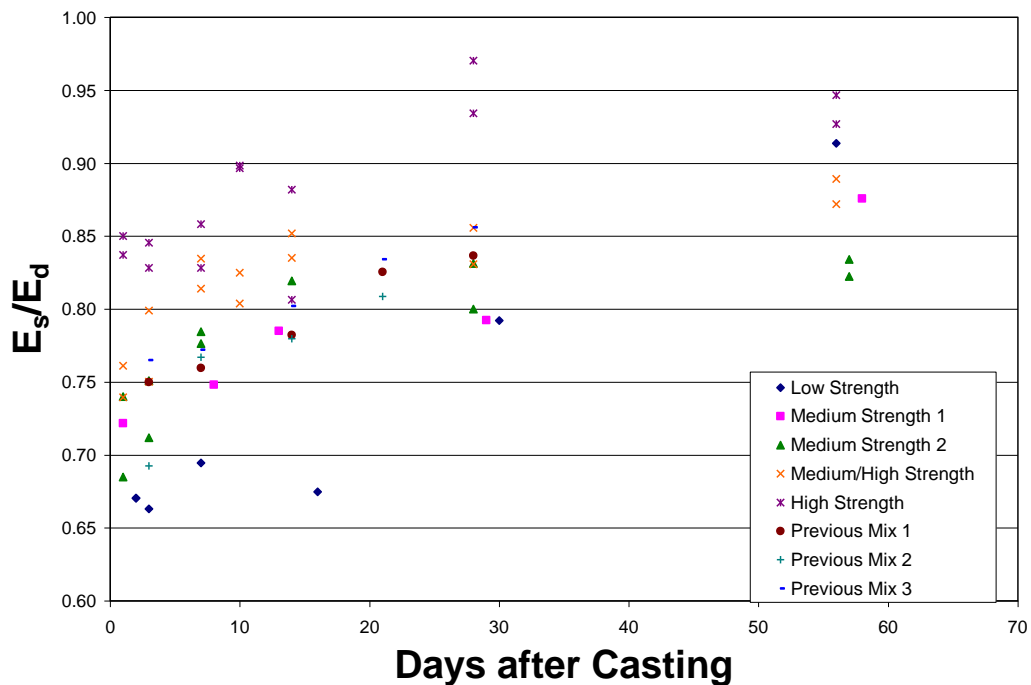
Fig. 7.10. Ratio of static to dynamic Young's modulus (E_s/E_d) as a function of time
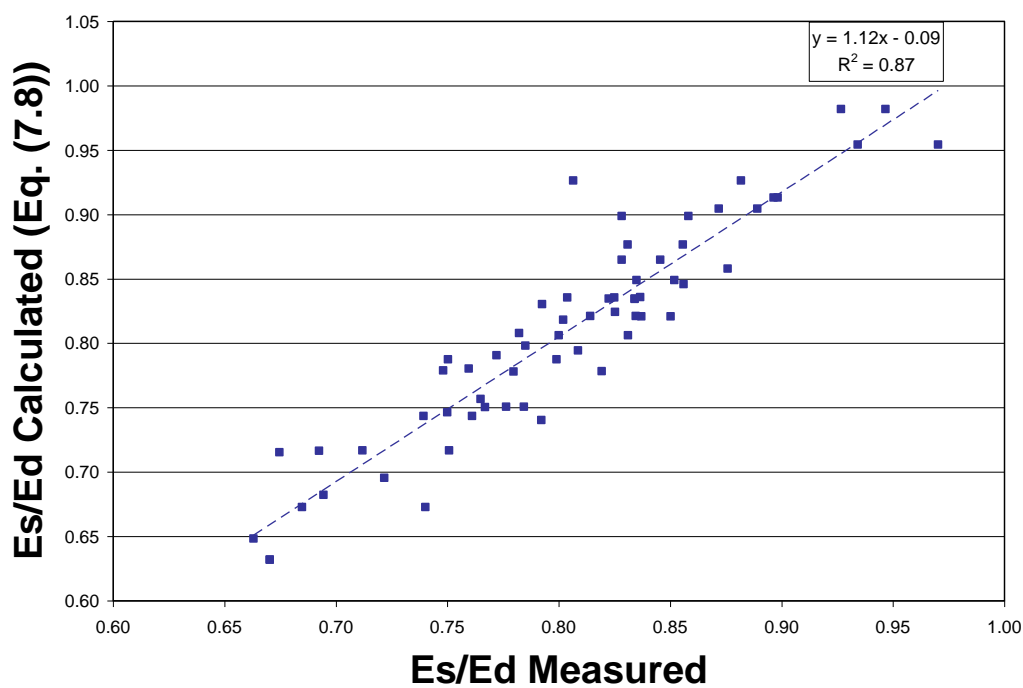

Fig. 7.11. Comparison of measured and calculated values (Eq. (7.8)) of the ratio of static to dynamic Young's modulus for all measurements
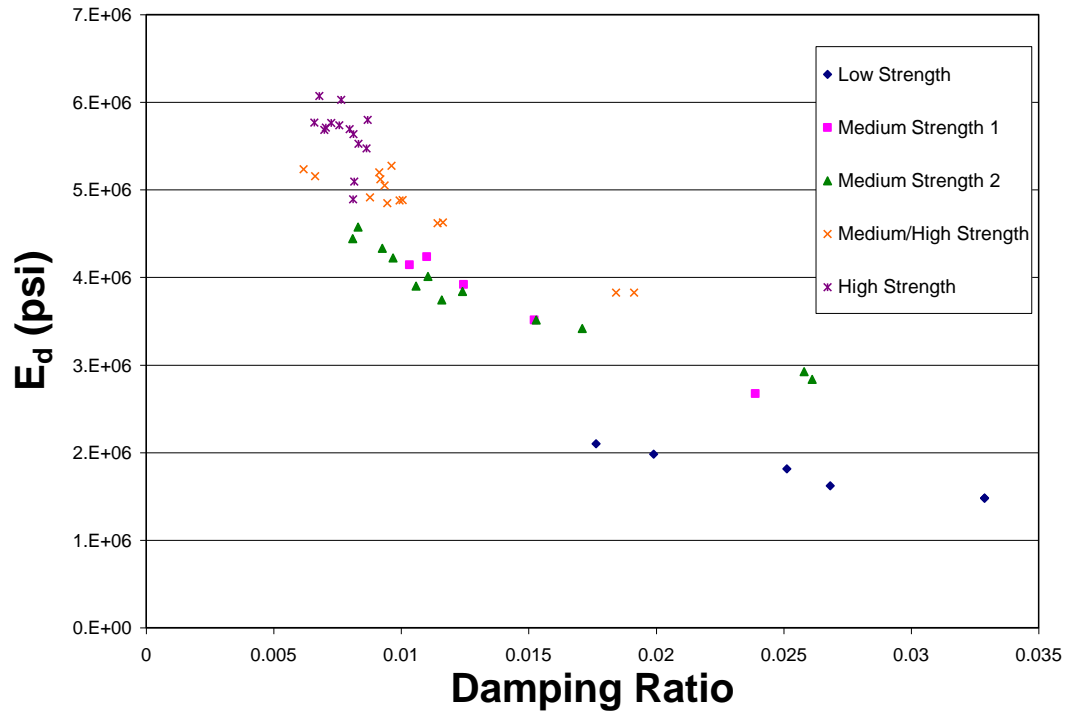
Fig. 7.12. Damping ratio as a function of time
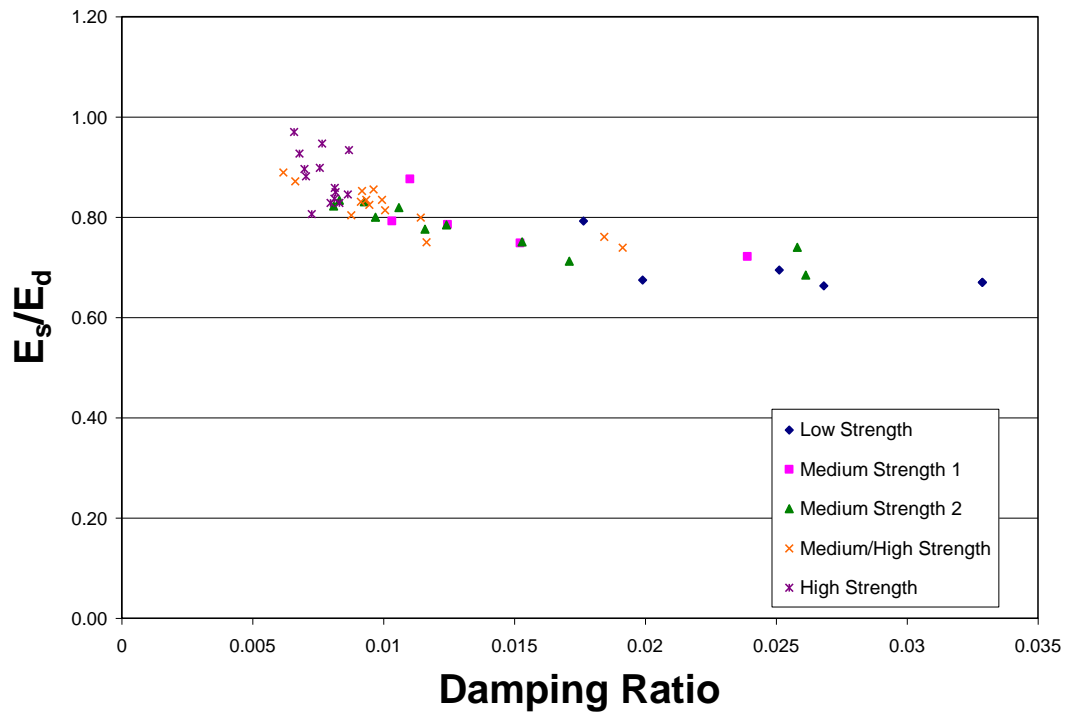
Fig. 7.13. Dynamic Young's modulus as a function of damping ratio

Combining all of the data from the five concrete mixes of varying compressive strengths (Fig. 7.14) allows for the development of the relationship of static to dynamic Young's modulus as a function of damping:

$$\frac{E_s}{E_d} = -9.18\zeta + 0.93 \tag{7.9}$$

This formula confirms previous research results that the ratio of static to dynamic modulus is a function of the damping ratio (Nagy 1997; Seely 2005). Fig. 7.15 presents all measured values compared to all calculated values determined using Eq. (7.9). A linear regression was performed on the data with a correlation factor of 0.72. The slope of the linear regression is 0.73 indicating that values calculated using Eq. (7.9) correlate fairly with measured values of the ratio of static to dynamic Young's modulus.

Fig. 7.14. Ratio of static to dynamic Young's modulus as a function of damping ratio

Fig. 7.15. Comparison of measured and calculated values (Eq. (7.9)) of the ratio of static to dynamic Young's modulus for all measurements

To compare the findings of this study to those of Nagy (1997), the value of α was plotted against compressive strength for all concretes and measurement times (Fig. 7.16). A linear regression was performed on the data and a correlation factor of 0.62 was determined. A formula for α was determined from this plot to relate α to compressive strength:

$$\alpha = 2.12 \times 10^{-6} f_c(t) + 0.19 \tag{7.10}$$

where $f_c(t)$ = compressive strength (psi) at time t.

Previous research included concrete mixes of similar compressive strength and thus did not suggest a strength dependent calculation of α. Substituting Eq. (7.10) into Eq. (7.1) leads to a modified version of the equation suggested by Nagy based on a time dependent compressive strength:

$$E_s = \frac{E_d}{1 + \eta^{2.12 \times 10^{-6} f_c(t) + 0.19}} \qquad (7.11)$$

Rearranging Eq. (7.11) gives:

$$\frac{E_s}{E_d} = \frac{1}{1 + \eta^{2.12 \times 10^{-6} f_c(t) + 0.19}} \qquad (7.12)$$

Using Eq. (7.12), a value for the ratio of static to dynamic Young's modulus can be calculated as a function of time dependent compressive strength. Fig. 7.17 presents all measured values compared to all calculated values determined using Eq. (7.12). A linear regression was performed on the data with a correlation factor of 0.83. However, the slope of the linear regression was 0.32 indicating that values calculated using Eq. (7.12) are not correlated well with measured values of the ratio of static to dynamic Young's modulus.
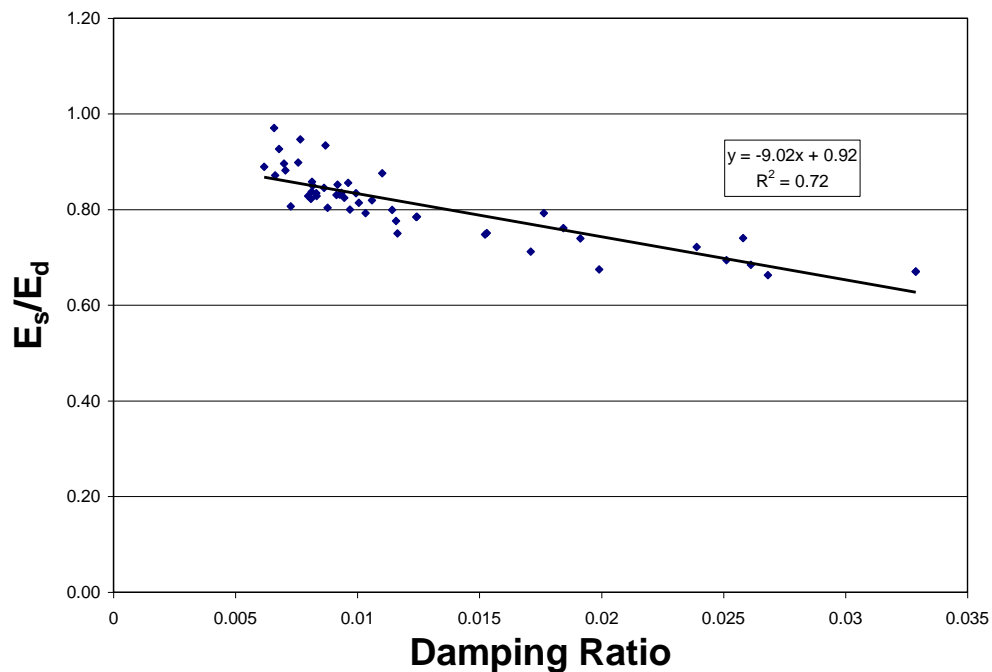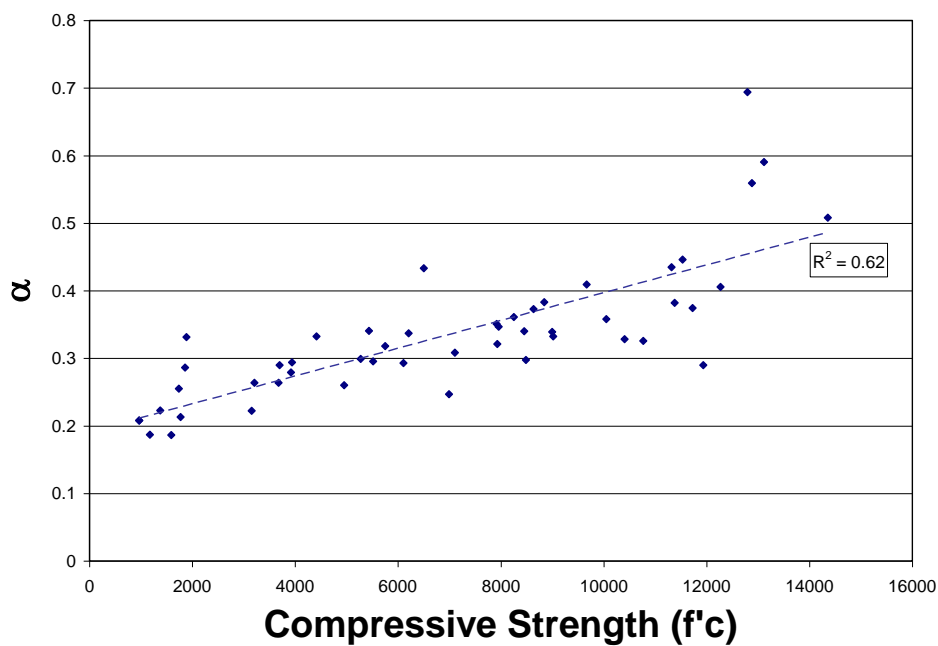

Fig. 7.16. α as a function of compressive strength

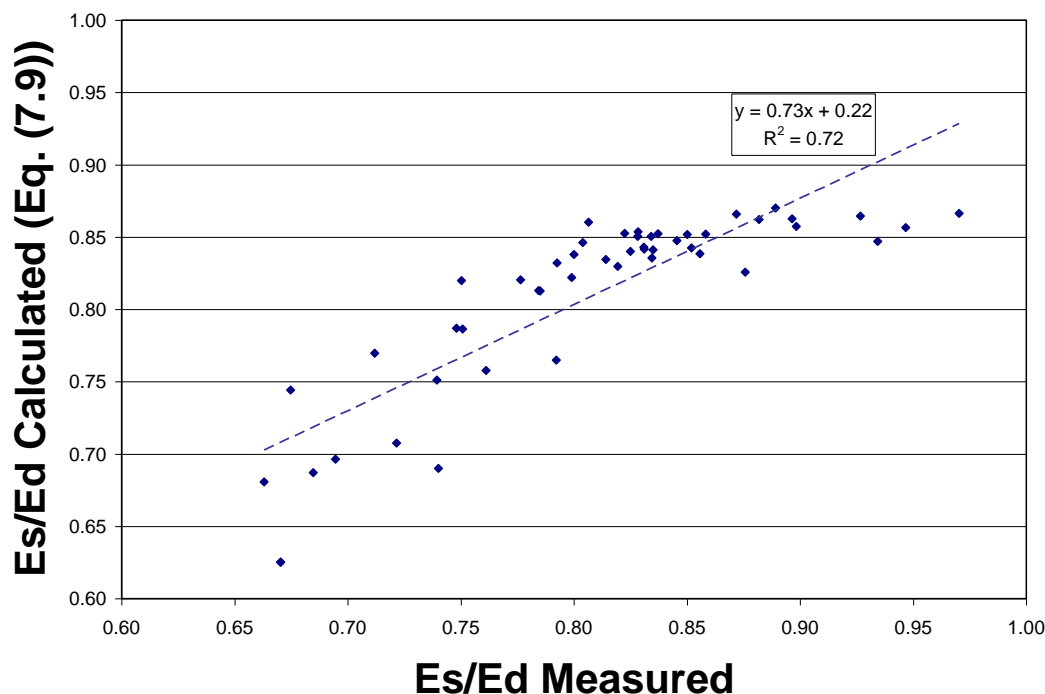**Fig. 7.17.** Comparison of measured and calculated values (Eq. (7.12)) of the ratio of static to dynamic Young's modulus for all measurements

Finally, values of the ratio of static to dynamic Young's modulus were calculated

using Eqs. (7.2 -7.3) (Figs. 7.18-7.19). Fig. 7.18 presents all measured values compared

to all calculated values determined using Eq. (7.2). A linear regression was performed on

the data with a correlation factor of 0.79. The slope of the linear regression was 1.60

indicating that values calculated using Eq. (7.2) are fairly correlated with measured

values of the ratio of static to dynamic Young's modulus. Fig. 7.19 presents all measured

values compared to all calculated values determined using Eq. (7.3). The correlation

factor determined from data calculated using Eq. (7.3) is 0.75 and the slope of the linear

regression is 1.08. Aside from the values of the ratio of static to dynamic Young's

modulus calculated using Eq. (7.8), the values calculated using Eq. (7.3) are the closest to

the measured values. This indicates that the equation derived by Han and Kim (2004) is

a very good indicator of measured values and that the proposed Eq. (7.8) is the best

indicator of measured values.

Comparison of Various Moduli

The strains induced on a concrete specimen during a FFRC test are typically on

the order of 0.001 percent or less (Stokoe et al. 1994). The strain induced on the concrete

specimens was calculated (Eq. (7.12)).

$$\varepsilon = \frac{\ddot{u}}{2\pi f_n V_{rod}}$$ (7.12)

where: ε = Average strain measured during a FFRC test

$\ddot{u}$ = Acceleration at f_l
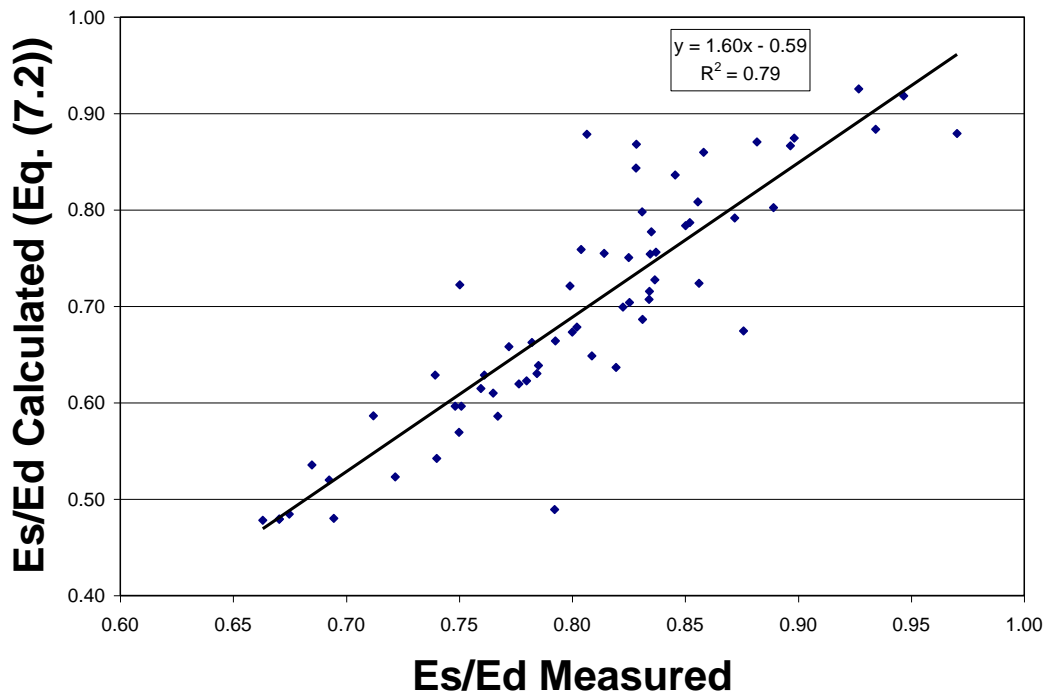
Fig. 7.18. Comparison of measured and calculated values (Eq. (7.2)) of the ratio
of static to dynamic Young's modulus for all measurements
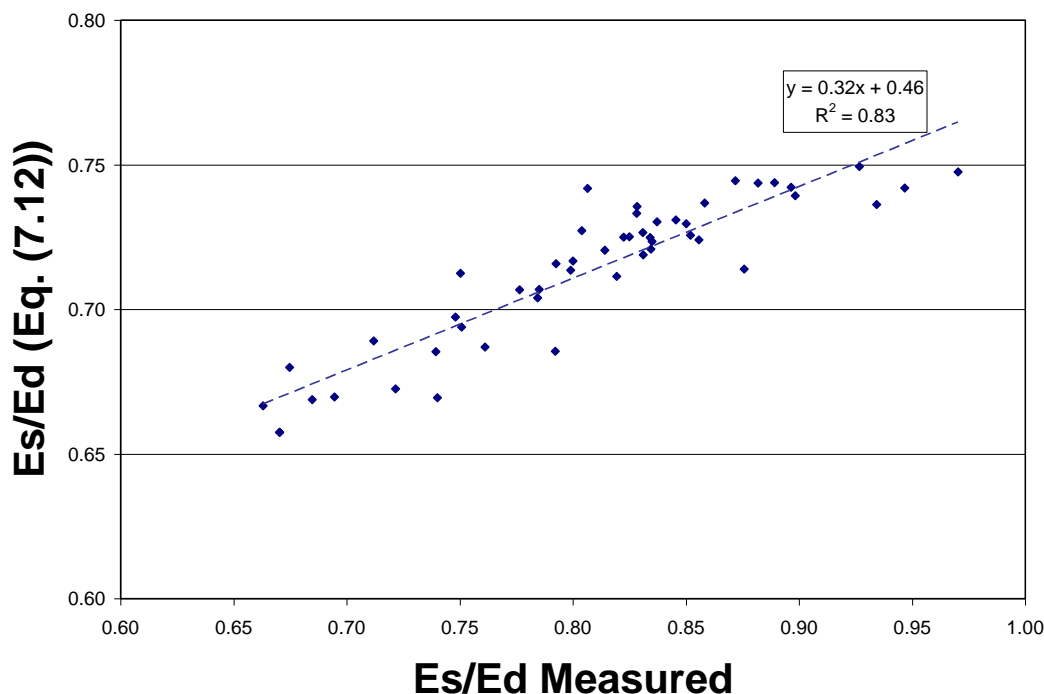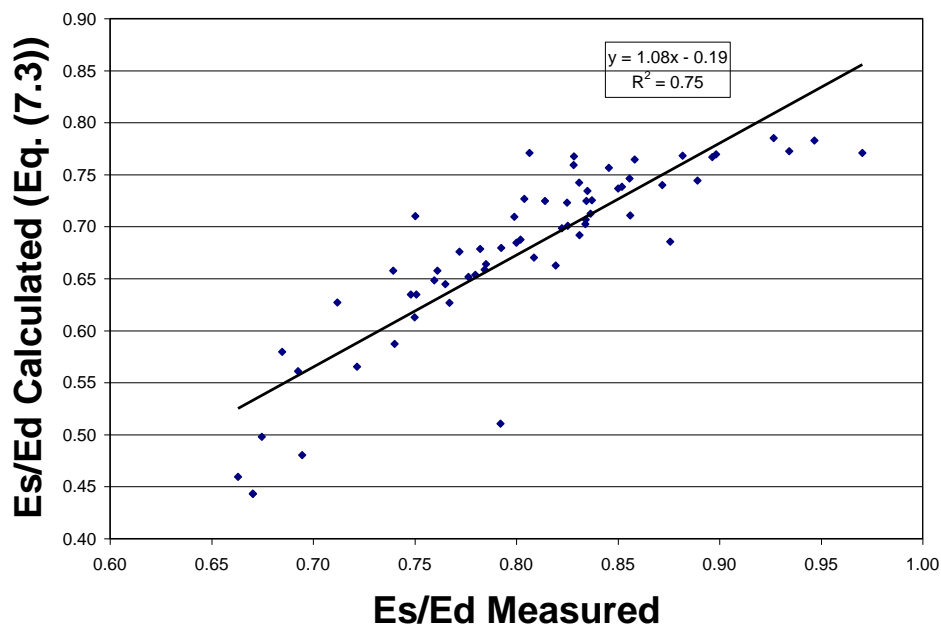
Fig. 7.19. Comparison of measured and calculated values (Eq. (7.3)) of the ratio of static to dynamic Young's modulus for all measurements

Ten calculations were made to determine an approximate maximum value of strain induced during a FFRC test. Of the strain values calculated, the maximum value of strain was approximately 10×10^{-12}.

Figure 7.6 presents the measurement differences between a small strain secant modulus and a large strain chord modulus. The slope of the small strain secant modulus on all static stress-strain curves from all tested cylinders was determined. Fig. 7.20 presents the ratio of the small strain secant moduli to the dynamic Young's moduli determined using the FFRC method. Fig. 7.18 shows that the small strain secant moduli determined correlate well with the dynamic Young's moduli measured using the FFRC method differing by a maximum of 8% and an average of 3%. Although the maximum strain induced during a FFRC test is on the order of 10×10^{-12}, the small strain secant modulus also gives a good measurement of dynamic Young's modulus.
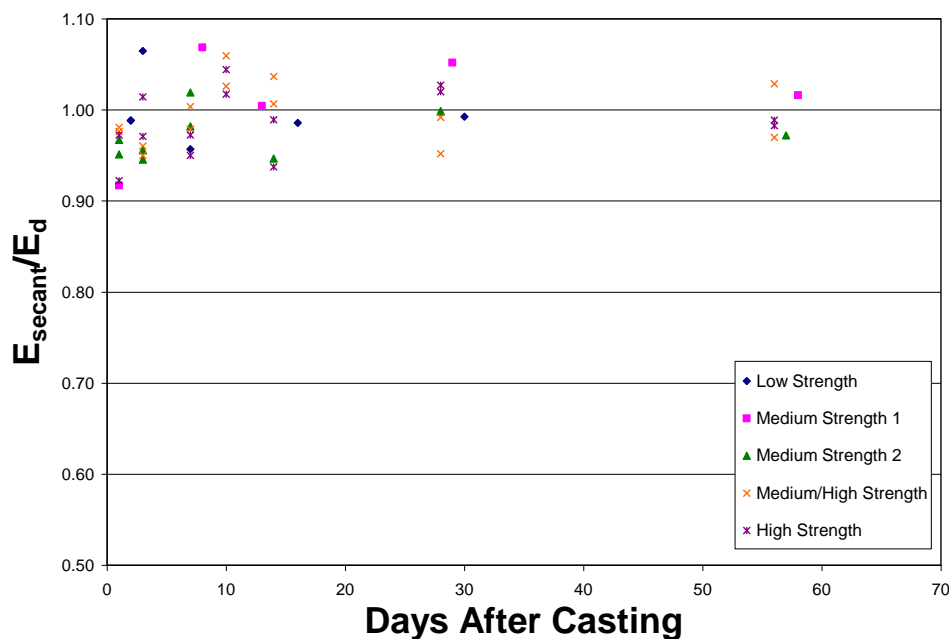
Fig. 7.20. Ratio of small strain secant modulus to dynamic Young's modulus as a function of time

Conclusions

The variation in the ratio of static to dynamic Young's modulus as a function of compressive strength, time, and damping ratio was studied. Eight concrete mixes ranging in compressive strengths from 1880 psi to 12560 psi were tested for static Young's modulus, dynamic Young's modulus, damping ratio, and strength as a function of time. Several equations to relate the ratio of static to dynamic Young's modulus to factors of strength and damping were developed and compared. Results indicate that:

1. Calculated values using a developed equation comparing static to dynamic Young's modulus based upon time dependent compressive strength were compared to the measured values of the ratio of static to dynamic Young's modulus. A linear regression was performed on the data with a correlation factor of 0.87. Also, the slope of the linear regression is 1.12 indicating that

values calculated using this equation correlate very well with measured values of the ratio of static to dynamic Young's modulus.

2. Calculated values using a developed equation comparing static to dynamic Young's modulus based upon damping were also compared to the measured values of the ratio of static to dynamic Young's modulus. A linear regression was performed on the data with a correlation factor of 0.72. The slope of the linear regression is 0.73 indicating that values calculated using Eq. (7.9) correlate fairly with measured values of the ratio of static to dynamic Young's modulus.

3. A formula proposed by previous research was modified to depend on factors of compressive strength and damping. The formula was originally designed to be dependent only on damping. A linear regression was performed on the data with a correlation factor of 0.83. However, the slope of the linear regression was 0.32 indicating that values calculated using this equation are not correlated well with measured values of the ratio of static to dynamic Young's modulus.

4. Two other formulas determined by previous research were used to compare to measured data. Linear regressions fitting data calculated using these equations had correlation factors of 0.79 and 0.75, respectively. The slopes of the fitted lines were 1.60 and 1.08, respectively, for data calculated using the two formulas.

5. Because a correlation factor of 1.0 with slope of 1.0 would be a perfect correlation between calculated and measured ratios of static to dynamic

Young's modulus, conclusions 1-4 indicate that the ratio of static to dynamic Young's modulus can most precisely be determined from factors of compressive strength and time using the equation proposed (Eq. (7.8)) by this study.

6. A small strain secant modulus measured up to strains of 0.00005 on the statically measured stress-strain curve correlate well with the dynamic Young's moduli measured using the free-free resonant column method differing by a maximum of 8% and an average of 3%. This indicates that an initial secant modulus, rather than an initial tangent modulus, may more accurately predict the value of the dynamic Young's modulus.

CHAPTER 8

CONCLUSION

Summary

The objective of this research was to provide a more complete understanding

of the dynamic material properties of concrete and to develop new testing equipment,

new experimental and analytical techniques, and an expanded knowledge to the

extent of which the methods of stress wave propagation can be used. As such, several

new and improved methods of analysis were developed along with new equipment to

aid in those techniques. Newly developed and existing concrete materials were tested

in parallel to determine behavior characteristics under a variety of loading and

boundary conditions. Finally, improved methods of analysis were proposed to further

the understanding of material behaviors under a variety of strains.

Combined Stress Wave Propagation
Method

A newly proposed method named the Combined Stress Wave Propagation

(CSWP) method was developed and presented. This method combines the existing

methodology and testing techniques of the spectral analysis of surface waves, impact

echo, and free-free resonant column techniques. The proposed method involves

performing both SASW and IE measurements simultaneously making a more efficient

field experiment than by performing the two techniques independently. Simultaneously,

the free-free resonant column (FFRC) method can be used to calculate Poisson's and

damping ratios so that no material property assumptions must be made during the final analysis of data.

A concrete tunnel lining was modeled as a three layer slab of varying depths and stiffness. Final analysis of the concrete tunnel lining model showed that SASW, IE, and DPW measurements correlate within 3% for both P-wave velocities and depth. The location and depth of the five voids were identified.

Combining the SASW and IE procedures into one testing procedure provided a much more efficient field experiment. Data was measured using the CSWP method that would not have been provided by performing the SASW or IE tests and analysis independently. This study indicates that the CSWP method is an extremely efficient and effective tool to analyze in-place properties of concrete tunnel linings and that it could be extended for use on other concrete structures. It is useful to determine the in-place properties of the materials within the tunnel lining and also in determining the location of voids within the concrete or underlying bedrock. The method is more efficient than performing SASW and IE alone, and by incorporating FFRC testing, no material properties must be assumed.

Proposed Damage Model

Unconstrained compression waves were used to determine the variation in first mode longitudinal frequency and damping ratio as a function of cyclic loading to failure. The amount of energy absorbed by individual concrete specimen was calculated from hysteretic curves measured during testing. Several concrete mixes were sampled to include a variety of compressive strengths. The first mode longitudinal frequencies were

shown to decrease to a range of 88.5% to 93.3% of their initial, undamaged frequency. Higher strength concretes exhibited less percentage loss of initial frequency. Measurements of total cumulative energy were shown to correlate with percentages of failure within 4.7%. Also, higher strength concretes exhibited an ability to absorb more energy through modes other than the formation of microcracks.

A proposed damage model was developed involving the use of compressive strength, frequency, and energy. This model was shown to correlate with measured values within 7%. Also, the proposed model showed to have a fair correlation when compared to damage index models from existing literature. Variation in first mode longitudinal frequency and total energy accumulation showed to be excellent indicators of damage in cyclically loaded concrete specimens of varying strength.

The equation developed during this study is better than any other equation existing in current literature.

A Comparison of Prestress Loss in a Three-Span Prestressed Concrete Bridge Made with High Performance Self Consolidating Concrete

A study was performed to measure the behavior of six, high performance, self-consolidating concrete (HPSCC), prestressed bridge girders using embedded vibrating wire strain gages (VWSG). Measurements were made on material specimens of the HPSCC used to make the bridge girders. The measured strains for the VWSGs were used to determine prestress losses that were compared to calculated values obtained using the 2004 and 2007 AASHTO LRFD Specifications.

Values calculated for the compressive strength using ACI 318-05 (Eq. (1) in this study) were approximately 31.7% smaller than the measured values at day 1. This under estimation grew smaller as a function of time and by day 56 the measured and calculated values correlated within 1%. Values of static Young's modulus calculated with ACI 318-05 (Eq. (2) in this study) varied from approximately 29% smaller to 21% larger than the measured values on days 1 and 56, respectively. However, values of static Young's modulus calculated suggested by ACI committee 209 (Eq. (6.3) in this study) were approximately 27% smaller at day 1, but within a 2% correlation on days 7, 28, and 56. Shrinkage strains calculated in accordance with AASTHO LRFD Specifications (Eq. (6.4) in this study) were approximately 40% smaller than the average measured value at day 7 and 1% and 11% at days 28 and 56, respectively.

The average measured prestress losses after the deck was cast were 29.8 ksi and 16.1 ksi corresponding to approximately 14.7% and 8.0% of the initial jacking stress of 202.5 ksi for the 132.2 ft. and 82.2 ft. girders, respectively. Among both the 132.2 ft. and 82.2 ft. girders, the variation in measured prestress was a maximum of 8%. AASHTO LRFD 2007 Specifications over predicted the total prestress loss by 6.3% and 25.0% for the 132.2 ft. and 82.2 ft. girders, respectively. In contrast, the best predictions calculated using the AASHTO LRFD 2004 Specification were 17.1% and 60.5% overestimates of the total prestress losses measured for the 132.2 ft. and 82.2 ft. girders, respectively. AASHTO LRFD 2007 Specifications under estimated values of elastic shortening by 20.9% and 8.3% for the 132.2 ft. and 82.2 ft. girders, respectively. The calculated values of prestress loss due to creep and shrinkage were overestimated by all design specifications. The AASHTO LRFD 2007 Specifications did the best job and

over predicted the losses due to shrinkage and creep for the 132.2 ft. and 82.2 ft. girders by 76.3% and 67.2%, respectively.

All AASHTO LRFD Specifications under estimated the measured elastic shortening losses and overestimated the total long term losses measured. This study showed that design practices are improving, and that prestress losses for high strength self-consolidating concrete can be predicted with them.

Static and Dynamic Young's Modulus

The measurement techniques and methodology of static and dynamic Young's modulus have consistently been debated upon in literature. Existing literature agrees that the dynamic modulus measured using nondestructive techniques is equal to an initial tangent modulus drawn on a stress-strain curve for concrete in uniaxial compression. A study was performed to determine the ratio of static to dynamic Young's modulus and initial tangent modulus to dynamic modulus. A new method to determine the dynamic Young's modulus from static measurements was proposed.

Studies of several concrete mixes show that the ratio of static to dynamic Young's modulus varies between approximately 65% and 95%. This ratio also varies with time and as a function of concrete strength. This result agrees with existing literature.

The initial tangent moduli of statically measured stress-strain curves exceed all dynamic Young's moduli measured using nondestructive techniques by approximately 200% or greater. This result indicates that the assumption previously made that the dynamic Young's modulus measured using nondestructive techniques is equal to an initial tangent modulus of a stress-strain curve is incorrect.

A new method was proposed to determine the dynamic Young's modulus from a statically measured stress-strain curve. Young's moduli determined from this method differ from those values measured using nondestructive techniques by a maximum of 13% and an average difference of only 4%. This method proved to be the best existing method to determine the ratio of Static to Dynamic Young's modulus using factors of compressive strength, damping, and time.

Conclusions and Recommendations

This dissertation investigated the use of nondestructive methods to develop new understandings of concrete materials and the loading conditions to which they are subjected. This research represents just a small work in the uncountable studies that have been performed and that should continue to be investigated to evaluate concrete structures nondestructively. There is always variability in concretes, and to say that a specific type of concrete is understood completely is incorrect. Prediction criteria can always be improved, and to be able to analyze structures nondestructively and compare the results with predicted values allows for this type of improvement. The ability to measure a concrete structure's in-place physical properties and use known methods to quantitatively assess the condition of the structure is invaluable. The methods and techniques of nondestructive testing of concrete allow for these types of improvements. In order to continue to develop the understanding of the in-place physical properties of concrete structures, the research and development of nondestructive testing of concrete must continue to move forward.

A better method of determining concrete profiles of varying stiffness and

identifying the location of embedded flaws was developed. This combined stress

wave propagation method is better than performing individual measurements. It takes

less time to perform the experimental work, and the analysis is made easier because

of the combination. In order to improve the understanding of concrete fatigue, an

equation was developed and proved to be the most accurate equation among other

existing equations to determine the damage of concrete specimen. Also, an equation

to understand the relationship between static and dynamic moduli was developed and

proved to provide more accurate results with regards to the ratio of static to dynamic

Young's modulus than any other equation in existing literature.

A high performance concrete made from self-consolidating concrete was tested

and proved to be unlike any other concrete ever manufactured. Using this incredible

material, prestressed bridge girders were fabricated and instrumented to measure the

change in prestress losses as a function of time and loading. AASHTO LRFD Design

Specifications were used to determine these losses and the most accurate method was

revealed. It was determined that although these design specifications most accurately

calculated the prestress losses, they would be improved by further developing the

equations for prestress losses related to creep and shrinkage effects.

In order to move forward, nondestructive methods must be used more. More

structures need to be instrumented to determine in-place properties. This is important not

only to improve design specifications, but also to allow engineers to be able to quantify

in-place properties. Although the methods to do this are in place, the existing

instrumentation is bulky and hard to use. It is thus important to develop new, easier to

use, instrumentation. This will allow and promote the use of nondestructive testing on structures, and simultaneously allow for the improvement of design specifications.

Engineers need more exposure to the vast world of nondestructive testing of materials. Although this dissertation dealt exclusively with the nondestructive testing of concrete, the experimental methods and analysis techniques can be used on virtually any material. Engineers should have some knowledge of these methods and techniques. Courses should be offered at universities and inspection engineers, especially, should be required to have an extensive knowledge of these methods.

Finally, it is vital that the equations proposed in this study be further developed and used in engineering. The equations for damage quantification and determination of static to dynamic moduli have an incredible potential to help engineers understand the properties of in-place structures. By performing further research on more concrete samples varying in mix design, these equations could be fine tuned, standardized, and used to help make structures safer.

REFERENCES

Ahlborn, T. M., French, C. E., and Leon, R. T. (1995). "Applications of High-Strength Concrete to Long-Span Prestressed Bridge Girders." *Transportation Research Record. 1476*, Transportation Research Board, Washington, D.C. 22-30.

Alliche, A., and Francois, D. (1989). *Fatigue Damage of Concrete, Fracture of Concrete and Rock*, Springer-Verlag, New York,

AASHTO. (1989). *Standard Specifications for Highway Bridges*, 14th Ed., AASHTO, Washington, D.C.

AASHTO. (2004). *LRFD Bridge Design Specifications*, 3rd Ed., AASHTO, Washington, D.C.

AASHTO. (2007). *LRFD Bridge Design Specifications*, 4th Ed., AASHTO, Washington, D.C.

ASTM. (1998). "Standard Test Method for Measuring the P-Wave Speed and the Thickness of Concrete Plates Using the Impact Echo Method." ASTM Designation: C 1383, West Conshohocken, PA.

ASTM. (2002). "Standard Test Method for Fundamental Transverse, Longitudinal, and Torsional Resonant Frequencies of Concrete Specimens." ASTM Designation: C 215, West Conshohocken, PA.

ASTM. (2002). "Standard Test Method for Static Modulus of Elasticity and Poisson's Ratio of Concrete in Compression." ASTM Designation: C 469, West Conshohocken, PA.

ASTM. (2005). "Standard Test Method for Slump Flow of Self-Consolidating Concrete." ASTM Designation: C 1611, West Conshohocken, PA.

ASTM. (2003). "Standard Practice for Making and Curing Concrete Test Specimens in the Field." ASTM Designation: C 31, West Conshohocken, PA.

Bahn, B., and Hsu, C. T. (1998). "Stress-Strain Behavior of Concrete under Cyclic Loading." *ACI Materials J.*, 95 (2), 178-193.

Barr, P. J., Kukay, B..M., and Halling, M. W. (2007). "Comparison of Prestress Losses for a Prestress Concrete Bridge Made with High Performance Concrete." In Press.

Bay, J. A., and Stokoe, K. H. (1990). "Field Determination of Stiffness and Integrity of PCC Slabs using the SASW Method." *Proc., Nondestructive Evaluation of Civil Structures and Materials*. 71-86.

Bay, J. A., and Stokoe, K. H. (1992). "Field and Laboratory Determination of Elastic Properties of Portland Cement Concrete Using Seismic Techniques." *Transportation Research Record. 1355,* Transportation Research Board, Washington, D.C. 67-74.

Bonen, D., and Shah, S. P. (2004). "Fresh and hardening properties of self-consolidating concrete." *Progressive Structural Engineering Materials*, 7, 14-26.

Boone, S. D. (2005). "Dynamic Properties of a Mass Concrete Fill." MS Thesis, The Univ. of Tennessee, Knoxville.

Carino, N. J., Sansalone, M., and Hsu, N. (1986). "A Point Source-Point Receiver, Pulse-Echo Technique for Flaw Detection in Concrete." *Proc., ACI J.*, 83(2), 199-208.

Cheng, C., and Sansalone, M. (1995). "Determining the Minimum Crack Width that can be Detected Using the Impact-Echo Method." *Materials and Structures*, 28, 125-132.

Cho, Y. S. (2003). "Non-destructive Testing of High Strength Concrete Using Spectral Analysis of Surface Waves." *NDT&E International,* 36, 229-335.

Cho, Y. S. (2005). "Spectral Analysis of Surface Waves in Single and Multi-Layer Slabs with Finite Thickness using Finite Element Modeling." *NDT&E International*, 38, 195-202.

Chopra, A. K. (2003). *Dynamics of Structures*, Pearson Education, Inc., Singapore.

Cole, H. A. (2000). "Direct Solution for Elastic Prestress Loss in Pretensioned Concrete Girders." *Practice Periodical on Structural Design and Construction*, 5, 27-31.

Dziewonski, A. M., Bloch, S., and Landisman, M. (1969). "A Technique for the Analysis of Transient Seismic Signals." *Bull. Seismol. Soc. Am.*, 59, 427-444.

Gao, L., and Hsu, C. T. (1998). "Fatigue of Concrete under Uniaxial Compression Cyclic Loading." *ACI Material J.*, 95(5), 575-581.

Garstka, B., Kratzig, W. B., and Stangenberg, F. (1993). "Damage Assessment in Cyclically Loaded Reinforced Concrete Members." *Proc., Second EURODYN*, pp. 121-128

Gettu, R., Aguado, A., and Oliveira, M. F. (1996). "Damage in High-Strength Concrete Due to Monotonic and Cyclic Compression - A Study Based on Splitting Tensile Strength." *ACI Materials J.*, 93(6), 519-523

Gheorghiu, C., Rhazi, J. E.; and Labossiere, P. (2005). "Impact Resonance Method for Damage Detection in RC Beams Strengthened with Composites." *Proc. of SPIE – The International Society for Optical Engineering, Nondestructive Evaluation and Health Monitoring of Aerospace Materials, Composites, and Civil Infrastructure.* IV(5767), 205-212.

Gilbertson, C. G., and Ahlborn, T. M. (2004). "A Probabilistic Comparison of Prestress Loss Methods in Prestressed Concrete Beams." *PCI J.*, 49(5), 52-69.

Goldsmith, W. (1965). *Impact: The Theory and Physical Behavior of Colliding Solids*, Edward Arnold Press, Ltd.

Gross, S. P. (1999). "Field Performance of Prestressed High Performance Concrete Highway Bridges in Texas." Doctoral dissertation, The Univ. of Texas, Austin.

Han, S., and Kim, J. (2004). "Effect of temperature and age on the relationship between dynamic and static elastic modulus of concrete." *Cement and Concrete Research*, 34, 1219-1227.

Hornibrook, F. B. (1939). "Application of Sonic Method to Freezing and Thawing Studies of Concrete." ASTM Bulletin No. 101.

Hsu, T. (1981). "Fatigue of Plain Concrete." *Proc. ACI Journal*, 78, 292-305.

International Building Code (2006). International Code Council, Inc., IL.

Joh, S.H. (1996). "Advances in Interpretation and Analysis Techniques of the Spectral-Analysis-of-Surface-Waves (SASW) Method." Doctoral dissertation, The Univ. of Texas, Austin.

Jones, R. (1953). "Testing of Concrete by the Ultrasonic Pulse Technique." *Proceed., Highway Research Board*, 32.

Jones, R., (1962). *Non-Destructive Testing of Concrete*, Cambridge University Press, London.

Kalinski, M. E., K. H. Stokoe, J. O. Jirsa, and J. M. Roesset (1994). "Nondestructive Identification of Internally Damaged Areas of Concrete Beam Using the Spectral Analysis of Surface Waves Method." *Transportation Research Record. 1458*, Transportation Research Board, Washington, D.C., 14-19.

Kang, T., Joh, S., and Cho, M. (2006). "Structural Integrity Assessment of Tunnel Concrete Lining by Resonance Search Technique." *Key Engineering Materials*, 321-323, 302-305.

Kaszynska, M. (2006). "Effect of Temperature on Properties of Fresh Self-Consolidating Concrete." *Archives of Civil Engineering*, 52(2), 277-287.

Khayat, K. H. (1999). "Workability, Testing, and Performance of Self-Consolidating Concrete." *ACI Materials J.*, 96(3), 346-353.

Khayat, K. H., Bickly, J., and Lessard, M. (2000). "Performance of Self-Consolidating Concrete for Casting Basement and Foundation Walls." *ACI Materials J.*, 97(3), 374-380.

Kim, D., Seo, W. S., and Lee, K. M. (2006). "IE-SASW Method for Nondestructive Evaluation of Concrete Structure." *NDT&E International*, 39, 143-154.

Kowalsky, M. J., Zia, P., Wagner, M. C., and Warren, B. A. (2001). "The Behavior of Prestressed High Performance Concrete Bridge Girders for US Highway 401 over the Neuse River in Raleigh, NC." Federal Highway Administration Research Report 23241-97-8, Washington, D.C.

Kramer, S. L. (1996). *Geotechnical Earthquake Engineering*, Prentice-Hall, Inc. New Jersey.

Kukay, B., Barr, P. J., and Halling, M.W. (2007). "A Comparison of Time Dependent Prestress Losses in a Two-Span, Prestressed Conctrete Bridge." Doctoral dissertation, Utah State University, Logan.

Lee, H., Yim, H., and Lee K. (2003). "Velocity-Strength Relationship of Concrete by Impact-Echo Method." *ACI Materials J.*, 100(1), 49-54.

Lin, J., and Sansalone, M. (1996). "Impact-Echo Studies of Interfacial Bond Quality in Concrete: Part 1- Effects of Unbonded Fraction of Area." *ACI Materials J.*, 93(3), 223-232.

Lydon, F. D., and Balendran, R. V. (1986). "Some Observations on Elastic Properties of Plain Concrete." *Cement and Concrete Research*, 16(3), 314-324.

Malhotra, V. M., and Carino, N. J. (2000). *Handbook on Nondestructive Testing of Concrete*, CRC Press, Inc., Florida.

Mehta, P., and Monteiro, P. (2006). *Concrete - Microstructure, Properties, and Materials, 3rd Ed.*, McGraw Hill Company, Inc., New York.

Mesbah, H. A., Lachemi, M., and Aitcin, P. C. (2002). "Determination of Elastic Properties of High-Performance Concrete at Early Ages." *ACI Materials J.*, 99(1), 37-41.

Nagy, A. (1997). "Determination of E-modulus of Young Concrete with Nondestructive Method." *J. of Materials in Civil Eng.*, 9(1), 15-20.

Naito, C. J., Parent, G., and Brunn, G. (2006). "Performance of Bulb-Tee Girders Made with Self-Consolidating Concrete." *PCI Journal*, 51(6), 72-85.

Nazarian, S. (1984). "In Situ Determination of Elastic Moduli of Soil Deposits and Pavement System by Spectral-Analysis-of-Surface-Wave Method." Doctoral dissertation, The Univ. of Texas, Austin.

Neville, A. M. (1996). *Properties of Concrete, 4th ed.*, Pearson Education Limited. New York.

Nogueria, C. L., and Willam, K. J. (2001). "Ultrasonic Testing of Damage in Concrete under Uniaxial Compression." *ACI Materials J.*, 98(3), 265-275.

Obert, L., and Duvall, W. I. (1941). "Discussion of Dynamic Methods of Testing Concrete with Suggestions for Standardization." *Proc., ASTM,* 41.

Park, Y.J., and Ang., A. H. S. (1985). "Mechanistic Seismic Damage Model for Reinforced Concrete." *ASCE J. of Structural Eng.*, 111(4), 722-757

Pessiki, S., and Johnson, M. (1996). "Nondestructive Evaluation of Early-Age Concrete Strength in Plate Structures by the Impact-Echo Method." *ACI Materials J.*, 93(3), 260-271.

Popovics, J. S. (1997). "Effects of Poisson's Ratio on Impact-Echo Test Analysis." *J. of Eng. Mechanics*, 123(8).

Powers, T. C. (1938). "Measuring Young's Modulus of Elasticity by Means of Sonic Vibrations." *Proc., ASTM*, 5(38).

Rao, P. S., Sivarama B., Lakshmanan, N.; and Stangenberg, F. (1998). "Damage Model for Reinforced Concrete Elements under Cyclic Loading." *ACI Materials J.*, 95(6), 682-690.

Rayleigh, J. W. S. (1976). *Theory of Sound.* Dover Publications, New York

Richart, F. E.; Hall, J. R.; and Woods, R. D. (1970). *Vibrations of Soils and Foundations*, Prentice-Hall, Inc., New Jersey.

Roller, J. J., Russell, H. G., Bruce, R. N., and Martin, B. T. (1995). "Long-Term Performance of Prestressed, Pretensioned High Strength Concrete Bridge Girders." *PCI Journal*, 43(6), 48-58.

Sadeghi, K., Lamirault, J., and Sieffert, J. G. (1993). "Damage Indicator Improvement Applied on R/C Structures Subjected to Cyclic Loading." *Proc., Second EURODYN*, 129-136.

Sansalone, M. (1986). "Flaw Detection in Concrete Using Transient Stress Waves," Doctoral dissertation, Cornell University, New York.

Sansalone, M. (1997). "Impact-Echo: The Complete Story." *ACI Structural J.*, 94(6), 777-786.

Sansalone, M., and Carino, N. J. (1986). "Impact-Echo: A Method for Flaw Detection in Concrete Using Transient Stress Waves." *NBSIR 86-3452, National Bureau of Standards*, Gaithersburg, Maryland.

Sansalone, M., and Carino, N. J. (1987). "The Transient Impact Response of Plates Containing Disk-shaped Flaws." *National Bureau of Standards Journal of Research*, 92(6), 369-381.

Sansalone, M., Lin, J., and Streett W. B. (1997). "A Procedure for Determining P-wave Speed in Concrete for Use in Impact-Echo Testing Using a P-wave Speed Measurement Technique." *ACI Materials J.*, 94(6), 531-539.

Sansalone, M., Lin, J., and Streett, W. B. (1998). "Determining the Depths of Surface-Opening Cracks Using Impact Generated Stress Waves and Time-of-Flight Techniques." *ACI Material J.*, 95(2), 168-177.

Seely, R. L. (2005). "Non-destructive Analysis of Concrete Through Dynamic Testing." MS Thesis, Utah State University, Logan.

Shokouhi, P. (2008). "Stress Dependency of Sonic Velocity in Concrete Under Uniaxial Load." *Proc. Transportation Research Record 87th Annual Meeting*, Transportation Research Board, Washington, D.C.

Stallings, M. J., Barnes, R. W., and Eskildsen, S. (2003). "Camber and Prestress Losses in Alabama HPC Bridge Girders." *PCI Journal*, 48(5), 90-104.

Stanton, T. E. (1944). "Tests Comparing the Modulus of Elasticity of Portland Cement Concrete as Determined by the Dynamic (Sonic) and Compression (Secant at 1000 psi) Methods." *ASTM Bulletin No. 131*.

Stokoe, K.H., Wright, S.G., Bay., J.A., and Roesset, J.M. (1994). "Characterization of Geotechnical Sites by SASW Method, Geophysical Characterization of Sites." *ISSMFE Technical Committee #10, XIII ICSMFE*, New Delhi, India, 15-25.

Suaris, W., and Fernando, V. (1987). "Ultrasonic Pulse Attenuation as a Measure of Damage Growth during Cyclic Loading of Concrete." *ACI Materials J.*, 84(3), 185-193.

Suaris, W.; Ouyang, C.; and Fernando, V. M. (1990). "Damage Model for Cyclic Loading of Concrete." *J. of Eng. Mechanics*, 116(5), 1020-1035.

Tadros, M. K., Al-Omaishi, N., Seguirant, S. J., and Gallt, J.G. (2003). "Prestress Losses in Pretensioned High-Strength Concrete Bridge Girders." *NCHRP Report 496*, National Cooperative Highway Research Program, Transportation Research Board, National Research Council, Washington, D.C.

Tarantola, A. (1987). *Inverse Problem Theory: Methods for Data Fitting and Model Parameter Estimation.* Elsevier, New York.

Timoshenko, S. P., and Goodier, J. (1970) *Theory of Elasticity 3rd Ed.* McGraw-Hill Publishing Co., New York.

Whitehurst, E. A. (1966). "Evaluation of Concrete Properties from Sonic Tests." *American Concrete Institute*, Iowa State University Press, Detroit.

www.wikipedia.com, 2008

Yang, Y., and Myers, J. J. (2005). "Prestress Loss Measurements in Missouri's First Fully Instrumented High-Performance Concrete Bridge." *Transportation Research Record. 1928.* Transportation Research Board, Washington, D.C., 118-125.

CURRICULUM VITAE

Shane D. Boone
(May 2008)

Career Objective:

To design and build progressively innovative structures. To analyze existing

structures using existing methods of nondestructive testing of concrete and to

improve those methods through continued research and development.

Education:

The University of Tennessee, Knoxville – BS Civil Engineering, 12/13/02.

The University of Tennessee, Knoxville – MS Civil Engineering, 5/8/05.

Utah State University – PhD Civil Engineering. 5/08. Grad GPA – 3.92.

Experience:

BWXT Y-12 – Structural Engineer, 11/1/03 – Present.

Responsibilities:

Design of new structures using materials such as wood, concrete, steel,

and masonry. Technical assistance and structural evaluation of

existing structures on site. Research in new areas of non-destructive

testing of concrete structures and presentation of findings to BWXT Y-

12 management and DNFSB members.

BWXT Y-12 - Subcontract Technical Representative / Field Engineer, 5/13/02 –

11/1/03

Responsibilities:

Technical representative for multiple direct-hire and subcontract

construction assignments. Performance of construction engineering

assignments of a varied nature requiring a full working knowledge of

construction engineering practices and specific assignment scope.

Awards:

William Cordon Concrete Scholarship, 2007-2008.

Transportation Research Board Utah Transportation Center Graduate Student of

the Year, 2007.